Modelling of end-pumped Ho:YLF amplifiers

by
Oliver John Philip Collett

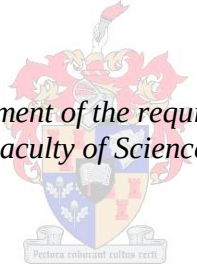

Thesis presented in fulfilment of the requirements for the degree of Masters of Science in the Faculty of Science at Stellenbosch University

Supervisor: Dr Lourens R. Botha
Co-supervisor: Dr Daniel Esser and Dr Christoph Bollig

March 2013

Declaration

By submitting this thesis/dissertation electronically, I declare that the entirety of the work contained therein is my own, original work, that I am the sole author thereof (save to the extent explicitly otherwise stated), that reproduction and publication thereof by Stellenbosch University will not infringe any third party rights and that I have not previously in its entirety or in part submitted it for obtaining any qualification.

Abstract

This work is a thesis regarding the energy scaling of end-pumped Ho:YLF amplifiers. The work includes: a brief review of laser physics and models, the development of a suitable three dimensional time resolved numerical model, a parametric study of double pass amplifiers simulated using the model, comparison between the simulation and the experimental results of a double pass amplifier system, and simulation of a high energy single pass amplifier.

A three dimensional time resolved numerical model of an end-pumped amplifier was developed. A rate equation model was used to simulate the absorption and emission of light, energy transfer upconversion, and spontaneous emission within the gain medium. In the traveling wave approximation the propagation of light through the gain medium was modelled with the use of a split step method that included diffraction and gain.

A parametric study was performed to find the design parameters for an end-pumped two pass amplifier. Limited optimisation of several amplifier parameters was performed. The study focused on the optimisation of the energy per pulse through changes to the following parameters: crystal length, laser beam size, pump beam sizes, and pump wavelength. The final design specifications for an experimental system were for a 100 mm long 0.5 % (atm.) doped Ho:YLF gain medium, pump and seed beams with spot sizes with effective beam sizes of 1 mm and 0.95 mm respectively and a pump wavelength of 1892 nm. The simulation predicted pulse energies above 480 mJ when seeded by a 55 mJ pulse at repetition rates of 50 Hz.

The experimentally realised system with similar design parameters produced the highest reported energy, 330 mJ, from an end-pumped Ho:YLF amplifier. Comparison between the simulation and the experimental results showed significant deviation. The deviation was explained by the effect of parameters not included previously in the simulation. These parameters were the power of the continuous

component of the seed beam, and the energy transfer upconversion rate. Limitations and fidelity of the numerical model with respect to the experimental system are discussed, notably the model of the highly divergent pump beam was simplistic.

Preliminary simulation results of a high energy single pass amplifier predict that energy scaling in Ho:YLF follows linearly with respect to pump power and that in the ideal case, multi-Joule operation is possible at 50 Hz with optical to optical efficiencies of 19 %.

Acknowledgments

I thank my supervisors Dr Daniel Esser, Dr Christoph Bollig, and Dr Lourens Botha for the opportunity to study and learn, and for assistance they have given me: Daniel, thank you for your guidance, and enthusiasm and interest in this study; Chistoph, thank you for sharing and teaching me laser physics; and Lourens for all the administrative support.

I would also like to thank members of the laser sources team that have been of assistance during my research. Hencharl, Cobus, Wayne, and Dieter thank you for entertaining even my wildest ideas and for the encouragement.

I feel very fortunate to have studied with my fellow students at the National Laser Centre. I would like to thank Ludwig, Nicolene, Darryl, Attie and Alpha for many helpful discussions.

I would also like to acknowledge the support of the National Laser Centre for funding this work.

The support, interest, and perspectives of my family and friends have been invaluable.

Contents

List of Figures

List of Tables

Nomenclature

$\mathbf{k}$	Wave vector.
β_{ij}	Branching ratio from level i to level j.
$\Delta\Omega$	Solid angle, two dimentional measurement of angle.
γ_i	Decay rate of a level due to some process, for instance spontaneous emmission, γ_{spon}, or non-radiative decay, γ_{nr}, or migration between ions, γ_{mig}.
λ	Wavelength of light, length of one optical cycle.
$\mathcal{F}$	Fourier Transfrom, transformation of some function x to a function in the frequency domian, X, $X = \mathcal{F}(x)$.
ν	Frequency of light, number of optical cycles passing a point in one second.
π	Either the ratio of the circumference of the circle to its diameter or the linear polarisation parallel to the c axis in a YLF crystal.
ρ	Photon density.
σ	A linear polarisation that is parallel to the a axis in YLF crystal.
σ_{ab}	Absorption cross section of the active ion; often a function of wavelegth $\sigma_{ab}(\lambda)$.
σ_{em}	Emission cross section of an active ion.
τ_i	Lifetime of a energy level i.
cm^{-1}	Inverse centimeters, spectroscopic measurement unit of wavelength.
$I(\lambda)$	Intensity of light.

k Wavenumber.

k_B Boltzman constant.

M^2 Beam qaulity factor.

N_i The density of ions in some level i.

w_{eff} Effective beam radius.

AOM Acoustic Optical Modulator, optical component that induces loss in a laser cavity by forming a grating in the material.

ASE Amplified Spontaneous Emission. Spontaneous emission of light from excited ions that is amplified by the laser medium.

c Speed of light.

CW Continuous wave. A laser property, emitting a beam or wave of light with constant intensity.

dB Decibel, unit of measuremet of gain $1dB = 10log_{10}\left(\frac{P_{out}}{P_{in}}\right)$

ETU Energy Transfer Upconversion.

FFT Fast Fourier Transform, a numerical method of calculating the fourier series of some signal.

h Plank's constant, the proportionality constant between the frequency of light and its energy.

Hz Hertz, measurement of frequency.

mJ Millijoule, unit of energy.

n Refractive index of light, relates group velocity to the speed of light.

nm Nanometer, unit of length.

ns Nanosecond, 10^{-9} seconds.

PRF Pulse Repetition Frequency, number of pulses per second in a laser beam.

Q-switched As in Q-switched laser, method of generating pulses from a laser by changing the quality of the cavity.

W Watt, unit of power.

YLF Yttrium Lithium Flouride, Crystal host normaly doped with Lanthanide ions, e.g. Ho^{3+} : YLF.

Chapter 1

Introduction

Generating high energy laser pulses in the two micrometer wavelength range has been of interest in a number of scientific, medical and military fields. These laser pulses have been used in a large number of applications [4]: detection of low concentrations of atmospheric gases and measurement of atmospheric wind velocity using Light Detection And Ranging (LIDAR) systems, tissue cutting in medial environment, Infra-Red Counter Measures (DIRCM) systems, free space optical communication, and a host of other applications.

The different applications require laser pulses with different properties. Operation past the water absorption features at 2 μm with high efficiency has been achieved with Optical Parametric Oscillators (OPOs) and holmium lasers [5].

One method of generating laser pulses with the desired properties uses a Master Oscillator to generate a pulse with the desired properties followed by a Power Amplifier to scale the energy (and average power) of the pulse while retaining the other desired properties. Such systems are commonly referred to as MOPA systems.

This thesis focused on simulating the amplifier stages of a MOPA system. The scope of this work was limited to amplification of 2 μm pulses by the stimulated emission process in trivalent Holmium (Ho^{3+}) ions doped into Yttrium Lithium Fluoride (YLF) crystals. Additionally the work was limited to end-pumping the gain medium.

The amplifier was simulated by a numerical model that was resolved into three spatial dimensions and

time. The model utilized numerical methods due to non-linearity in the equations that govern the amplification of Q-switched laser pulses.

1.1 Purpose

The purpose of this work was to study the dynamics of pulsed Ho:YLF amplifiers using a mathematical model. The goals in this study were to:

Understand and formulate physical processes. Analysis of the effect of underlying processes on the behavior of the amplifier.

A parametric study to find the design parameters and evaluate the effect of various amplifier parameters on the dynamics.

Optimization based on a numerical model to design a high energy amplifier.

Comparison with existing amplifiers to establish confidence in the model.

Explore potential energy scaling schemes.

1.2 Background & Literature Review

Modeling of lasers has historically occurred in tandem with the development of laser sources. As lasers and amplifiers with different dynamics were designed and built, the models have adjusted to describe the systems. These models have in turn been used to extrapolate from the known parameter space to predict performance of different laser and amplifier systems.

The field of diode laser or laser end-pumped three-level lasers (and amplifiers) based on trivalent ions of the Lanthanide series doped into crystalline hosts has specialized from a large body of laser theory.

Modeling of these lasers has drawn on theory and experimental results from related fields as well as relying on comparison with experimental results from laser systems as a test of validity. Related fields include spectroscopy and material properties of the crystalline gain medium, advances in modeling of other types of laser systems, and laser beam propagation and resonator design.

The development of increasingly sophisticated lasers and amplifiers has led to increasingly complex models. Early development of end-pumped quasi-three level lasers prompted the development of con-

tinuous wave (CW) models by Fan *et al.* [6], showing that the loss due to the lower laser level could be treated as a saturable loss. Risk [7] used a numerical model to investigate the effect of changing the overlap of the pump and laser beam in the gain medium of Continuous Wave (CW) Nd:YAG lasers. This paper discussed both saturation and the spatial distribution of variables. Krupke *et al.* [8] discussed Q-switched operation and scaling laws of three level lasers and amplifiers with an emphasis on the use of high brightness pump sources.

These early works form the basis of the theory for the operation of quasi-three level end-pumped lasers which was utilized in this thesis.

Spectroscopic studies of trivalent Holmium ions doped into fluoride crystals by Payne *et al.* [9] provided necessary information for the development of models of the gain media which were of the utmost relevance for this thesis.

The development of high energy 2 μm lasers and amplifiers for space based LIDAR at NASA lead to studies on side-pumped lasers and amplifiers that used co-doped trivalent Holmium and Thulium (Tm) as active ions in the gain medium. The development prompted major investigation into the energy transfer dynamics and its effect on the operation of co-doped gain media, as well as a host of other studies [1, 10, 11, 12]. This included detailed spectroscopic studies [1, 13, 14] of both co-doped and singly doped gain media. The laser systems developed included a MOPA system that produced 600 mJ pulses at 2 μm [15].

More recently there has been development of end-pumped lasers and amplifiers that use gain media singly doped with Holmium ions. End-pumped systems are distinguished mainly by the difference in the pump source. These may include fiber lasers [5], resonant Tm lasers [16] and intracavity pumping with Tm lasers [17, 18]. These systems typically have high efficiency and good beam quality [5, 16, 19], but have not reached the energy of the side pumped systems. This development has been enabled by the increasing power of both fiber and bulk pump lasers.

Models of beam propagation through active gain media, using different techniques to solve the governing partial differential equations, have been applied to optical resonators and amplifiers [20, 21, 22, 23]. There are analytical solutions to the paraxial scalar wave equation, given by the Hermite (Laguerre)-Gaussian polynomials, however, these solutions are restricted to special cases [23]. More general approaches to solving diffraction effects in solid state lasers have used numerical methods [22, 23].

The classes of numerical methods that have been employed to solve either the Rayleigh-Sommerfeld

diffraction integral or equivalent differential forms include, direct integration, direct integration using the Fast Fourier transform (FFT), and angular spectrum methods [24]. While these methods are of comparable computational requirements each method may have different sampling requirements and associated errors. Angular spectrum methods are typically accurate in regions close to the aperture and have greater errors far from it.

Angular spectrum methods have recently been used in numerical models of beam diffraction through a number of different quasi-three level laser systems. Using this method Shu [21] accounted for diffraction and saturation in Ytterbium doped oscillators and amplifiers. Often these models include the temperature dependence of the refractive index to study the effect of the distribution of temperature in the gain medium on the characteristics of the laser or amplifier. For example Wohlmuth *et al.* [25] analyzed the change in beam quality due to the dynamics of a pulsed, multimode Thulium laser. Xiang *et al.* [26] investigated the improved beam quality from the output from a Nd:YVO_4 laser amplifier with different pump focuses.

The variational principle methods have been applied to lasers and amplifiers with saturable gain to optimize some goal [27]. These methods typically reduce the complexity of the system in order to formulate the problem in a soluble form yielding exact solutions. Typical assumptions include assumed gain profiles, thin gain media, or CW operation. Typical gain profiles are for example: Top hat (Heaviside π), Gaussian and Super-Gaussian functions [27].

The limits on energy storage due to Amplified Spontaneous Emission (ASE) were discussed by Fan [28].

Much of the applicable theory has been well established and published in books and reference articles that focus on particular developments. The principles of laser operation is covered by Siegman's *Lasers* [23] as well as Svelto's *Principles of Lasers* [29]. Eichhorn's paper *Quasi-three-level solid-state lasers in the near and mid infrared based on trivalent rare earth ions* [30] gives insight into some aspects of laser design and modeling. The review paper by Cornacchia *et al. Review- 2um lasers with fluoride crystals: Research and development* [31] reviews advances in fluoride hosts.

1.3 Outline of contents

In Chapter 2 the theory of solid state lasers explaining the operation of Q-switched lasers and amplifiers is presented. The chapter deals with the processes that occur in the gain medium between the active ions and the radiation as well as the inherent diffraction of scalar electric fields. Chapter 3 describes the formulates of the problem and outlines the development of a soluble numerical model. The numerical model described is quite general, in the next chapter a specific example is considered. The design of a Ho:YLF power amplifier stage is outlined and aspects of the behavior are predicted. The chapter contains specific properties of the amplifier: the properties of the Ho:YLF gain medium, seed laser and pump laser. The results of comparison with such an experimental amplifier are reported in Chapter 5. Energy scaling schemes are presented in Chapter 6. Finally the work is summarized and extensions are discussed.

Chapter 2

Solid state laser theory

The typical operation of optically pumped solid state lasers relies on the energy cycle of an active ion in a host crystal. The ion is "pumped" from the ground state or lower pump level into the upper pump energy level by absorbing a pump photon. It then either decays by spontaneous emission into a lower energy level or is stimulated to emit a photon into the laser field and undergo the required quantum energy level transition. The particular form of the energy cycle depends on the available transitions between energy levels of a specific ion and the rate at which different processes proceed. Solid state lasers are often classed by the number of levels that have a significant influence on the operation of the laser. A simplified energy level diagram for a three level laser with some of the processes is displayed in Figure 2.1.

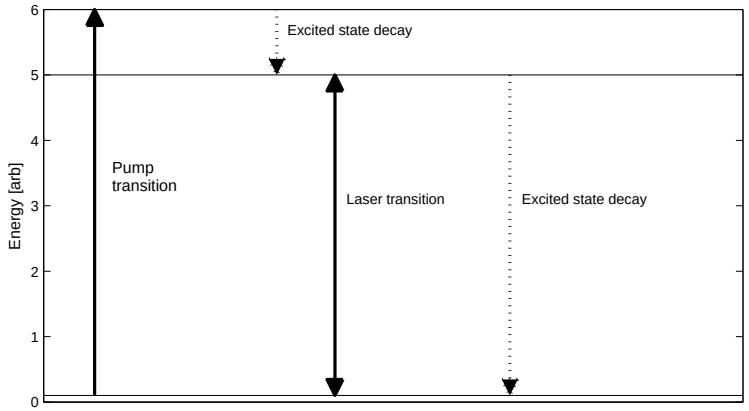

Figure 2.1: Three level laser energy level diagram.

The notable feature of the three level lasers is that the energy levels involved with the absorption of the pump light are also involved in the emission of light into the laser field. This is important because absorption and stimulated emission are reciprocal processes. This means that the probability of an ion absorbing a photon and of being stimulated to emit a photon between any two non-degenerate levels is the same for a given intensity of the radiation [23].

Quasi-three level lasers differ from three level laser in that the "levels" are manifolds comprised of a number of stark split sub-levels. This complicates the energy cycle but the basic idea, of following each possible energy cycle remains valid.

2.1 The governing processes in the rate equation limit

In this section the basic processes that influence the operation of a laser are discussed. These include absorption and stimulated emission, radiative decays of excited levels, and energy transfer between ions. The strong coupling of levels within manifolds of rare earth ions, such as Neodymium, Thulium, or Holmium doped into laser gain media, changes the description of the processes.

2.1.1 Absorption and stimulated emission

Absorption and stimulated emission are fundamental to the operation of lasers because these processes lead directly to the amplification or attenuation of coherent light. The remainder of this section follows the discussion by Siegman on the radiation transport equations under the rate equation assumptions [23].

Consider the absorption and stimulated emission of light by a small volume of some gain material and assume that the active ions have been doped uniformly into the material at some density N_{active}. The density of ions in a quantum energy level i is N_i and is called the population density of that level. The incident light has an intensity I at a certain wavelength λ. As the light beam propagates through the medium it changes intensity as it gives or receives quanta of energy from ions in some non-degenerate energy levels 1 and 2 with associated population densities $N_1$and N_2. The rate at which the population densities change due to **absorption** is given by,

$$\frac{dN_2}{dt} = \sigma(\lambda)\frac{I(\lambda)}{h\nu}N_1, \tag{2.1}$$

and,

$$\frac{dN_1}{dt} = -\sigma(\lambda)\frac{I(\lambda)}{h\nu}N_1. \tag{2.2}$$

The energy density of the beam of light is given by $\frac{c}{n}I$, were c is the speed of light, n is the refractive index of the gain medium. The cross section σ at vacuum wavelength λ is the probability that an ion absorbs or emits a photon of that wavelength. The rate depends linearly on the product of the intensity of the beam and the population density of the lower level N_1. The rate at which the population densities change due to **stimulated emission** are

$$\frac{dN_2}{dt} = -\sigma(\lambda)\frac{I(\lambda)}{h\nu}N_2, \tag{2.3}$$

and

$$\frac{dN_1}{dt} = \sigma(\lambda)\frac{I(\lambda)}{h\nu}N_2. \tag{2.4}$$

Similar to the absorption process, Equations 2.1-2.2, the rate for the stimulated emission depends linearly on the product of the intensity of the beam and the population density of the upper level N_2. The rate also depends on the cross section which in turn depends on the wavelength of the beam. The change in the intensity of the beam due to both absorption and stimulated emission as it propagates in the positive z direction though the volume is,

$$\frac{\partial I}{\partial z} - \frac{n}{c}\frac{\partial I}{\partial t} = I(\lambda)\sigma(\lambda)[N_2 - N_1]. \tag{2.5}$$

For net absorption of the beam the population density of the upper level must be less than that of the lower level ($N_2 < N_1$) while for net amplification or gain the reverse condition, ($N_2 > N_1$) must hold. This is a consequence of the equality of the cross section of stimulated emission and absorption.

The radiation transport equations (2.3, 2.4, 2.5) are coupled and non-linear. The discussion above is the case for two non-degenerate levels. The absorption and stimulated emission processes are more complicated for real active ions in host crystals as discussed in the next section.

2.1.2 Absorption and stimulated emission between strongly coupled manifolds

Boltzmann distribution

The distribution of the population densities of the levels in each manifold may, in some instances, be coupled strongly [9, 29, 32]. In some gain materials the energy level structure of rare earth ion dopants is complicated by splitting of degenerate energy levels into manifolds of Stark levels by the crystal field [9, 14]. In the bulk material the populations of the stark levels may then be coupled thermally. In the steady state the population distribution within each manifold is expected to relax into a Boltzmann distribution.

The dynamic change in population of these levels due to other processes, such as depopulation of excited states due to stimulated emission is assumed to have no effect on the distribution. This assumption is valid if the redistribution of population between levels due to thermodynamic processes takes place on a much faster time scale than the other processes. Another way to interpret this assumption is that it represents the the lower limit of applicability for this theory. The other processes should then take place at much slower rates than the thermal redistribution, namely:

- the build up of laser radiation in the cavity which is in the nanosecond to 100's of nanosecond range for Q-switched pulse generation.
- the intensity of the pump beam changes slowly under CW pumping.
- the lifetime of upper laser levels of rare earth ions ranges from microseconds to 10's of milliseconds.
- the energy transfer upconversion rates are variable but slower than the relaxation of levels within each manifold.

When the levels are in thermal equilibrium the Stark levels form a Boltzmann distribution and the population $f_{k,j}(T)$ of a Stark level j within manifold k is given by

$$f_{k,j}(T) = \frac{g_j e^{\frac{-\left(E_{k,j}-E_{k,1}\right)}{k_B T}}}{Z_k}, \tag{2.6}$$

were $E_{k,j}$ is the energy of the Stark level with a degeneracy g_j, k_B is the Boltzmann constant and T is the absolute temperature of the system. The corresponding partition function is given by

$$Z_k(T) = \sum_j g_j e^{\frac{-\left(E_{k,j}-E_{k,1}\right)}{k_B T}}. \tag{2.7}$$

Reciprocity Principle

The distribution of Stark levels within each manifold causes the ratio of the absorption and emission cross sections between the two manifolds to fixed by the reciprocity principle [32, 9]. The consequence is that the effective emission cross section σ_{em} and effective absorption cross sections σ_{ab} of the manifold are related by

$$\sigma_{em}(\lambda, T) = \sigma_{ab}(\lambda, T)\, e^{-\frac{hc}{k_B T}\left(\frac{1}{\lambda}-\frac{1}{\lambda_u}\right)} \tag{2.8}$$

where λ_u is given by,

$$\lambda_u = \frac{hc}{k_B T}\left(ln\frac{Z_g}{Z_u}\right)^{-1}. \tag{2.9}$$

The population of the relevant manifold is needed to calculate the absorption of the light that propagates through the active medium,

$$\frac{\partial I}{\partial z} - \frac{n}{c}\frac{\partial I}{\partial t} = I(\lambda)\left[\sigma_{em}(\lambda) N_2 - \sigma_{ab}(\lambda) N_1\right], \tag{2.10}$$

$$\frac{dN_2}{dt} = \frac{I(\lambda)}{h\nu}\left[-\sigma_{em}(\lambda) N_2 + \sigma_{ab}(\lambda) N_1\right], \tag{2.11}$$

$$\frac{dN_1}{dt} = -\frac{dN_2}{dt}, \tag{2.12}$$

were N_i is the population density of the i^{th} manifold of the active ion in the medium. The reciprocity principle reduces the complexity of the absorption and stimulated emission processes in strongly coupled systems since the number of levels that influence the dynamics are greatly reduced. In this work the assumption is made implicitly by the use of effective absorption and emission cross sections. The measurement of the cross sections typically occurs under steady state conditions [14].

Transparency

The case were the derivative of Equation 2.10 is zero, the gain medium is said to become transparent. In this case if the population densities of the ions are found in only the two levels N_1 and N_2 as is approximately the case for Holmium in crystalline hosts [33]. Then the population at which transparency occurs depends only on the wavelength of the radiation and the temperature of the gain medium, *viz.*

$$0 = [\sigma_{em}(\lambda) N_2 - \sigma_{ab}(\lambda) N_1], \tag{2.13}$$

substituting $N_1 = N_{tot} - N_2$, were N_{tot} is the total, constant population density, and dividing by $\sigma_{ab} N_{tot}$ the gives,

$$\frac{\sigma_{em} + \sigma_{ab}}{\sigma_{ab}} \frac{N_2}{N_{tot}} \quad -1 = \quad 0. \tag{2.14}$$

The reciprocity principle in the form of Equation 2.8 makes the wavelength and temperature dependence explicit,

$$\frac{\sigma_{ab} e^{-\frac{hc}{k_B T}\left(\frac{1}{\lambda} - \frac{1}{\lambda_u}\right)} + \sigma_{ab}}{\sigma_{ab}} \frac{N_2}{N_{tot}} \quad -1 = \quad 0, \tag{2.15}$$

$$\frac{N_2}{N_{tot}} \quad = \quad \frac{1}{\left(e^{-\frac{hc}{k_B T}\left(\frac{1}{\lambda} - \frac{1}{\lambda_u}\right)} + 1\right)}. \tag{2.16}$$

Saturation

The change in intensity of a beam that an amplifier produces is linked to the change in gain of that amplifier [23], similarly energy that can be extracted from a volume is linked to the systems gain. The relationship between the fluence change in a small region of the gain medium in a certain time and the gain at the two boundary times may be established by considering the Equations 2.10- 2.12. If no other processes occur that change the population density then as a consequence of Equation 2.12, the combined density of the two levels does not change and is a constant which will be named the total population density, N_{tot} ,

$$N_{tot} = N_1 + N_2. \tag{2.17}$$

This implies that it is possible to rewrite Equations 2.10 & 2.11 independent of N_1,

$$\frac{\partial I}{\partial z} - \frac{n}{c}\frac{\partial I}{\partial t} = I(\lambda)\left[(\sigma_{em}(\lambda) + \sigma_{ab}(\lambda))N_2 - \sigma_{ab}(\lambda) N_{tot}\right], \tag{2.18}$$

$$\frac{dN_2}{dt} = -\frac{I(\lambda)}{h\nu}\left[(\sigma_{em}(\lambda) + \sigma_{ab}(\lambda))N_2 - \sigma_{ab}(\lambda) N_{tot}\right]. \tag{2.19}$$

By considering the two points in time it is possible to relate the gain per unit length to the fluence change. By performing separation of variables on the above equation we find that,

$$\frac{dN_2}{N_2 - b} = -\frac{1}{a} I(\lambda)\, dt, \tag{2.20}$$

were,

$$a = \frac{h\nu}{\sigma_{ab}(\lambda) + \sigma_{em}(\lambda)}. \tag{2.21}$$

$$b = \frac{\sigma_{ab}(\lambda) N_{tot}}{\sigma_{ab}(\lambda) + \sigma_{em}(\lambda)}, \tag{2.22}$$

This equation links two important features of three-level amplifiers: the population of the upper state required for transparency, b, and the saturation fluence of the material, a (also commonly denoted by F_{sat}). Integrating both sides we find that the integral of the intensity between two given points in time is a function of the population density ,

$$\int_{t1}^{t2} I(\lambda)\, dt = -F_{sat} \int_{x1}^{x2} \frac{dN_2}{N_2 - b}, \tag{2.23}$$

were $x1$and $x2$ are the population densities at $t1$and $t2$ respectively. Associating the fluence, F_{t1-t2}, with the change of intensity between these two times and integrating the right hand side gives,

$$F_{t1-t2} = F_{sat} \ln\left(\frac{x2 - b}{x1 - b}\right). \tag{2.24}$$

This equation links the ratio of the difference between the population densities and the transparency population to the fluence. In turn the difference between the population densities and the transparency population is proportional to the gain per unit length,

$$\frac{1}{I(\lambda)}\left(\frac{\partial I}{\partial z}-\frac{n}{c}\frac{\partial I}{\partial t}\right) = [(\sigma_{em}(\lambda)+\sigma_{ab}(\lambda))N_2-\sigma_{ab}(\lambda)N_{tot}], \tag{2.25}$$

$$G = (\sigma_{em}(\lambda)+\sigma_{ab}(\lambda))[x-b], \tag{2.26}$$

were x is any given population density. Thus the ratio of the gain for two different populations is related to the fluence changes between those two times. The upper manifold population density is bounded by zero and N_{tot} as all populations are positive semi-definite implies that the gain is bounded. Substituting Equation 2.26 for $x2-b$ and $x1-b$, gives the ratio of the gain at those population densities, G_2 and G_1 respectively,

$$F_{t1-t2} = F_{sat}\ln\left(\frac{G_2}{G_1}\right), \tag{2.27}$$

$$\frac{G_2(t2,x2)}{G_1(t1,x1)} = \exp\left(\frac{F_{t1-t2}(t1,t2,x1,x2)}{F_{sat}}\right). \tag{2.28}$$

This equation can be applied between two points within a single pulse to calculate the ratio of the gain from the change in fluence. It can also be seen that the fluence required to significantly reduce the gain of any region of the amplifier is on the order of F_{sat}. Assuming that the same equation holds for each beam of a multipass amplifier means that at the two time points the gain is identical, and thus the ratio of gain at these two times is the same for all beams. This implies that the total fluence change is, n times that of the fluence change of any pass, F_p were n is the number of pass,

$$\frac{G_n(t2,x2)}{G_1(t1,x1)} = \exp\left(\frac{nF_p}{F_{sat}}\right). \tag{2.29}$$

Thus an effective saturation fluence for the first pass, $F_{sat,n}$, decreases by,

$$F_{sat,n} = \frac{F_{sat}}{n}. \tag{2.30}$$

Intra-manifold relaxation

The argument for the validity of this assumption in the case of the amplifiers under study is that the rate of change of population densities with time due to stimulated emission is much smaller than the rate of change due to the relaxation to the Boltzmann distribution. The rate of change due to relaxation can be approximated by,

$$\begin{aligned} \frac{dN}{dt} &= -\frac{N_0 - N}{\tau_{relax}} \\ \frac{dn}{dt} &= -\frac{n_0 - n}{\tau_{relax}}, \end{aligned} \tag{2.31}$$

were τ_{relax} is the rate of relaxation to the population density N_0 given by the Boltzmann distribution, and the relative population is $n = \frac{N}{N_{total}}$. The change in population due to the stimulated emission is given by,

$$\frac{dN}{dt} = -\frac{I(\lambda)\ N\ \sigma_{em}(\lambda)}{h\nu} \tag{2.32}$$

Equating Equations 2.31 and 2.32 to find the deviation from the static population gives,

$$\frac{I(\lambda)\ N\ \sigma_{em}(\lambda)}{h\nu} = \frac{N_0 - N}{\tau_{relax}} \tag{2.33}$$

$$\frac{I(\lambda)\ n\ \sigma_{em}(\lambda)}{h\nu} = \frac{n_0 - n}{\tau_{relax}} \tag{2.34}$$

$$\frac{n_0 - n}{n} = \frac{I(\lambda)\ \sigma_{em}(\lambda)\ \tau_{relax}}{h\nu} \tag{2.35}$$

$$\frac{n}{n_0} = \left(1 + \frac{I(\lambda)\,\sigma_{em}(\lambda)\,\tau_{relax}}{h\nu}\right)^{-1} \tag{2.36}$$

$$\frac{n}{n_0} \backsimeq 1 - \frac{I(\lambda)\,\sigma_{em}(\lambda)\,\tau_{relax}}{h\nu} \tag{2.37}$$

$$\Delta n = -\frac{I(\lambda)\,\sigma_{em}(\lambda)\,\tau_{relax}}{h\nu} \tag{2.38}$$

The ratio of deviated population to the steady state population depends on the intensity of the light, the cross section, and the relaxation rate. The lower bound on this function occurs at maximum intensities, maximum cross section, and maximum relaxation rates.

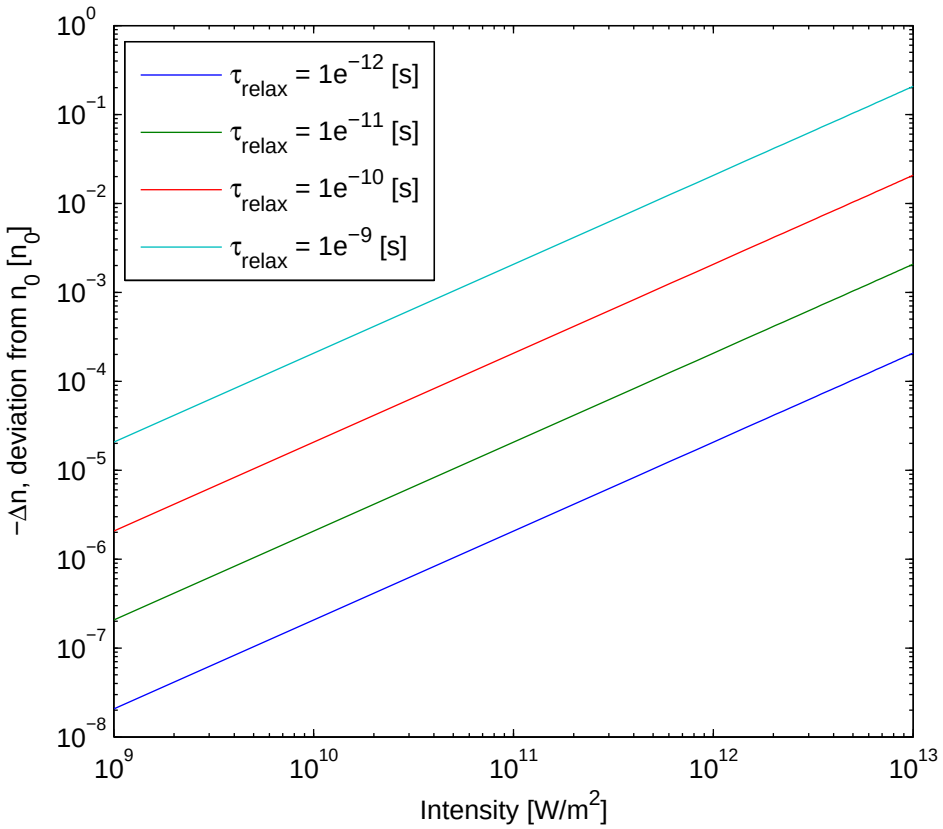

Figure 2.2: Log-Log graph showing the equilibrium population shift due to some intensity. The four traces correspond to the equilibrium values at four different relaxation rates. The cross section was fixed at 2×10^{-24} m^2 for the 2050 nm transition in Ho:YLF.

Figure 2.2 shows the change in equilibrium population due to some beam intensity as calculated by Equation 2.38. The peak intensity of the lasers systems under study is on the order of 10^{11} Watts per meter squared. The figure shows that with relaxation rates in the picoseconds, the redistribution of energy within manifolds is negligible, however, if the relaxation rate is significantly greater, say on the order of nanoseconds, then the redistribution is significant. The relaxation rate in trivalent rare earth ions typically thought to occur on time scales of 10^{-11} s [30].

2.1.3 Spontaneous decay, radiative lifetimes and branching ratios

Ions in excited levels may decay into lower levels by spontaneous decay. The population of Stark levels in an excited manifold remains uniform during decays because the rate of establishing a thermodynamic distribution between the Stark levels in the manifold is much faster than the spontaneous decay rate [29]. The rate equation for this process is given by Equation 2.40 with the decay constant γ_i that is equal to the inverse of the lifetime τ_i of the manifold,

$$\frac{\partial N_i}{\partial t} = \frac{-N_i}{\tau_i} \tag{2.39}$$

$$= -\gamma_i N_i. \tag{2.40}$$

Ions in an excited level N_i decay into a certain lower level N_j with a probability given by the branching ratio β_{ij}. The increase in population density of all the lower lying manifolds N_j, N_{j-1}, N_{j-2}...N_0 are given by

$$\frac{\partial N_j}{\partial t} = \beta_{ij}\gamma_i N_i \tag{2.41}$$

$$\frac{\partial N_{j-1}}{\partial t} = \beta_{ij-1}\gamma_i N_i \tag{2.42}$$

$$\frac{\partial N_{j-2}}{\partial t} = \beta_{ij-2}\gamma_i N_i \tag{2.43}$$

$$\vdots \quad \vdots \quad \vdots \tag{2.44}$$

$$\frac{\partial N_0}{\partial t} = \beta_{i0}\gamma_i N_i. \tag{2.45}$$

By equating the changes to the population of the emitting manifold and sum of the changes to the population densities of the lower lying manifolds, it is clear that the sum of the branching ratios is one,

$$\frac{-\partial N_i}{\partial t} = \sum_{k=0}^{j} \frac{\partial N_k}{\partial t} \tag{2.46}$$

$$\gamma_i N_i = \sum_{k=0}^{j} \beta_{ik}\gamma_k N_k \tag{2.47}$$

$$\sum_{k=0}^{j-1} \beta_{ik} = 1. \tag{2.48}$$

There are other possible decay processes that depopulate excited levels such as non-radiative decay due to multi-phonon relaxation [30] and the energy transfer process of migration [14]. The total rate of

decay of the manifold, that is measured as the fluorescence lifetime, has been shown to be approximated by the sum of these processes [14],

$$\gamma_{flour} \simeq \gamma_{spon} + \gamma_{nr} + \gamma_{mig}, \tag{2.49}$$

were γ_{fluor} is the fluorescence decay rate, γ_{spon} is the spontaneous emission rate, γ_{nr} is the non-radiative decay rate, and γ_{mig} is the rate due to energy transfer migration.

2.1.4 Energy transfer processes

Energy transfer upconversion (ETU) describes the group of processes where energy transfer between ions results in excited manifolds having a net population. Energy transfer occurs between two ions as a result mainly of dipole-dipole interactions [11, 34]. While derivation of the rates for an energy transfer process for the active ions in a particular host crystal is complicated, the concept can be described as a simply[30, 34, 10, 17]; Given two ions in an excited state, one will transition into a lower energy level and the other into a higher energy level with approximately the same energy difference. The reverse energy transfer process may cause transitions of ions in the higher excited and lower energy levels to transition into the initial excited state.

In Ho:YLF upconversion occurring between ions in the upper laser manifold have a probability of exciting to both the $^5I_6$ and $^5I_5$ manifolds[33]. A schematic representation of the ETU process in Ho:YLF is shown in Figure 2.3.

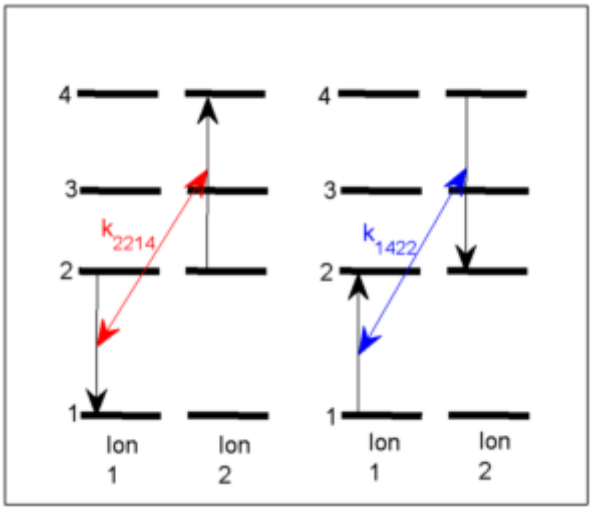

Figure 2.3: A diagram of the energy transfer upconversion processes between two Holmium ions in the gain medium. The first process (red) depopulates the upper laser level (energy level 2) while the second (blue) populates it.

The rate equations for energy transfer process k_{ijlj} in a medium with populations N_i, N_j and N_l that leave the donor and acceptor ions in the same level are[33],

$$\frac{dN_i}{dt} = -k_{ijlj}N_iN_l \tag{2.50}$$
$$\frac{dN_j}{dt} = +2k_{ijlj}N_iN_l \tag{2.51}$$
$$\frac{dN_l}{dt} = -k_{ijlj}N_iN_l. \tag{2.52}$$

Equations 2.50-2.52 show the dependence of the rate of the processes on the product of the population densities of the two starting levels. The rate equations for the reverse process that starts with the donor and acceptor ions in the same level N_j, with a rate constant k_{jijl} are,

$$\frac{dN_i}{dt} = +k_{jijl}N_j^2 \tag{2.53}$$
$$\frac{dN_j}{dt} = -2k_{jijl}N_j^2 \tag{2.54}$$
$$\frac{dN_l}{dt} = +k_{jijl}N_j^2. \tag{2.55}$$

The energy transfer upconversion rate has been shown to depend on the host lattice as well as the doping concentration [11, 35].

2.2 Scalar diffraction theory - The angular spectrum method

This section is an overview of near-field scalar diffraction by Harvey [36] and Goodman [37] using a Fourier Transform technique. The theory relates the diffraction of monochromatic scalar fields to their Fourier components. The diffraction of the field is governed by the Helmholtz equation [36],

$$\left[\nabla^2 + \mathbf{k}^2\right] U(x, y, z) = 0. \tag{2.56}$$

were $\mathbf{k}$ is the wave number of the field in the vacuum. The scalar electric field $U(x, y, z)$ is defined on two planes P_0 and P normal to the propagation axis at z and z_0. The fields are decomposed into plane waves using the analysis Fourier transform on each plane. The Fourier transform pairs on the two planes are given by,

$$A(\alpha, \beta; z_0) = \int\int U(x, y; z_0)\, e^{-i2\pi(\alpha x + \beta y)} dx dy \tag{2.57}$$

$$U(x, y; z_0) = \int\int A(\alpha, \beta; z_0)\, e^{+i2\pi(\alpha x + \beta y)} d\alpha d\beta \tag{2.58}$$

and

$$A(\alpha, \beta; z) = \int\int U(x, y; z)\, e^{-i2\pi(\alpha x + \beta y)} dx dy \tag{2.59}$$

$$U(x, y; z) = \int\int A(\alpha, \beta; z)\, e^{+i2\pi(\alpha x + \beta y)} d\alpha d\beta \tag{2.60}$$

provided that the inverse transforms exist. The theory relates each component of the direction cosine spectrum in one plane to the spectrum of the next plane by a transfer function,

$$A(\alpha, \beta; z) = A_o(\alpha, \beta; z_0)\, e^{ikz\left(\sqrt{1-(\alpha^2+\beta^2)}\right)}. \tag{2.61}$$

The solution $U(\hat{x}, \hat{y}; \hat{z})$ at the second plane at z is constructed by applying the analysis transform $(\mathcal{F})$ followed by multiplication by the transfer function and then applying the synthesis transform $(\mathcal{F}^{-1})$,

$$U(\hat{x}, \hat{y}; \hat{z}) = \mathcal{F}^{-1} : \left\{ \mathcal{F} : \{U_o(\hat{x}, \hat{y}; \hat{z}_0)\}\, e^{ikz\left(\sqrt{1-(\alpha^2+\beta^2)}\right)} \right\}. \tag{2.62}$$

Harvey [36] showed that this procedure is equivalent to the integral formalism of Rayleigh-Sommerfield diffraction. A flow diagram of the algorithm is shown below in Figure 2.4.

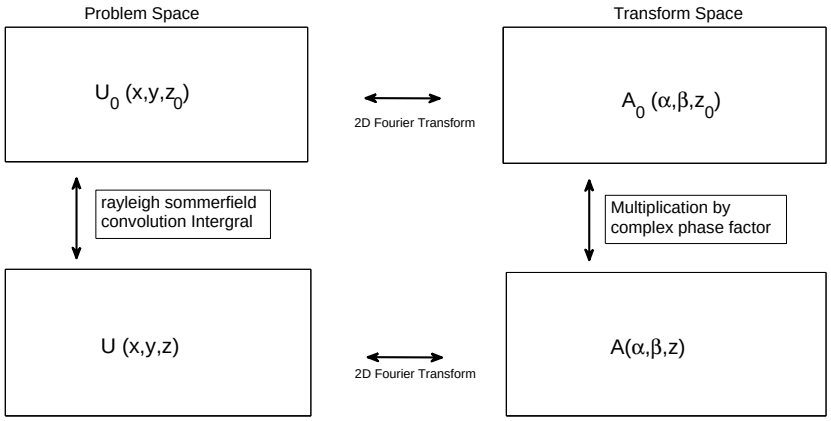

Figure 2.4: Flow diagram for the Fourier transform method to solve the diffraction problem.

The angular spectrum (AS) or plane wave spectrum (PWS) method has been shown to be equivalent to solving the the Rayleigh-Sommerfeld diffraction integral [36].

2.3 Discussion

The basic processes that occur in quasi three level lasers and amplifiers that operate in the long pulse (Q-switched) regime were presented. The stimulated emission and absorption processes depend on both the intensity of the light and the population density of ions in the region of interest. The non-linearity of these processes makes analytical solutions difficult.

The combination of the absorption (stimulated emission) process and scalar diffraction forms the basis for accounting for both gain and diffraction of a field through a gain medium. A numerical model that combines some of these processes to describe a laser amplifier is developed in the next chapter.

Chapter 3

Amplifier Model

The aim of the work reported in this chapter is to construct a mathematical model for a quasi-three level amplifier. By solving the equations governing the processes that take place in the laser gain medium and considering the necessary boundary condition approximate solutions can be found. The model is constructed with the intent that it should be easily modified to be applicable to modeling laser oscillators.

The non-linearity of the radiation transport equations means that finding exact analytical solutions are not generally possible [23]. A number of simplifying assumption can reduce the complexity of the problem. The complexity of this particular model is increased by spatial resolution and dimension of the variables. The effect of simplifying assumptions on the fidelity and accuracy of the model will be discussed in Chapter 4.

This chapter begins with a detailed description of a model of a two pass laser amplifier resolved in three spatial dimensions and time.

3.1 Description of the amplifier

An end-pumped amplifier may be modelled by the change of variables of the amplifier system as governed by the equations for the various processes that occur between variables. The variables include: the two complex fields that represent the scalar electric field at the seed wavelength, a complex field that represents the scalar pump beam, a real semi field that represents the density of ions in the upper laser level of the gain medium, and a real field that approximates the amplified spontaneous emission

(ASE). The amplifier's gain medium, as well as the seed and pump beams, are considered to have a specific geometry and confined to some region. The ASE field or rays are calculated in the active gain medium volume as discussed in this section.

While the model is quite general and could be applied to a large number of possible amplifiers, it is constructed to model a specific architecture. The double pass of the seed beam and single pass of pump beam through the gain medium are the practical limit for the specific Ho:YLF amplifier due to the properties of the beams and available optics and crystals [38, 3].

The results of the simulation of a double pass amplifier using this model are reported in Chapter 4. The comparison with the results of the experimental setup are reported in Chapter 5.

Seed Beam

The pulse train incident on and that propagates through the amplifier is defined by a complex field in some volume Ω_{seed}. Assuming rectangular symmetry this volume can be decomposed into a region of real space R^3,

$$\Omega_{seed} = [0, x_{seed}] \times [0, y_{seed}] \times [0, z_{seed}] \,,$$

were x_{seed}, y_{seed}, and z_{seed} are the size of the region where the seed beam is defined in the x, y, and z directions respectively. The pulse train propagated through the volume in a given time, described on the time interval Ω_t between t_0 and t_{end},

$$\Omega_t = [t_0, t_{end}] \,.$$

The monochromatic (with a wavelength λ_{seed}) pulse train or seed beam is described by the irradiance I_{seed} or intensity of the complex scalar field u_{seed} on a plane transverse to the direction of propagation z at one of the boundaries of $\Omega_{seed} \times \Omega_t$,

$$I_{seed}(x, y, z_0, t) = \frac{cn\epsilon_0}{2} u_{seed}\left(x, y, z_0, t\right) u^{\star}_{seed}\left(x, y, z_0, t\right) . \tag{3.1}$$

were ϵ_0 is the vacuum permittivity. On the boundary the beam will be assumed to be separable in time and space,

$$I_{seed}(x, y, z_0, t) = f_{seed}\left(x, y, z_0\right) P\left(t\right) , \tag{3.2}$$

were $f_{seed}(x, y, z_0)$ is the transverse intensity profile and $P(t)$ was the power in the beam. The intensity on the boundary $I_{seed}(x, y, z_0, t)$ is considered a boundary condition. The intensity elsewhere in the amplifier I_{seed} is a variable of the problem and was defined on $\Omega_{seed} \times \Omega_t$. The power density of the seed beam, ρ_{seed} is described by the photon density in the material,

$$\rho_{seed}(x, y, z, t) = \frac{I_{seed}(x, y, z, t)\, n}{h\nu_{seed} c}, \tag{3.3}$$

were c is the speed of light in the vacuum, n is the refractive index of the material, and $h\nu_{seed}$ is the energy per photon. The extrapolation to multiple seed beam is treated incoherently, for instance the intensity of two overlapping beams I_1 and I_2 is considered to be $I_1 + I_2$.

Pump Beam

The pump beam is described in a similar manner to the seed beam. The pump beam propagates through some pump volume Ω_{pump} on R^3,

$$\Omega_{pump} = [0, x_{pump}] \times [0, y_{pump}] \times [0, z_{pump}],$$

were x_{pump}, y_{pump}, and z_{pump} are the size of the volume in the x, y, and z directions respectively. The monochromatic pump beam (with a wavelength λ_{pump}) propagates through the volume on the same time interval Ω_t. The pump radiation that is incident on the pump volume is described by the irradiance or intensity of the scalar field on a plane transverse to the direction of propagation at one of the boundaries of $\Omega_{pump} \times \Omega_t$,

$$I_{pump}(x, y, z_0, t) = \frac{cn\epsilon_0}{2} u_{pump}(x, y, z_0, t)\, u^{\star}_{pump}(x, y, z_0, t).$$

On the boundary the beam will be assumed to be separable in time and space, i.e.

$$I_{pump}(x, y, z_0, t) = f_{pump}(x, y, z_0)\, P(t), \tag{3.4}$$

were $f_{pump}(x, y, z_0)$ is the transverse intensity profile and $P(t)$ is the power in the beam. The intensity on the boundary $I_{pump}(x, y, z_0, t)$ is considered a boundary condition. The intensity elsewhere in the amplifier I_{pump} is a variable of the problem and is defined on $\Omega_{pump} \times \Omega_t$. The power density of the

pump beam, ρ_{pump} is described by the photon density,

$$\rho_{pump}(x,y,z,t) = \frac{I_{pump}\,(x,y,z,t)\,n}{h\nu_{pump}c}, \tag{3.5}$$

were c is the speed of light in the vacuum, n is the refractive index, and $h\nu_{pump}$ is the energy per photon.

Gain medium

The gain medium with a slab geometry is defined in the volume Ω_{gain},

$$\Omega_{gain} = [0, x_{crysal}] \times [0, y_{crysal}] \times [0, l_{crysal}]. \tag{3.6}$$

This volume is assumed to be static. The active ions are doped into the crystal and have a density N_{active} that is assumed to be constant through the gain medium,

$$N_{\text{active}}\,(x,y,z,t) \equiv N_{\text{active}}.$$

In the model the manifold population densities, N_1,N_2,$N_3 \cdots N_i$, are variables that are defined in the volume Ω_{gain} and the time interval Ω_t. The thermal population of upper manifolds is negligible due to the large energy difference between the ground and excited manifolds. A reasonable set of initial conditions for the population densities are that only the ground state is populated at t_0 ,

$$N_i = 0, i \neq 1 \tag{3.7}$$

$$N_1 = N_{\text{active}}. \tag{3.8}$$

There are no boundary conditions for the population densities as the population densities have no explicit spatial dependence. The spatial variation of the populations are assumed to be produced by the difference in the temporal rate caused by the spatial distribution of seed and pump beams.

Active gain medium

The region of space where the active ions are excited is limited to the region where the gain medium interacts with the pump beam, $\Omega_{gain} \cap \Omega_{pump}$, and where it interacts with the seed beam, $\Omega_{gain} \cap \Omega_{seed}$. The area that is considered includes both these regions, i.e.,

$$\Omega_{active} = (\Omega_{gain} \cap \Omega_{pump}) \cup (\Omega_{gain} \cap \Omega_{seed}) . \tag{3.9}$$

For Holmium ions doped into YLF, the rate equations that govern of the population density of the lowest four energy manifolds are constructed by adding the rates for the processes that occur between the manifolds. The pump and laser radiation are absorbed and emit between the ${}^5I_8$ ground manifold (N_1) and the ${}^5I_8$ upper laser manifold (N_2). There are spontaneous decays from the excited levels and four energy transfer processes are considered. The rate equations for those processes for the manifold population densities N_4, N_3, N_2, and N_1 with the associated pump beam ρ_{pump} and seed beam ρ_{seed} are (for other formalisms of three level rate equations see [10, 17, 33]),

$$\frac{dN_4(x,y,z,t)}{dt} = -k_{4212}N_4(x,y,z,t)\,N_1(x,y,z,t) + k_{2124}N_2^2(x,y,z,t) - \frac{N_4(x,y,z,t)}{\tau_4} \tag{3.10}$$

$$\begin{aligned}\frac{dN_3(x,y,z,t)}{dt} &= k_{2123}N_2^2(x,y,z,t) - k_{3212}N_3(x,y,z,t)\,N_1(x,y,z,t) - \frac{N_3(x,y,z,t)}{\tau_3} \\ &\quad +\beta_{43}\frac{N_4(x,y,z,t)}{\tau_4}\end{aligned} \tag{3.11}$$

$$\begin{aligned}\frac{dN_2(x,y,z,t)}{dt} &= \frac{c}{n_{ylf}}\rho_{pump}(x,y,z,t)\left[-\sigma_{em}(\lambda_p)\,N_2(x,y,z,t) + \sigma_{ab}(\lambda_p)\,N_1(x,y,z,t)\right] \\ &\quad +\frac{c}{n_{ylf}}\rho_{seed}(x,y,z,t)\left[-\sigma_{em}(\lambda_s)\,N_2(x,y,z,t) + \sigma_{ab}(\lambda_s)\,N_1(x,y,z,t)\right] \\ &\quad +2k_{4212}N_4(x,y,z,t)\,N_1(x,y,z,t) + 2k_{3212}N_3(x,y,z,t)\,N_1(x,y,z,t) \\ &\quad -2\left(k_{2124}+k_{2123}\right)N_2^2(x,y,z,t) \\ &\quad -\frac{N_2(x,y,z,t)}{\tau_2} + \beta_{32}\frac{N_3(x,y,z,t)}{\tau_3} + \beta_{42}\frac{N_4(x,y,z,t)}{\tau_4}\end{aligned} \tag{3.12}$$

$$\begin{aligned}\frac{dN_1(x,y,z,t)}{dt} &= \frac{c}{n_{ylf}}\rho_{pump}(x,y,z,t)\left[\sigma_{em}(\lambda_p)\,N_2(x,y,z,t) - \sigma_{ab}(\lambda_p)\,N_1(x,y,z,t)\right] \\ &\quad +\frac{c}{n_{ylf}}\rho_{seed}(x,y,z,t)\left[\sigma_{em}(\lambda_s)\,N_2(x,y,z,t) - \sigma_{ab}(\lambda_s)\,N_1(x,y,z,t)\right] \\ &\quad -2k_{4212}N_4(x,y,z,t)\,N_1(x,y,z,t) - 2k_{3212}N_3(x,y,z,t)\,N_1(x,y,z,t) \\ &\quad +2\left(k_{2124}+k_{2123}\right)N_2^2(x,y,z,t) \\ &\quad +\frac{N_2(x,y,z,t)}{\tau_2} + \beta_{31}\frac{N_3(x,y,z,t)}{\tau_3} + \beta_{41}\frac{N_4(x,y,z,t)}{\tau_4}\end{aligned} \tag{3.13}$$

The rate equations are nonlinear and coupled to both the pump and seed beams. If the ions are constrained to these four levels due to rapid decay of higher manifolds by non-radiative decay then the population density of one of the levels is dependent on the others [11, 17, 10]. The ground level population density may be defined by the difference between the density of doped ions N_{active} and the density of ions in the excited manifolds,

$$N_1(x,y,z,t) \backsimeq N_{active}(x,y,z,t) - \sum_{i=2}^{4} N_i(x,y,z,t). \tag{3.14}$$

Traveling wave approximation

The solutions to the radiation transport equation have two notable features that are common to all hyperbolic partial differential equations [39]. The first is that it describes a conserved quantity, in this case that was the velocity of light as it travels through a medium. The other was that in the traveling wave approach to solving the radiation transport equations, the space and time dependence are decoupled but not necessarily independent.

The traveling wave technique is a standard method for solving hyperbolic partial differential equations that can reduce the partial differential equation to an ordinary differential equation in a transformed variable [39]. It is possible to decouple the spatial and temporal dependence of the radiation transport equation by a transform of co-ordinates from the lab frame $\hat{z}$ and $\hat{t}$ to the forward traveling wave frame z and t given by [23, 30],

$$z = \hat{z}, \tag{3.15}$$

$$t = \hat{t} - \frac{n}{c}\hat{z}, \tag{3.16}$$

and for the backward traveling wave,

$$z = \hat{z}, \tag{3.17}$$

$$t = \hat{t} + \frac{n}{c}\hat{z}. \tag{3.18}$$

The differential operators for the forward traveling beam becomes,

$$\frac{\partial}{\partial z} = \frac{\partial \hat{z}}{\partial z}\frac{\partial}{\partial \hat{z}} + \frac{\partial \hat{t}}{\partial z}\frac{\partial}{\partial \hat{t}} \tag{3.19}$$

$$\frac{\partial}{\partial z} = \frac{\partial}{\partial \hat{z}} + \frac{n}{c}\frac{\partial}{\partial \hat{t}}, \tag{3.20}$$

and

$$\frac{\partial}{\partial t} = \frac{\partial \hat{z}}{\partial t}\frac{\partial}{\partial \hat{z}} + \frac{\partial \hat{t}}{\partial t}\frac{\partial}{\partial \hat{t}}, \tag{3.21}$$

$$\frac{\partial}{\partial t} = \frac{\partial}{\partial \hat{t}}. \tag{3.22}$$

Similarly the operators for propagation in the reverse direction become,

$$\frac{\partial}{\partial z} = \frac{\partial}{\partial \hat{z}} - \frac{n}{c}\frac{\partial}{\partial \hat{t}}, \tag{3.23}$$

and

$$\frac{\partial}{\partial t} = \frac{\partial}{\partial \hat{t}}. \tag{3.24}$$

The radiation transport equation for the stimulated emission and absorption processes (Equation 2.10),

$$\frac{\partial I}{\partial z} - \frac{n}{c}\frac{\partial I}{\partial t} = I(\lambda)\left[\sigma_{em}(\lambda) N_2 - \sigma_{ab}(\lambda) N_1\right], \tag{3.25}$$

can now be decoupled from the time domain. For example the rate of change of a forward traveling beam, I^+, is transformed into an ordinary differential equation,

$$\frac{\partial I^+(x,y,z)}{\partial z} = I^+(x,y,z)\left[\sigma_{em} N_2(x,y,z,t) - \sigma_{ab} N_1(x,y,z,t)\right], \tag{3.26}$$

and a backward propagating beam, I^-, is transformed,

$$\frac{\partial I^-(x,y,z)}{\partial z} = -I^-(x,y,z)\left[\sigma_{em} N_2(x,y,z,t) - \sigma_{ab} N_1(x,y,z,t)\right]. \tag{3.27}$$

The transformed beams still depend on the time domain through the population densities (in the transformed co-ordinates). Both beams are described by a change of variable to the photon density,

for instance the intensity of the seed beam becomes $\rho_{seed}(x, y, z, t)$ at the wavelength λ_s,

$$\rho_{seed}(x, y, \hat{z}, \hat{t}) = \frac{I_{seed}\left(x, y, \hat{z}, \hat{t}\right) n}{h\nu_{seed} c}, \tag{3.28}$$

were $h\nu$ is the energy of the photon. The spatial derivatives are proportional,

$$\frac{\partial \rho_{seed}(x, y, z)}{\partial z} = \frac{\partial I_{seed}(x, y, z)}{\partial z} \frac{n}{h\nu_{seed} c}. \tag{3.29}$$

Propagation of the beam

The diffraction of either the seed or pump beam in the gain medium can be described in number of different ways. This work concentrates on three different approaches; the first approach is to treat the beam as non-diffracting, the second to define the radial distribution of the beam as it propagates, and the third to use a split step method to approximate the diffraction of the scalar electric field through the gain medium.

Non-diffracting method The first method treats the propagation of each transverse component of the beam through the gain medium independently as proposed by Rustad *et al* [33]. The incident beam $\rho_\lambda(x, y, z_0, t)$ at some wavelength λ is defined on the boundary $\Omega_{active} \times \Omega_t$ that will be considered to be the plane perpendicular to the propagation direction z at a position z_0. The photon density at any transverse position x_i and y_j on that plane, $\rho_\lambda(x_i, y_i, z_0, t)$, will obey Equations 3.26 and 3.28 along the line $s(x_i, y_i, z)$ and the are solved by separation of integration variables,

$$\frac{\partial \rho_\lambda(x_i, y_i, z)}{\rho_\lambda(x_i, y_i, z)} = \partial z \left(\sigma_{em}(\lambda) N_2(x_i, y_i, z, t) - \sigma_{ab}(\lambda) N_1(x_i, y_i, z, t)\right) \tag{3.30}$$

were N_2 and N_1 are the population densities of the upper and lower manifold of the transition, σ_{em} and σ_{ab} are the emission and absorption cross sections respectively. The solution at some other point $s(x_i, y_i, z_f)$ is solved using a line integration along s from $s(x_i, y_i, z_0)$ to that point,

$$\frac{\rho_\lambda(x_i, y_i, z_f, t)}{\rho_\lambda(x_i, y_i, z_0, t)} = exp\left[\int_{z0}^{zf} \sigma_{em}(\lambda) N_2(x_i, y_i, z, t) - \sigma_{ab}(\lambda) N_1(x_i, y_i, z, t)\, dz\right]. \tag{3.31}$$

Mode defined method The second approach is to define the transverse profile of the beam in the active volume as a normalized distribution or mode M_λ,

$$\rho_\lambda(x,y,z,t) = P_\lambda(z,t)\, M_\lambda(x,y,z)\, \frac{n}{h\nu c}, \tag{3.32}$$

and replace the intensity in Equation 3.26 with the power in each plane, $P_\lambda(z)$, as the variable,

$$\frac{n}{h\nu c}\frac{\partial\left(P_\lambda(z,t)\, M_\lambda(x,y,z)\right)}{\partial z} = \frac{n}{h\nu c} P_\lambda(z,t)\, M_\lambda(x,y,z)\left(\sigma_{em}(\lambda)\, N_2(x,y,z,t) - \sigma_{ab}(\lambda)\, N_1(x,y,z,t)\right).$$

Integration across the transverse plane followed by a change in the order of integration and differentiation gives

$$\frac{\partial P_\lambda(z,t)}{\partial z} = \iint_{\Omega_{active}} P_\lambda(z,t)\, M_\lambda(x,y,z)\left(\sigma_{em}(\lambda)\, N_2(x,y,z,t) - \sigma_{ab}(\lambda)\, N_1(x,y,z,t)\right) dA. \tag{3.33}$$

The solution is found by separation of variables and a line integral along the propagation axis

$$\frac{P_\lambda(z_f,t)}{P_\lambda(z_0,t)} = exp\left[\int_{z0}^{zf}\iint_{\Omega_{active}} M_\lambda(x,y,z)\left(\sigma_{em}(\lambda)\, N_2(x,y,z,t) - \sigma_{ab}(\lambda)\, N_1(x,y,z,t)\right) dA dz\right]. \tag{3.34}$$

Scalar diffraction method The third method is an extension to the scalar diffraction theory as discussed in Chapter 2. Consider a scalar electric field U that obeys the Helmholtz equation,

$$\left[\nabla^2 + k_0^2\right] U(x,y,z) \quad = \quad 0, \tag{3.35}$$

were k_0 is the free space wave number. In the slowly varying envelope approximation the fast oscillation of the electric electric field is separated from the spatial amplitude [23],

$$U = u(x,y,z)\, e^{-jk_0 z}.$$

The Laplacian is rewritten to depend only on the spatial amplitude,

$$\nabla^2 U = e^{-jk_0 z}\left[\frac{\partial^2}{\partial z^2} + \frac{\partial^2}{\partial x^2} + \frac{\partial^2}{\partial y^2} - 2ik_0\frac{\partial}{\partial z} - k_0^2\right] u.$$

It is possible to combine the linear gain term $g(x,y,z,t)$ and diffraction or diffusion effects in quasi-three level lasers and amplifiers [21, 40] by modifying the Helmholtz equation. The gain for the beam is expressed in terms of the populations densities,

$$g(x,y,z) = \sigma_{em}(\lambda) N_2(x,y,z,t) - \sigma_{ab}(\lambda) N_1(x,y,z,t). \tag{3.36}$$

The addition of the gain terms are included in the Helmholtz equation[40] resulting in an in-homogeneous equation,

$$ikgu(x,y,z) = \left(\frac{\partial^2}{\partial z^2} + \frac{\partial^2}{\partial x^2} + \frac{\partial^2}{\partial y^2} - 2ik\frac{\partial}{\partial z}\right) u(x,y,z) \tag{3.37}$$

were k is the wave number in the material, $k = nk_0$, with refractive index n. For laser beams propagation under the para-axial approximation the second derivative is much smaller than the first derivative in the propagation direction, $\frac{\partial^2 \tilde{u}}{\partial z^2} \ll 2ik_0\frac{\partial \tilde{u}}{\partial z}$. An iterative solution for the evolution of the electric field may be expressed as a symmetric first order split step operator [22, 40],

$$u(x,y,z+\Delta z) = exp\left[-\frac{i\Delta z}{4k}\nabla_\perp^2\right] exp\left[\frac{g}{2}\Delta z\right] exp\left[-\frac{i\Delta z}{4k}\nabla_\perp^2\right] u(x,y,z), \tag{3.38}$$

were $\nabla_\perp^2$ is the transverse Laplacian. The $exp\left[-\frac{i\Delta z}{4k}\nabla_\perp^2\right]$ term diffracts the beam a distance $\frac{\Delta z}{2}$. This operator represents the diffraction of the amplitude under similar conditions to Fresnel diffraction. In this work that operator will be replaced by the angular spectrum operator (Equation 2.62). The symmetric operator becomes [26]

$$u\left(x,y,z+\frac{\Delta z}{2}\right) = e^{\frac{g\left(x,y,z+\frac{\Delta z}{2}\right)}{2}\Delta z}\mathcal{F}:\left\{\mathcal{F}:\{u(x,y,z)\}e^{ik\frac{\Delta z}{2}\sqrt{1-(\alpha^2+\beta^2)}}\right\}, \tag{3.39}$$

$$u(x,y,z+\Delta z) = \mathcal{F}:\left\{\mathcal{F}:\left\{u\left(x,y,z+\frac{\Delta z}{2}\right)\right\}e^{ik\sqrt{1-(\alpha^2+\beta^2)}\frac{\Delta z}{2}}\right\}. \tag{3.40}$$

This operator requires four Fourier transforms which make the operator computationally expensive. However, this operator can accurately model diffraction effects for propagation distances that are small in comparison with the radius of the beam in question[41].

A numerical approach is taken to solve these equations as well as the rate equations for the population densities in the next section.

Mirrors

The spatial amplitude "traveling" in the positive direction reflected by mirrors was approximated by a parabolic phase function [20],

$$u^{-}(x,y,z_0) = \sqrt{R}\, exp\left[ik_0\left(\frac{x^2}{r_x}+\frac{y^2}{r_y}\right)\right]\, u^{+}(x,y,z_0)\,,$$

were R is the reflectivity of the mirror, and r_x and r_y are the radii of curvature in the x and y planes respectively.

Amplified spontaneous emission

ASE has been shown to degrade amplifier and laser performance and reduce the storage of energy in the gain medium [28, 42, 23]. Power from the spontaneous emission in the gain medium stimulates emission from ions in the upper laser level which in turn leads to amplification as the light travels through the medium. The power generated this way cannot be extracted and is lost from the system.

The discussion that follows is based on the work of [23, 29, 42] on the amplification of narrow bandwidth spontaneous emission that is expanded to deal with the broad gain spectrum of Ho:YLF. To calculated of ASE output of the amplifier or laser consider a small region of the gain medium that has a density of ions in the upper laser manifold N_2. The power emitted by spontaneous radiative decay by the volume dV is calculated by

$$P_{sp} = N_2 \gamma_{sp} h\nu dV, \tag{3.41}$$

were γ_{sp} is the radiative decay rate of the upper level, $h\nu$ is the energy of the decay photon, and $N_2 dV$ is the number of ions in the upper laser manifold in the volume. Spontaneous emission from the upper manifold may have a broad spectrum in three level lasers and amplifiers. The spectral distribution of power generated by spontaneous emission between the upper and lower laser manifolds can be found by rearranging the Füchtbauer–Ladenburg equation [9, 30, 14]

$$\sigma^{\alpha}_{em}(\lambda) \;=\; \frac{\lambda^5}{8\pi n^2 c \frac{\tau_{sp}}{\beta}} \frac{P^{\alpha}_{sp}(\lambda)}{\int \lambda P^{\alpha}_{sp}(\lambda)\, d\lambda}, \tag{3.42}$$

were α is the polarisation of the light, P^{α}_{sp} is the power of the spontaneous emission field, n is the refractive index of the material, λ is the wavelength of the light, τ_{sp} is the spontaneous emission

lifetime of the upper laser manifold, $\sigma_{em}^{\alpha}(\lambda)$ is emission cross section, and β is the branching ratio for the spontaneous emission between the two manifolds. The distribution of power into the emission spectrum depends on the cross section,

$$\tilde{P}_{sp}^{\alpha}(\lambda) \propto \frac{\sigma_{em}^{\alpha}(\lambda)}{\lambda^5}. \tag{3.43}$$

In Ho:YLF the power distribution of each polarisation is such that $\frac{2}{3}$ of the power is emitted into the σ polarisation and $\frac{1}{3}$ into the π polarisation [14]. Therefore,

$$\tilde{P}_{sp}^{\alpha}(\lambda) = \frac{\frac{\sigma_{em}^{\alpha}(\lambda)}{\lambda^5}}{\int \lambda \left(\frac{1}{3}\frac{\sigma_{em}^{\pi}(\lambda)}{\lambda^5}(\lambda) + \frac{2}{3}\frac{\sigma_{em}^{\sigma}(\lambda)}{\lambda^5}(\lambda)\right) d\lambda}. \tag{3.44}$$

In this work it is assumed that the power is radiated in all directions for both polarizations into the normalized spectral distribution. The power per unit solid angle per wavelength interval at a position R_i in the active region Ω_{active} is given by combining equations 3.44 and 3.41,

$$P_{sp}^{\alpha}(R_i, \lambda) = \frac{N_2(R_i)\gamma h\nu dV}{4\pi} P_{sp}^{\alpha}(\lambda). \tag{3.45}$$

The ASE radiation is approximated by a set of plane waves with a decreasing amplitude emitted into the full solid angle. The ASE intensity is constructed by considering the amplification of the power of the ASE radiation passing through the active region. The power amplification of radiation between R_i and R_j occurs along the vector $R = R_j - R_i$ and is approximated by a line integral of equation 2.10 along R,

$$G(R_i, R_j, \lambda) = \int -\sigma_{ab}(\lambda) N_g(R_i + R) + \sigma_{em}(\lambda) N_{ex}(R_i + R)\, dr. \tag{3.46}$$

The solid angle that the power is emitted into is given by the common approximation between the area of the surface that the power passing through A_j and the length of the vector,

$$\Delta\Omega(R_j, R_i) = \frac{A(R_j, R_i)}{R^2}. \tag{3.47}$$

The intensity of the ASE at R_j due to the power emitted at R_i is given by the amplified power per

steradians divided by the area that it fills,

$$I_{ase}\left(R_i, R_j, \lambda\right) = \frac{\Delta\Omega\left(R\right)}{A\left(R_j, R_i\right)} G\left(R_i, R_j, \lambda\right) P_{ase}\left(R_i, \lambda\right), \tag{3.48}$$

$$= \frac{1}{R^2} G\left(R_i, R_j, \lambda\right) P_{ase}\left(R_i, \lambda\right). \tag{3.49}$$

The intensity of the ASE in the gain volume is calculated by integration of the intensity $I_{ase}\left(R_i, R_j\right)$ from each volume in the gain volume,

$$I_{total}\left(R_j, \lambda\right) = \iiint_{\Omega_{active}} I_{ase}\left(R_i, R_j, \lambda\right) dV. \tag{3.50}$$

The rate equation for the absorption and stimulated emission of the ASE radiation between the upper and lower laser manifolds is determined by integrating Equation 2.10 over the spectrum of the ASE radiation,

$$\frac{dN_2\left(R_j\right)}{dt} = \frac{c}{n} \int_{\lambda_{manifold}} I_{total}\left(R_j, \lambda\right) \left[-\sigma_{em}\left(\lambda\right) N_2\left(R_j\right) + \sigma_{ab}\left(\lambda\right) N_1\left(R_j\right)\right] d\lambda, \tag{3.51}$$

$$\frac{dN_1\left(R_j\right)}{dt} = -\frac{dN_2}{dt}. \tag{3.52}$$

3.2 Three dimensional time resolved numerical model

The choice of method to solve the problem may vary significantly depending on the particular boundary conditions imposed, as well as on any other restraints that may be imposed on the variables. The approach taken to solve the problem as described above was to approximate the solution using a numerical method. In this section the numerical model is outlined.

Approximation of the gain medium by constant volumes

The population densities $N_i\left(x, y, z, t\right)$ in the gain volume, $\Omega_{gain} \times \Omega_t$ are approximated on a mesh Ω_{mesh} and with nodes at,

$$u(x, y, z, t) \simeq u\left(h_x\left(i - \frac{1}{2}\right), h_y\left(j - \frac{1}{2}\right), h_z\left(k - \frac{1}{2}\right), h_t\left(l\right)\right), \tag{3.53}$$

which cover the volume as the indices i, j and k run from 1 to N_x, N_y, N_z, N_t over the spatial dimensions z , y and z of the problem. The distances between the nodes in each spatial dimension are,

$$h_x = \frac{x_{crystal}}{N_x}, \tag{3.54}$$

$$h_y = \frac{y_{crystal}}{N_y}, \tag{3.55}$$

$$h_z = \frac{l_{crystal}}{N_z}, \tag{3.56}$$

while each node was considered to be at the center of a volume, $V = h_x h_y h_z$.

The seed generated by a Q-switched laser is typically periodic with a short pulse followed by a long period with no power. When considering periodically pulsed seed beams the time interval can be broken up into periods. This period consists of two intervals, the interval containing the laser pulse and a long interval with no seed power,

$$\Omega\left(t+T\right) = \begin{cases} \Omega_{pump} & T_a \leq |t+T| \leq T_b \\ \Omega_{pulse} & T_a \geq |t+T| \geq T_b \end{cases}, \tag{3.57}$$

were T is the period of the pulse, T_b is the start of the pulse phase and T_a is the end of the pulse phase. The use of these intervals simplifies the rate equations, for instance if the seed pulse is zero the rate of change of the seed beam is identically zero.

The population density of $N\left(x,y,z,t\right)$ is approximated by $N\left(i,j,k,l\right)$ at each node $u\left(i,j,k,l\right)$. The population density at each node is treated as constant over the small volume, V. Assuming the population densities are constant reduces the complexity of the system. The justification is that the population densities have no explicit dependence on the spatial domains under the assumptions made in the description of the problem. The volume that is constant decreases as the number of nodes in the model increases.

The photon density of the pump and seed beams are approximated on a grid that is bigger by one element in the z direction, $N_z + 1$, with nodes at,

$$\rho_\lambda\left(x,y,z,t\right) \simeq \rho_\lambda\left(h_x\left(i-\frac{1}{2}\right), h_y\left(j-\frac{1}{2}\right), h_z\left(k-1\right), h_t\left(l\right)\right). \tag{3.58}$$

Between each node $\rho_\lambda\left(i,j,k,l\right)$ and the next along the propagation direction(z) $\rho_\lambda\left(i,j,k\pm1,l\right)$ the

population density is represented by $N(i,j,k,l)$. This simplifies the solution of the radiation transport equation or the scalar diffraction method for the laser or pump field as discussed below.

Non-diffracting beam

In the previous section three different propagation theories were outlined, these methods can be applied to the approximated population densities. In the non-diffracting theory the propagation of either the seed or pump beam in the positive direction is given by the change of photon density at each transverse point, Equation 3.31

$$\frac{\rho_\lambda(x_i,y_i,z_f,t)}{\rho_\lambda(x_i,y_i,z_0,t)} = exp\left[\int_{z_0}^{z_f} \sigma_{em}(\lambda) N_2(x_i,y_i,z,t) - \sigma_{ab}(\lambda) N_1(x_i,y_i,z,t)\, dz\right]. \tag{3.59}$$

The cross sections $\sigma_{em,ab}$ are considered constant for this work. This means that evaluating the integral from node to node is trivial,

$$\frac{\rho_\lambda^+(i,j,k+1,l)}{\rho_\lambda^+(i,j,k,l)} = e^{(\sigma_{em}N_2(i,j,k,l)-\sigma_{ab}N_1(i,j,k,l))\int_{z0}^{zf} dz}, \tag{3.60}$$

$$= e^{(\sigma_{em}N_2(i,j,k,l)-\sigma_{ab}N_1(i,j,k,l))h_z}. \tag{3.61}$$

The reverse propagation is solved by applying Equation 3.31,

$$\frac{\rho_\lambda^-(i,j,k-1,l)}{\rho_\lambda^-(i,j,k,l)} = e^{(\sigma_{em}N_2(i,j,k,l)-\sigma_{ab}N_1(i,j,k,l))\int_{zf}^{zo} dz} \tag{3.62}$$

$$= e^{(\sigma_{em}N_2(i,j,k,l)-\sigma_{ab}N_1(i,j,k,l))h_z}. \tag{3.63}$$

Propagation of the beam from one plane to the next is completed by computing the change between each pair of transverse nodes.

Mode defined beams

The mode is defined on the same grid as the photon density,

$$M_\lambda(x,y,z) \simeq M_\lambda(i,j,k), \tag{3.64}$$

and the power of the beam along the propagation axis is defined as,

$$P_\lambda(z,t) \simeq P_\lambda(k,l). \tag{3.65}$$

The profile of the photon density is defined on the grid by,

$$\rho_\lambda(i,j,k,l) = P_\lambda(k,l)\, M_\lambda(i,j,k)\, \frac{n}{h\nu c}. \tag{3.66}$$

Approximation of the integration across the transverse plain gives,

$$\frac{\Delta P_\lambda(k,l)}{\Delta z} = h_x h_y P_\lambda(k,l) \sum_i^{N_x} \sum_j^{N_y} M_\lambda(i,j,k) \left(\sigma_{em}(\lambda)\, N_2(i,j,k,l) - \sigma_{ab}(\lambda)\, N_1(i,j,k,l)\right). \tag{3.67}$$

The solution is found by separation of variables and a line integral along the propagation axis,

$$\frac{P_\lambda(k+1,l)}{P_\lambda(k,l)} = \exp\left[h_z h_x h_y \sum_i^{N_x} \sum_j^{N_y} M_\lambda(i,j,k) \left(\sigma_{em}(\lambda)\, N_2(i,j,k,l) - \sigma_{ab}(\lambda)\, N_1(i,j,k,l)\right)\right]. \tag{3.68}$$

Numerical angular spectrum method

The implementation of the split step method to solve for the diffraction of the scalar electric field between the two planes ,

$$
\begin{aligned}
u\left(x,y,z+\frac{\Delta z}{2}\right) &= \mathcal{F}:\left\{\mathcal{F}:\left\{u\left(x,y,z\right)\right\}e^{ik\sqrt{1-(\alpha^2+\beta^2)}\frac{\Delta z}{2}}\right\},\\
u\left(x,y,z+\Delta z\right) &= \mathcal{F}:\left\{e^{ik\sqrt{1-(\alpha^2+\beta^2)}\frac{\Delta z}{2}}\mathcal{F}:\left\{e^{\frac{g\left(x,y,z+\frac{\Delta z}{2}\right)}{2}\Delta z}u\left(x,y,z+\frac{\Delta z}{2}\right)\right\}\right\}, \qquad (3.69)
\end{aligned}
$$

is approximated with the use of the two dimensional Fast Fourier transform (2D FFT) to approximate the two dimensional Fourier transform and a discrete phase factor [26, 43, 37, 36, 41],

$$
\begin{aligned}
u\left(i,j,k+\frac{1}{2}\right) &= \mathsf{FFT}^{-1}\left\{\mathsf{FFT}\left\{u\left(i,j,k\right)\right\}e^{ik\sqrt{1-\left(\alpha_i^2+\beta_j^2\right)}\frac{h_z}{2}}\right\}, \qquad (3.70)\\
u\left(i,j,k+1\right) &= \mathsf{FFT}^{-1}\left\{e^{ik\sqrt{1-\left(\alpha_i^2+\beta_j^2\right)}\frac{h_z}{2}}\mathsf{FFT}\left\{e^{\frac{g(i,j,k)}{2}h_z}u\left(i,j,k+\frac{1}{2}\right)\right\}\right\}. \qquad (3.71)
\end{aligned}
$$

The 2D FFT is a numerical method and has an associated error. The error has been shown to be linked to the sampling requirements and aliasing conditions [41, 43, 24]. These requirements are analogous to the sampling condition (Whittaker, Kotelnikov, Nyquist, Shannon) in signal processing [44]. The sampling distance, $h_{x,y}$, is linked to the number of samples, $N_{x,y}$, in the sampling window, $S_{x,y}$ by

$$
S_{x,y} = N_{x,y}h_{x,y}. \qquad (3.72)
$$

The sampling condition relates the maximum frequency that can be resolved to

$$
f_{nyq} = \frac{1}{2h_{x,y}}, \qquad (3.73)
$$

and limits the cosine spectrum to

$$
\alpha_{nyg} = \lambda f_{nyq}. \qquad (3.74)
$$

The minimum number of samples of the transfer function or propagation kernel is given by[43]

$$N_{x,y} \geq \frac{2\lambda h_z}{h_{x,y}\sqrt{4h_{x,y}^2 - \lambda^2}}, \tag{3.75}$$

For longer propagation distances placing a band limitation on the angular spectrum limits some aliasing errors [45],

$$f = \frac{\alpha}{\lambda} \leq \frac{1}{\lambda}\sqrt{1 + \frac{4z^2}{\left(N_{x,y}h_{x,y}\right)^2}}. \tag{3.76}$$

Each of the three methods considered and used to propagate the seed and pump beam though the gain medium by iteration between each transverse plane. The results are presented and discussed in Chapter 5.

Population Densities

The approach to approximate a solution for the rate equations for the population densities of the active ions $N_i(i,j,k,l)$ with a numerical integration technique. The type of numerical method used has effects on the stability and accuracy for a given time step. Implicit methods typically have better stability but are more computationaly intensive compared to explicit methods. Both types of methods are investigated in Section 4.3. For example the evolution of a system of ordinary differential equation's are calculated with the explicit Euler method with a round off error $O(h_z^2)$,

$$N_4\left(i,j,k,l+1\right) = N_4\left(i,j,k,l\right) + h_t\left(-k_{4212}N_4N_1 + k_{2124}N_2^2 - \frac{N_4}{\tau_4}\right) + O(h_t^2) \tag{3.77}$$

$$N_3\left(i,j,k,l+1\right) = N_3\left(i,j,k,l\right) + h_t\left(k_{2123}N_2^2 - k_{3212}N_3N_1 - \frac{N_3}{\tau_3} + \beta_{43}\frac{N_4}{\tau_4}\right) + O(h_t^2) \tag{3.78}$$

$$\begin{aligned} N_2\left(i,j,k,l+1\right) = {} & N_2\left(i,j,k,l\right) + h_t\frac{c_o}{n_{ylf}}\rho_{pump}[-\sigma_{em}\left(\lambda_p\right)N_2 + \sigma_{ab}\left(\lambda_p\right)N_1] \\ & + h_t\left(2k_{4212}N_4N_1 + 2k_{3212}N_3N_1 - 2\left(k_{2124}+k_{2123}\right)N_2^2\right) \\ & + h_t\left(\frac{c_o}{n_{ylf}}\rho_{seed}[-\sigma_{em}\left(\lambda_s\right)N_2 + \sigma_{ab}\left(\lambda_s\right)N_1] - \frac{N_2}{\tau_2} + \beta_{32}\frac{N_3}{\tau_3} + \beta_{42}\frac{N_4}{\tau_4}\right) \\ & + O(h_t^2) \end{aligned} \tag{3.79}$$

$$N_1\left(i,j,k,l+1\right) = N_{tm} - \sum_{i=2}^{4} N_i\left(i,j,k,l+1\right) \tag{3.80}$$

were $\rho_{pump} = \rho^{+}_{pump} + \rho^{-}_{pump}$ and $\rho_{seed} = \rho^{+}_{seed} + \rho^{-}_{seed}$. For the specific gain medium, Ho:YLF, the system was further simplified by assuming that N_4 and N_3 are very small in comparison to N_2 and N_1 [11, 17]. This assumption was based on the fact that the fluorescence lifetime of these levels depopulates the levels faster than they are pumped by energy transfer upconversion. Additionally the non-radiative decay branches into the N_2 manifold via the N_3 manifold with close to 100% efficiency[11],

$$\begin{aligned} N_2\left(i,j,k,l+1\right) &= N_2\left(i,j,k,l\right) + h_t\frac{c_o}{n_{ylf}}\rho_{pump}[-\sigma_{em}\left(\lambda_p\right)N_2 + \sigma_{ab}\left(\lambda_p\right)N_1] \\ &\quad + h_t\left(\frac{c_o}{n_{ylf}}\rho_{seed}[-\sigma_{em}\left(\lambda_s\right)N_2 + \sigma_{ab}\left(\lambda_s\right)N_1] - \frac{N_2}{\tau_2}\right) \\ &\quad - h_t\, k_{\Sigma ho}\, N_2^2 + O(h_t^2) \end{aligned} \tag{3.81}$$

$$N_1\left(i,j,k,l+1\right) = N_{tm} - \sum_{i=2}^{2} N_i\left(i,j,k,l+1\right), \tag{3.82}$$

were $k_{\Sigma ho}$ is the effective upconversion rate[33].

Amplified spontaneous emission model

For the purpose of the calculation of the ASE power gain it is useful to calculate the gain distribution,

$$g\left(r,\lambda\right) = -\sigma_{ab}\left(\lambda\right)N_g\left(r\right) + \sigma_{em}\left(\lambda\right)N_{ex}\left(r\right). \tag{3.83}$$

The power gain for the ASE field is calculated by the line integral from R_i along some vector R,

$$G\left(R_i,R,\lambda\right) = \int_{R_i} g\left(r,\lambda\right)dR. \tag{3.84}$$

The line integrals have the same form as the three dimensional Radon transform of $g\left(r,\lambda\right)$ for a fixed value of the wavelength. This method (and particularly the inverse transform) is applied to tomography and other imaging systems. In this context the integral is interpreted as numerical Radon transform [46, 47].

3.3 Discussion

The amplifier has been described in terms of its components, the coupled equations that link them and the boundary conditions. The description of the pump and seed beam are similar, the differences are mainly in the properties of the fields or particular boundary conditions and the influence of those properties on the behavior in the gain medium.

The propagation of either beam through the gain medium has been treated in three different ways: linear non diffracting method, split step angular spectrum method for diffracting beams and a "mode" confined method.

The various methods used in the model fall into a more general class of numerical methods for partial differential equations. The temporal method is a method of lines approach to solving the non-linearity (temporal) in the coupled rate equations. The split step angular spectrum method is a Fourier transform based spectral method.

The model has features that have allowed for an accurate description of Ho:YLF slab amplifiers due to the three dimensional approach. The Cartesian co-ordinate system allows for the modeling of slab amplifiers that have different beam characteristics in different planes. The results of the simulation of a Ho:YLF amplifier are reported in Chapter 4.

The numerical requirements and restrictions of the model are linked to the chosen numerical methods. This included the requirements on the resolution of the optical fields that within the context of a numerical model limits the possible fields that could be expressed. The model has resolution of the gain medium along the propagation direction that allows for accurate calculation of the absorption of the pump beam.

There are also limitations introduced by solid state laser theory and some of the simplifying assumptions made. The modelling of the amplification of short temporal pulses is limited by the assumptions made in the Reciprocity Method.

Some noticeable effects are not considered such as the effect of temperature on the gain medium parameters such as the dependence of the cross sections on temperature [1, 9], and the change of refractive index with temperature.

Both the transient and persistent behavior are of interest. The transient analysis (as proposed in this chapter) would for instance be useful for simulating whether suppression of the first pulse was

necessary. Periodic boundary conditions could possibly be more accurate due to seed and pump beams periodicity.

The numerical model was implemented in the computational environment MATLAB [48], and all the simulations presented in this thesis were computed in that environment.

Chapter 4

Design of a high energy Ho:YLF slab amplifier

4.1 Introduction

The design of power amplifier stages requires integration of information about the components of the system and predicted behavior of the completed system. The numerical model that was developed in Chapter 3 is used to simulate the behavior of an amplifier that was constructed from a particular pump laser and a particular seed laser [49, 50]. In effect the choice of these lasers limited the number and range of model parameters.

The first section of this chapter begins with a description of the properties of the amplifier: the Ho:YLF gain medium, the pump laser and the seed laser. The accurate representation of an amplifier by the simulation depends on the accuracy of the description of the seed and pump beams incident on the amplifier, as well as the material properties of the Ho:YLF gain medium.

Section 4.3 presents the results of the error analysis of the amplifier model. This includes analysis of error and accuracy of the model. The analysis is discussed with the use of an example of a single parameter set. The large number of parameters used to represent the amplifier system leads to complicated error analysis.

The results and analysis of the simulation of a particular amplifier system are subsequently presented in detail. The solutions of the amplifier model contain a large amount of data. The representation of

the data in reduced form is illustrated with the use of an example.

Predictions of general trends of amplifier performance with respect to design parameters are presented next. In turn the effects of pump wavelength, mode matching and beam size, and crystal length on the amplifier performance are simulated. While this represents a subsection of the possible configurations it covers the major parameters possible with the given physical seed and pump lasers. The exception was the seed polarisation that was excluded due to concern over the distortion of the seed beam by the strong thermal lens on the π polarisation of the slab YLF crystals (the π polarisation and crystal c-axis parallel with the small axis of the slab).

Comparison of the model with an experimental amplifier system is discussed in Chapter 5. Further energy scaling schemes are addressed in Chapter 6.

4.2 Amplifier properties

The top down description of the amplifier given below starts with the geometry and layout of the components, then proceeds with the properties of the Ho:YLF gain medium, the pump beam, and the seed beam.

4.2.1 Geometry and layout

In the model of the amplifier the seed beam passed through the gain medium from the right and was reflected back by a dichoric mirror. The pump beam was incident on the amplifier gain medium through a dichoric mirror from the left ($+\hat{z}$). Alignment of the optical axis of the seed and pump beam was assumed to be perfect in both angle and offset. Ho:YLF crystals with slab geometry were used to accommodate the assumed elliptical pump beam, Figure 4.1 shows a schematic of the amplifier with elliptical or elongated non-diffracting beams.

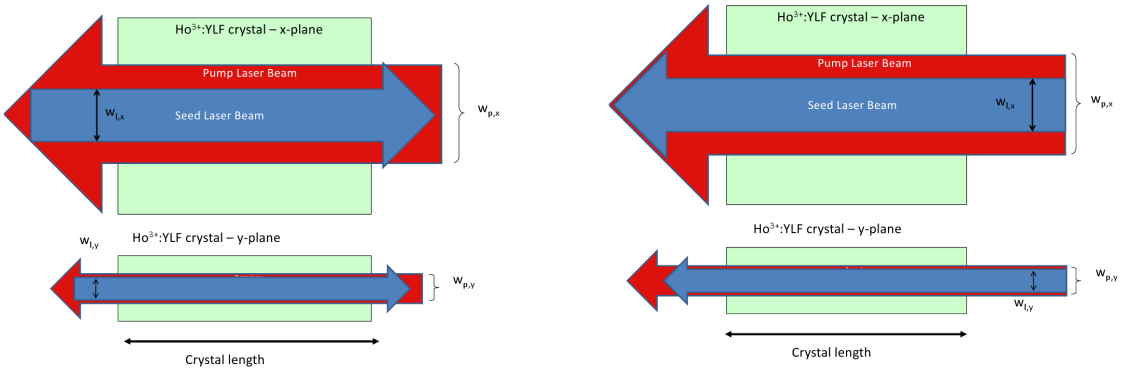

Figure 4.1: Schematic of the two passes of the amplifier showing the beam sizes in the horizontal and perpendicular planes and the amplifier length. Right, the first pass with the pump and seed beams traveling opposite directions. Left, the second pass with the beams traveling in the same direction.

There were two possibilities for the configuration of a two pass amplifier due to direction of propagation of the seed and pump beam in the amplifier. Figure 4.1 shows the first possibility were the pump and seed (first pass) beams propagated in the opposite direction. The second possibility was that the pump and seed propagated in the same direction. Amplifiers with the first layout are discussed in this chapter.

The use of crystals with a slab geometry has been noted to have improved the thermal management and reduced thermal fracture limits in comparison with crystals in a rod geometry [51]. It also provides a potentially scalable architecture. This has been demonstrated in other materials[52]. Scalability of slab geometries will be investigated in Chapter 6.

4.2.2 Ho:YLF spectra and optical properties

YLF is an uni-axial crystal with a tetragonal structure [14, 11]. In this work only linear polarisations that were aligned with the crystal axis are considered. In an a-cut YLF crystal there are then two polarizations of a transverse electric field aligned this way, σ and π. The electric field component is parallel with the c-axis for the π polarization while it is perpendicular to the c axis for the σ polarization. YLF is birefringent, the refractive index in the 2 μm region is assumed to be $n_\pi = 1.47$ and $n_\sigma = 1.44$ [9, 14].

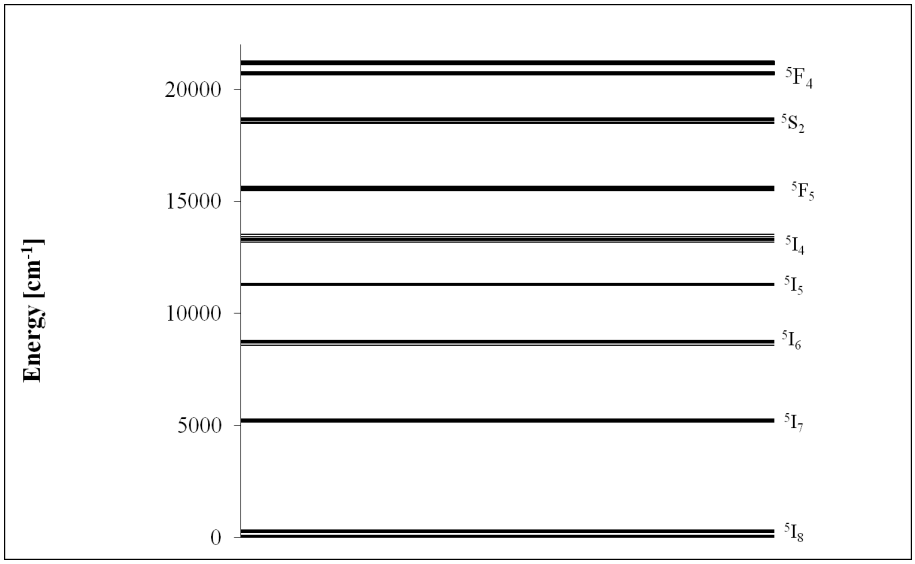

Figure 4.2: Theoretical energy levels of Ho^{3+}:YLF in cm^{-1} [1]. Some of the Stark levels are distinguishable within the manifolds.

The energy levels of the valence electrons of Ho:YLF are highly degenerate. The degeneracy is lifted by interaction of the active ion with the crystal field that splits the energy levels into manifolds of Stark levels [14]. The first few manifolds of Ho:YLF are shown in Figure 4.2.

Manifold	$^5I_8$	$^5I_7$	$^5I_6$	$^5I_5$	$^5I_4$	$^5F_5$	$^5S_2$	$^5F_4$	$^5F_3$	$^5F_2$
Stark Level										
1	0	5153.3	8669.7	11242.2	13188.3	15488.8	18491.9	18602.0	20642.6	21127.7
2	6.8	5157.2	8670.1	11242.8	13269.3	15493.9	18496.5	18604.9	20666.5	21135.2
3	24.6	5163.3	8677.3	11245.4	13321.1	15511.2	18521.4	18617.2	20714.0	21173.7
4	47.8	5165.3	8682.3	11250.6	13340.8	15552.8	18525.8	18680.6	20762.2	21227.4
5	55.2	5184.5	8585.6	11252.1	13349.1	15624.3		18684.1	20768.8	
6	74.7	5205.3	8693.5	11304.3	13412.5	15635.4		18703.7		
7	211.3	5227.3	8699.5	11332.0	13536.8	15641.8		18711.9		
8	269.8	5232.7	8768.8	11338.3		15660.8				
9	273.9	5288.4	8783.4							
10	279.2	5290	8796.5							
11	294.2	5291.1								
12	301.3									
13	317.9									

Table 4.1: Theoretical Stark Level Energies of Ho^{3+}:YLF in cm^{-1}. [1].

Table 4.1 groups the energy levels by manifold. Operation in the 2 μm wavelength region occurs between the $^5I_8$ ground manifold and the first excited manifold $^5I_7$. This laser scheme that relies on the splitting of one of the laser levels are called a quasi-three level laser scheme. The pumping scheme

where the pump radiation is absorbed by the ground manifold exciting an electron into the upper laser manifold are typically named in-band pumping.

The active ions have different rates for the absorption and stimulated emission processes for beams of different polarisations. The emission and absorption cross sections were used extensively as parameters for the numerical simulation as they determined the rate at which power in an optical beam was absorbed and emitted between levels. The measured emission and absorption cross sections between the ${}^5I_7$ and ${}^5I_8$ manifolds are shown in Figure 4.3. The experiment was performed at room temperature [2].

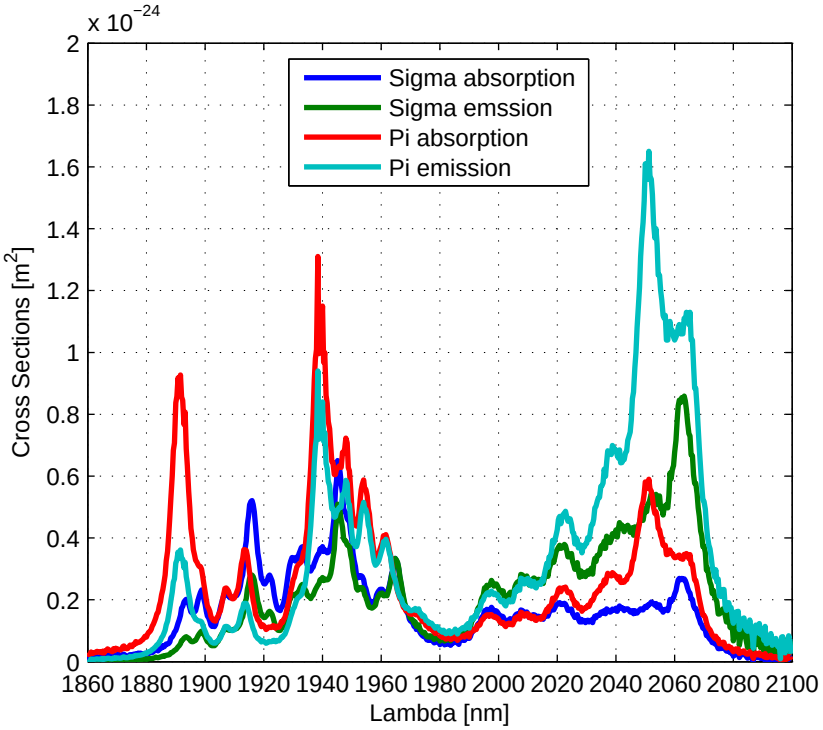

Figure 4.3: Ho:YLF spectra from 1870 nm to 2100 nm. The optical transition takes place between the ground manifold ${}^5I_8$ and the first excited manifold ${}^5I_7$. [2]

The spectra shows strong absorption with three main peaks at 1888 nm and 1938 nm on the π polarization and at 1914 nm on the σ polarization. The cross over point λ_u occurs at 1977 nm. The peaks in the emission spectrum occur at 2050 nm on the π polarization and at 2065 nm on the σ polarization.

Comparison between the spectra of three different Ho:YLF samples shows large variations in both the absorption and the calculated emission [9, 2, 1]. The difference in the reported cross sections was a concern due to the sensitivity of the model on this parameter, as well as the influence of temperature.

The reciprocity method gives the effect of temperature changes on the ratio between the cross sections

of the ${}^5I_7 \rightarrow {}^5I_8$ transition, see equation 2.8. While the relative values of the emission and absorption cross section are fixed at a certain temperature by the reciprocity principle, both the absorption and the emission cross sections may vary with the temperature of the host medium. With increasing temperature the absorption cross section will be closer to the emission cross section and there will be a reduction in gain at long wavelength and reduced absorption at short wavelengths. To demonstrate this effect Figure 4.4 shows the ratio of the absorption and emission cross sections at a typical laser wavelength of 2064 nm and and a pump wavelength of 1888 nm for temperatures from 200 to 500 K as calculated by Equation 2.8.

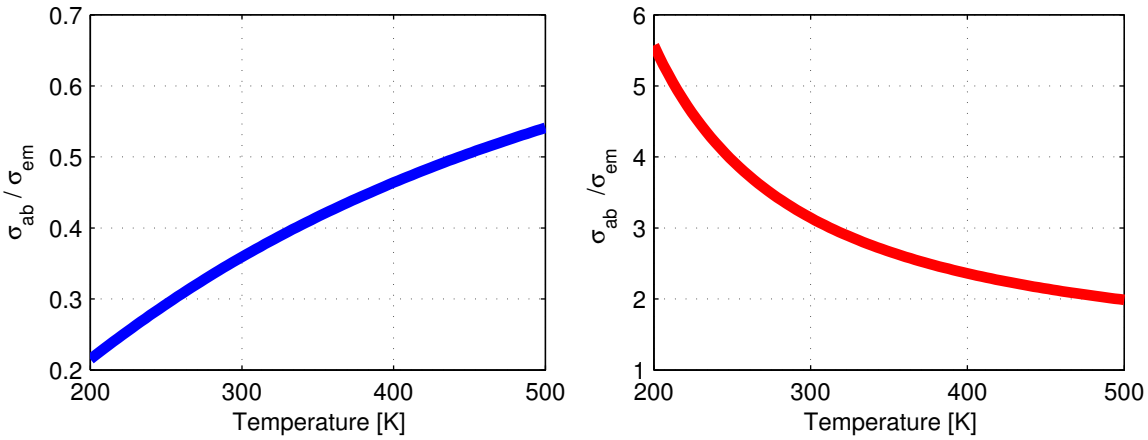

Figure 4.4: Ratio of cross sections of Ho:YLF as given by the reciprocity method at 2064 nm (left) and at 1888 nm (right) as a function of temperature.

The importance of the ratio between the absorption and emission cross sections can be illustrated by calculating the limit on the population (transparency) of the ${}^5I_7$ manifold at a particular wavelength, see Equation 2.16. The difference between the population at transparency at different wavelengths, say a pump and laser wavelengths ($\lambda_p$and λ_l) shows the three level nature of the gain medium.

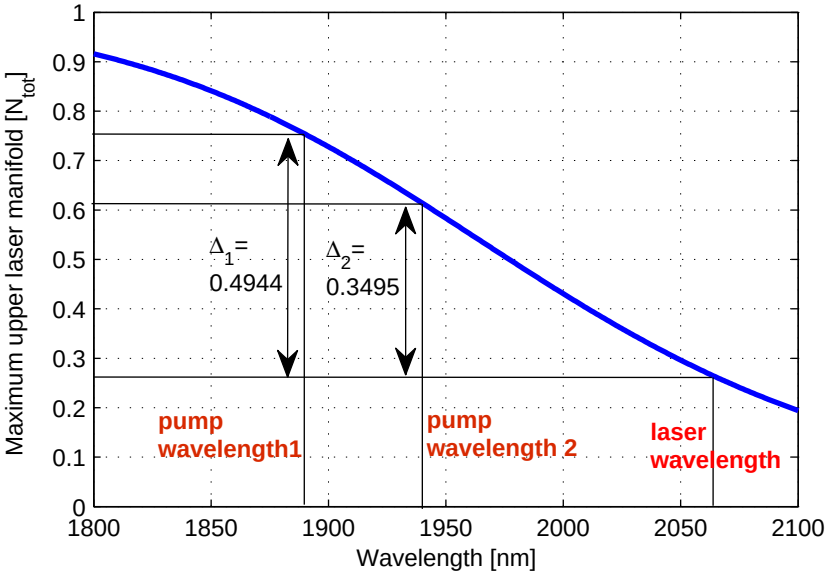

Figure 4.5: Transparency of Ho:YLF at different wavelengths at 300 K.

Figure 4.5 shows that pump beams with shorter wavelengths become transparent with larger populations of ions in the upper laser level than pump beams with longer wavelengths. Similarly if the gain medium is inverted, having a greater population density than the steady state transparency (at a particular wavelength) then a longer wavelength seed laser could potentially extract more energy from the ions as they are depopulated to the transparency population. The transparent population difference between pump and seed laser gives one limit to the amount of energy that can be extracted by a laser pulse. However this analysis does not account for the rate at which the absorption and stimulated emission processes occur, the depopulation of the upper laser level by spontaneous emission, or effect of any of the other processes occurring in the gain medium. Other material properties of the gain medium effect the manifold population such as the lifetime of the manifolds (Table 4.2) .

Manifold	Radiative lifetime [ms] [1]	Fluorescence lifetime [ms]
$^5I_7$ (upper laser level)	13.921	16.1 [9],14.5 [10]
$^5I_6$ (major E.T.U. level)	6.455	2.9 [10]
$^5I_5$(major E.T.U. level)	7.922	$\sim$ 0.020 [10]

Table 4.2: Theoretical radiative and experimental fluorescence lifetimes of Ho:YLF.

The fluorescence lifetime of the upper laser level (and all levels) was expected to be shorter than the radiative lifetime. The discrepancy between the results could result from differences in the measured samples and in experimental setups. The measured fluorescence lifetime of the higher excited manifolds

are significantly smaller than the respective calculated radiative lifetimes[1]. In the calculations that follow a radiative lifetime of 14 ms is assumed. The branching ratio's for these spontaneous radiative decays are tabulated in Table 4.3 .

Branching Ratio: Receiving Manifold	$^5I_8$	$^5I_7$	$^5I_6$
$^5I_7$	1	-	-
$^5I_6$	0.91	0.09	-
$^5I_5$	0.40	0.57	0.03

Table 4.3: Branching ratios of Ho:YLF [1].

4.2.3 Amplifier Pump Laser: Tm:YLF slab laser

A Tm:YLF slab laser was developed at the CSIR National Laser Center as the pump beam for the amplifier system [3]. The pump beam wavelength was measured to be in the range of 1888 – 1890 nm which overlaps with the 1890 nm absorption peak of Ho:YLF on the π polarization. The Tm:YLF slab laser produced a pump beam with a maximum power of 189 W with beam quality factor of $M_x^2 = 443$ in the horizontal plane and $M_y^2 = 3.8$ in the vertical plane. At lower pump power the beam quality factors were not measured.

Tm:YLF pump laser properties	Value	Reference
CW laser power	0-189 W	[3]
M_x^2	443	[3]
M_y^2	3.8	[3]
Operating wavelength λ_p	1888 nm	[3]
Pump Super Gaussian Parameter in x plane	2	approximated
Pump Super Gaussian Parameter in y plane	20	approximated

Table 4.4: Properties of the Tm:YLF pump beam.

The transverse intensity profile of the Tm:YLF slab laser is very different in the horizontal (x) and vertical plane (y). The profile was approximated with a super-Gaussian function in both planes

$$f_{pump}(x, y, z_0) = A_0 exp\left[-2\left(\frac{x}{w_{x,pump}}\right)^{sgp_{x,pump}} - 2\left(\frac{y}{w_{y,pump}}\right)^{sgp_{y,pump}}\right], \tag{4.1}$$

were A_0 is the normalization coefficient. The even super-Gaussian parameters in the x-plane and y-plane are $sgp_{x,pump}$ and $sgp_{y,pump}$ respectively. The $\frac{1}{e^2}$ beam waist in the x plane is $w_{x,pump}$ and in the y plane $w_{y,pump}$. The two beam waist parameters are important because changes to the beam size can be performed without modification of the pump laser with the use of lenses.

4.2.4 Seed Laser: Single-frequency Q-switched Ho:YLF ring oscillator-amplifier

An existing single-frequency Q-switched Ho:YLF oscillator-amplifier system developed at the CSIR National Laser Center was the seed beam for the amplifier [50]. That system produced a maximum output pulses with an energy of 72 mJ and with a full width at half maximum pulse length of $\sim 320\,ns$ at 10 Hz PRF that increased to up to 600 ns at 350 Hz. However, the energy incident on the amplifier was only 54 mJ due to an optical isolator that was required in the experimental system. The measured beam quality factor at full pump power and 50 Hz PRF was a M^2 of 1.05 in both planes. The wavelength of the oscillator was measured to be 2064 nm. The ring cavity, a diode seed laser and cavity length control ensured that the laser operated unidirectional on one longitudinal mode.

Seed beam properties	Value	Reference
Maximum energy per pulse	54 mJ	[50, 3]
M_x^2	< 1.05	[50]
M_y^2	< 1.05	[50]
Operating wavelength λ_s	2064 nm	[50]
Seed Super Gaussian Parameter in x plane	2	approximated
Seed Super Gaussian Parameter in y plane	2	approximated
PRF	single shot-350 Hz	[50]
Pulse length at maximum energy [FWHM]	320 ns	[50]

Table 4.5: Properties of the seed beam produced by the ring laser-oscillator system.

The transverse intensity profile of the seed beam was approximated with a Gaussian function in both plains,

$$f_{seed}(x, y, z_0) = B_0 exp\left[-2\left(\frac{x}{w_{x,seed}}\right)^2 - 2\left(\frac{y}{w_{y,seed}}\right)^2\right], \tag{4.2}$$

were B_0 is the normalization co-efficient, $w_{x,seed}$ and $w_{y,seed}$ are the $\frac{1}{e^2}$ beam waists in the x and y planes respectively. Similarly to the case of the pump beam, the two beam waist parameters of the seed lasers were important because changes to the beam size can be performed with the use of lenses.

The temporal profile was also approximated by a Gaussian function

$$g_{seed}(t) = \frac{2\sqrt{\ln 2}}{\pi^{\frac{1}{2}} w_{FWHM}} exp\left[-\left(\frac{2\sqrt{\ln 2}\,(t - t_0)}{w_{FWHM}}\right)^2\right],$$

were t_0 is the peak of the pulse and w_{FWHM} is the full width at half the maximum of the pulse.

4.3 Error analysis and model fidelity

Error analysis of the three dimensional time resolved model was difficult because the non-linear nature of the evolution of the population densities. This in turn effects the propagation of beams in the model as the beams are coupled to the population densities. Further complicating the error analysis were the large number of parameters that describe the system, each with different errors. The approach taken was to first evaluate the model for a fixed parameter set. The convergence of the model was discussed with the use of this example.

4.3.1 Convergence of the numerical amplifier model

Numerical errors were found to be closely linked to the choice of the method and the step size and therefore the number of nodes in the model. By changing the step size and measuring the difference between solutions it was possible to see if the solutions converge or diverge. A macroscopic approach to measuring the difference between solutions was made by comparing the average energy per pulse.

The solution was considered to be converging when changing the accuracy of the numerical method (normally achieved by increasing the number of data points of the grid) does not influence the solution. Specifically convergence of the energy per pulse indicates that the changing accuracy of the numerical method does not influence the solution.

In the following section the convergence of the model was investigated by increasing the number of nodes in the solution in a particular dimension. The convergence of the solution was investigated first in the dimension of the direction of propagation of the pump and seed beams, $\hat{z}$, then in the two dimensions of the transverse plain, $\hat{x}$ and $\hat{y}$. The convergence of temporal dimension of the problem was also investigated. These results are for the non-diffracting beam propagation method only.

Convergence in the spatial domain

Convergence in the energy per pulse output of the amplifier was investigated for changes in the number of elements in the $\hat{z}$ dimension of the model. The number of elements in both transverse dimensions was constant, fixed at 20 in both the $\hat{x}$ and $\hat{y}$ dimensions and fixed time steps. The parameters for the numerical model were chosen to be close to the typical parameters for the experimental amplifier, as discussed in section 4.2.

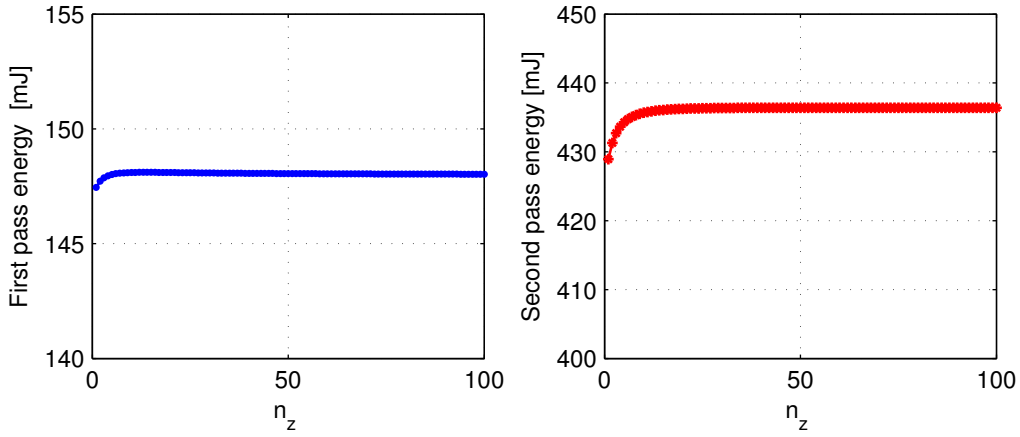

Figure 4.6: Energy per pulse of the amplifier system for different number of nodes in the z direction. The graph on the left shows the energy per pulse of the first pass through the amplifier for different number of elements in the numerical model while the graph of the right shows the energy per pulse of the second pass through the amplifier for different number of elements in the numerical model.

Figure 4.6 shows that as the number of elements was increased, the energy per pulse of the first pass converged to 148 mJ. The energy per pulse of the second pass converged to 0.436 J. The difference in the output energy simulated with 5 elements and 100 was found to be 5 mJ.

The convergence of the energy per pulse was measured by the relative difference between the solutions. In this way the total energy per pulse of the $(n_z + 1)^{th}$ solution was compared to the energy of the n_z^{th} solution. The formulation of the relative error between successive solutions used was,

$$\text{Rel Error} = \frac{E(n_z + 1) - E(n_z)}{E(n_z + 1)}, \tag{4.3}$$

were $E(n_z)$ was the total energy per pulse of the solution with n_z elements. For the same data set as Figure 4.6 the convergence data is shown in Figure 4.7.

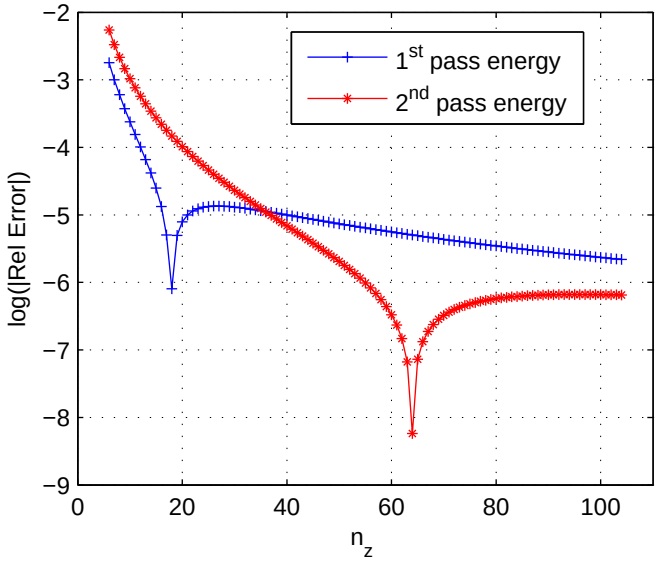

Figure 4.7: Convergence of the energy per pulse of the amplifier model solutions as the number of nodes in the longitudinal dimension was increased. The relative difference between solution is on a log scale.

The result of the convergence measure was that the solutions do converge. The presence of the inflection points in the solutions, seen as the dips in the relative error in Figure 4.7, prompted a test with more transverse elements, they were then increased to 40 in both the $\hat{x}$ and $\hat{y}$ dimensions. The sharp changes of direction of the convergence data were due to the a change of the gradient of the energy from positive to negative (equation 4.3). The results for the energy per pulse are shown in Figure 4.8.

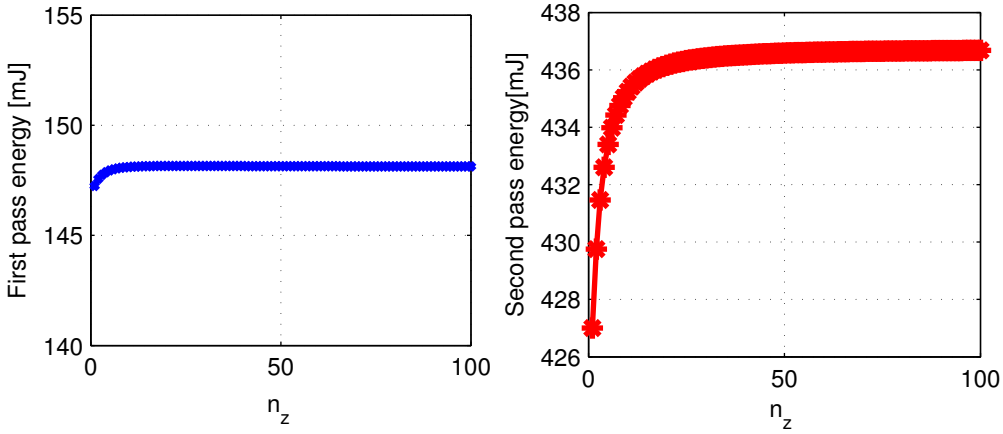

Figure 4.8: Total energy per pulse of the amplifier system for different number of nodes in the z direction for 40 nodes in the x and y dimensions.

A direct comparison between figures 4.8 & 4.6 shows that the differences between the solutions were

small. The convergence is shown in Figure 4.9, which was noticeably different from the convergence behavior shown in Figure 4.7.

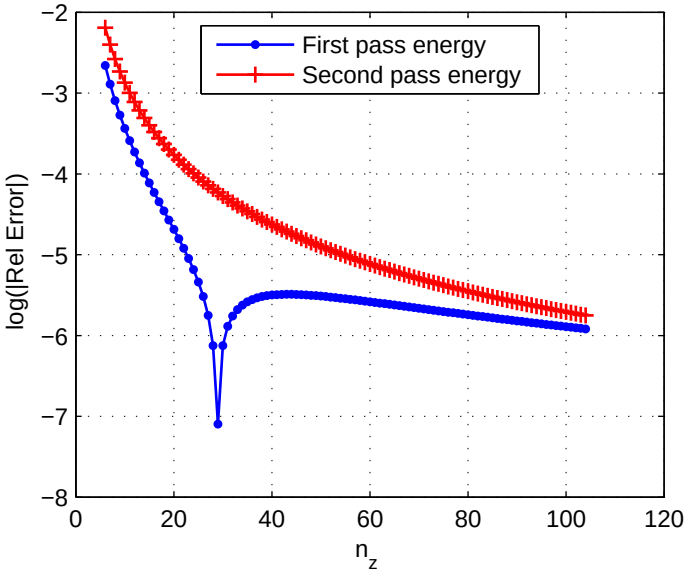

Figure 4.9: Convergence of the amplifier model solutions as the number of nodes in the longitudinal dimension was increased.

The convergence with large numbers of nodes slows, this was expected because the step size in the z direction depends inversely on the number of nodes in the model. While the increase in the number of transverse nodes changed the shape of the convergence behavior it did not changed the value to which the solution converges significantly.

Convergence in the number of elements in the x and y directions

The convergence behavior of the numerical model was tested by increasing the number of nodes in the transverse plane. In effect the increase in nodes in the transverse plane increases the the sampling of the transverse distribution of the pump and seed beams. When the number of nodes was small the representation of the beams may have been poor as the beam profile was under sampled. Similarly if the number of nodes in the transverse plane increased the sampling of the distribution of the population density variables increased. Figure 4.10 shows the energy per pulse of the amplifier system on the first and second pass of the seed as the number of nodes in the transverse plane were increased.

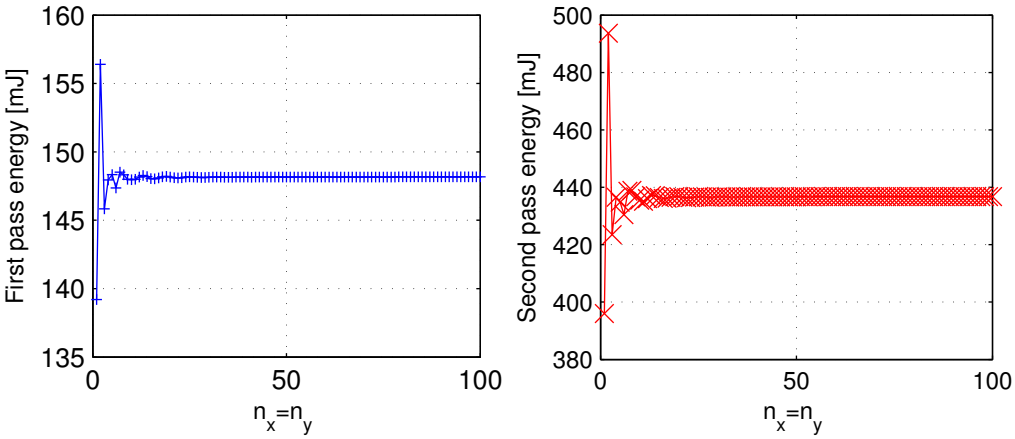

Figure 4.10: Total energy per pulse of the amplifier system for different number of nodes in the x and y direction.

The large variation of the simulated energy per pulse shows that under sampling of the pump and seed beams was a significant problem for this parameter set. The variations decrease rapidly. Figure 4.11 shows the convergence behavior of the amplifier model solutions as the number of nodes in the transverse plane were increased.

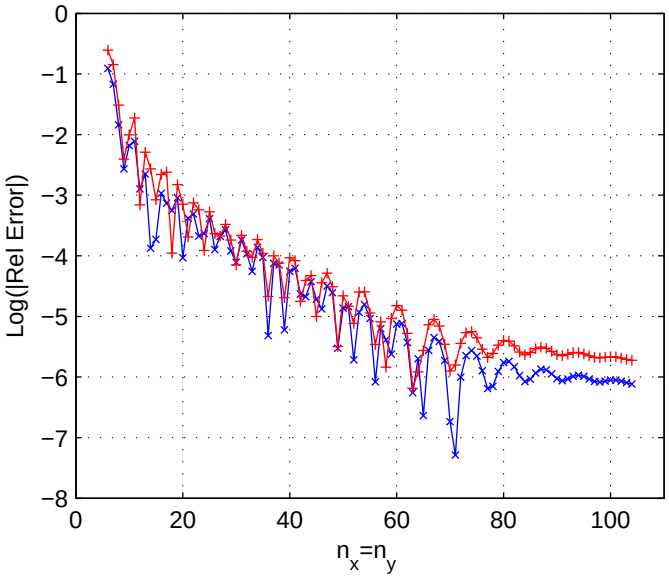

Figure 4.11: Convergence behavior of the model in the transverse plain.

The results of the convergence in the transverse plain were not smooth. The lack of smoothness was explained by the convergence data, interpreted as the scaled magnitude of the gradient of the function of energy per pulse for increasing node numbers (Equation 4.3). The relative error shows that the

oscillation in the traces of Figure 4.10 was damped but persistent until large numbers of transverse nodes were used. The relative error decreased to about 10^{-5} for 65 or more nodes.

Convergence in the temporal domain

Convergence in the pulse and pump phase were treated separately. The simple forward Euler numerical method was used in each case. The results of the convergence of the model when only the time step in the pulse phase was changed are shown in Figure 4.12.

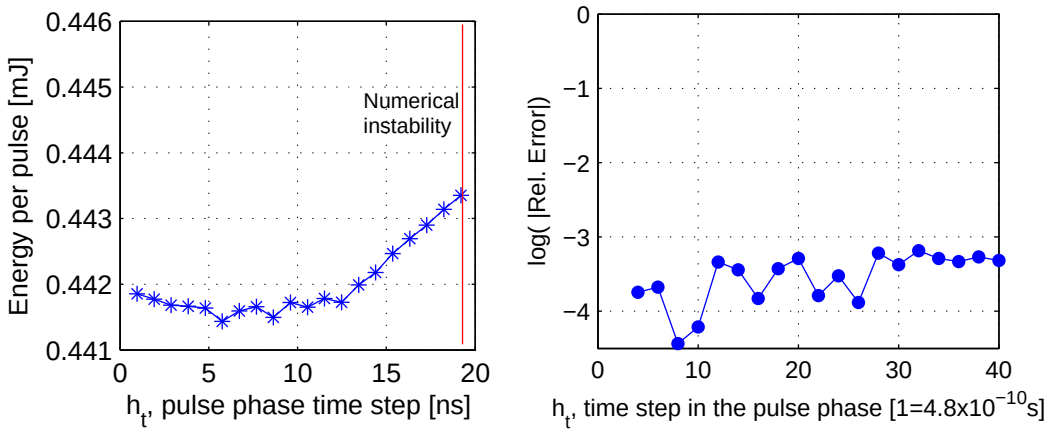

Figure 4.12: Convergence in the pulse phase of the amplifier model.

The results showed that the model was unstable when using large time steps. This was an expected result because with large step sizes the numerical method may overestimate the change in population densities at the peak of the pulse and the model was inherently unstable if the population in any level becomes negative or exceeds the doping concentration of active ions (Equation 2.5). The relative error shows that there was variation in the model even with small step sizes. This was an unexpected result but was explained by the lack of convergence of the energy in the pump phase with the step size used.

The simulation results for the convergence of the solution with different pump time steps are displayed in Figure 4.13.

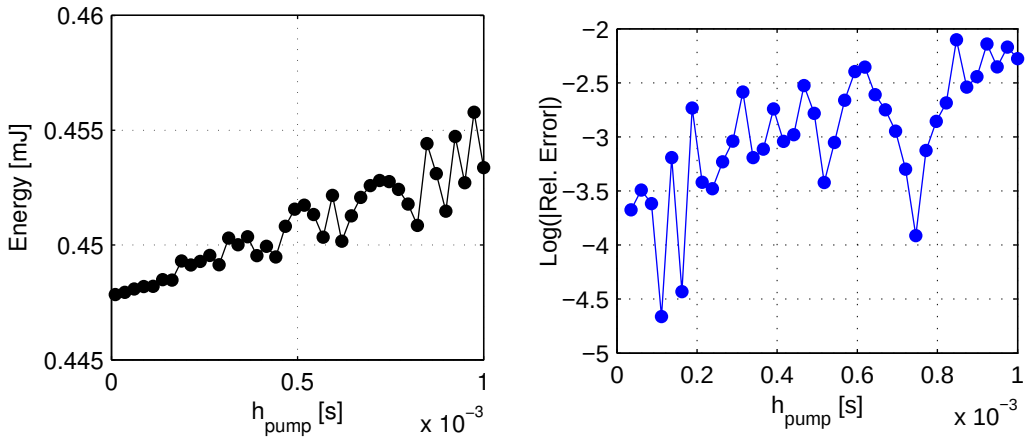

Figure 4.13: Convergence in energy for different time steps in the pump phase of the model.

The convergence in the pump phase showed improvement from the pulse phase results. The slow convergence was likely due to the Euler method in the pump phase that typically has slow convergence for exponential solutions.

Fidelity of the amplifier model

The convergence of the simulation of the amplifier shows that the numerical model finds a stable solution. The convergence also give a good indication of the size of the error that the model introduces to the solution.

4.4 Solutions of the amplifier model

The solutions were a collection of traces or trajectories through time. For a grid with 40 nodes in the x, y and z directions there were 64000 traces for the population densities and a similar number for the intensity of the seed and pump beams.

To depict the evolution of the seed and pump beams it was useful to condense the data for the pump and seed beams to traces of the power passing through particular planes or to depict the static absorption of the traveling wave. For example absorption of the pump beam before and after the 20^{th} pulse is displayed in Figure 4.14. The simulation was in the steady state by the 20^{th} pulse, see Figure 4.15.

The simulation used the parameters found in Tables 4.5, 4.5 & 4.2 and the spectra found in Figure 4.3. The non-diffracting beam propagation method was used to propagate the beams and a simple explicit

Euler method was used to approximate the changes in the population densities.

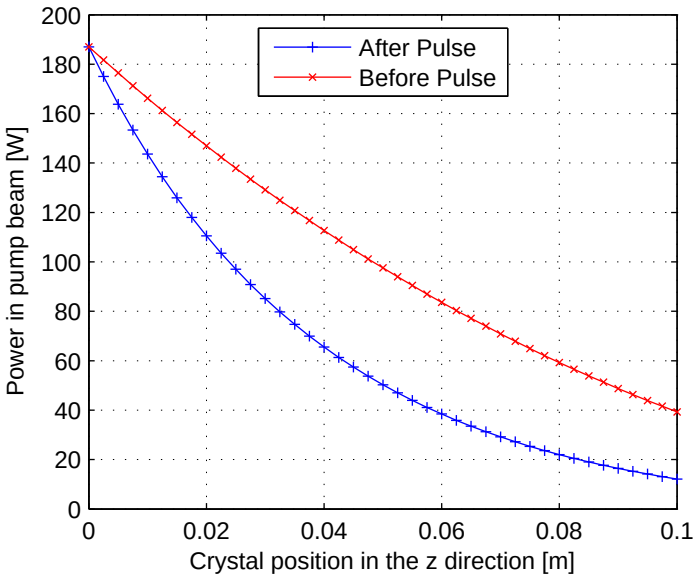

Figure 4.14: Distribution of the pump beam power through the amplifier crystal before and after the 20^{th} seed pulse.

The static absorption of the pump beam through the gain medium after the pulse showed the typical exponential decay expected (equation 3.60), the absorption before the pulse was flatter due to the increased population in the upper laser manifold. The temporal change of transmitted pump power depended on the population of the upper laser manifold as well as the depopulation of the upper laser manifold by the seed beam.

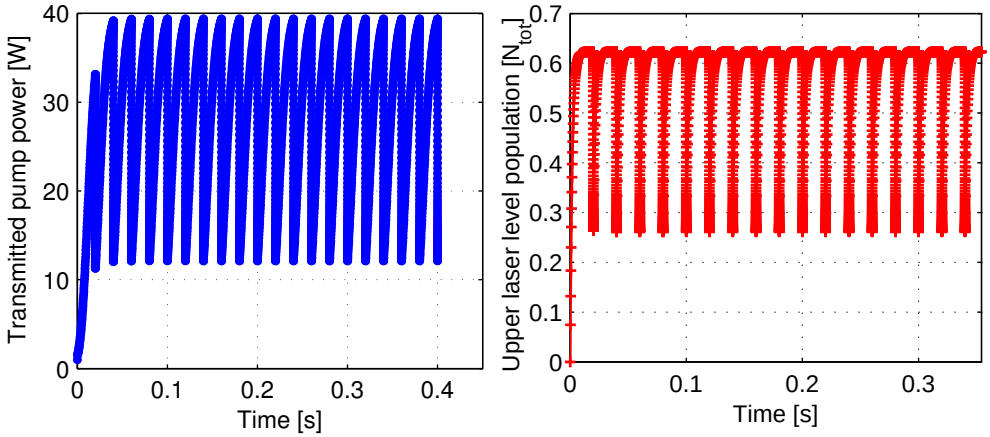

Figure 4.15: Traces of the transmitted pump power (left) and the corresponding change in the population density of a single element $N_2\,(20, 20, 1)$ (right). The element was located in the center of the crystal face that the pump beam was incident on.

Figure 4.15 shows the trace of pump power that was transmitted through the gain medium. The sharp decreases in transmitted pump power was caused by the depopulation of the upper laser level by the pulsed seed beam. This is clearly seen in Figures 4.16 & 4.18 that show the population of the upper laser level before and after the 20^{th} seed pulse.

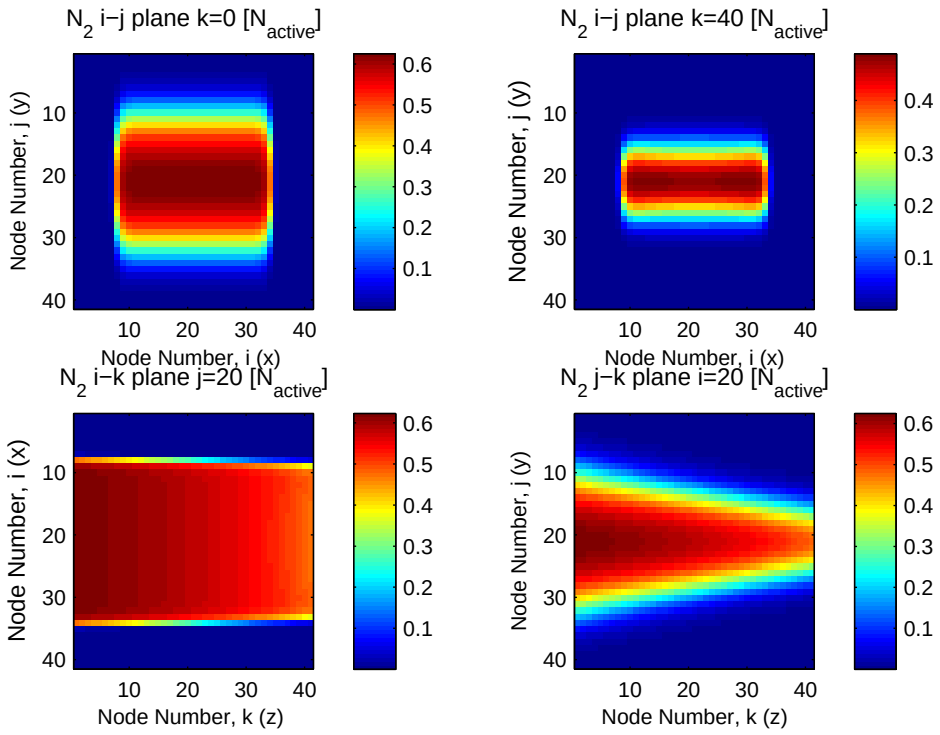

Figure 4.16: Upper laser manifold population before the 20^{th} pulse.

It was seen from the pump beam profile and the gain medium distribution, Figure 4.17 and Figure 4.16 respectively, that the distribution of population density in the upper laser level in the amplifying medium was smooth and followed the profile of the pump beam.

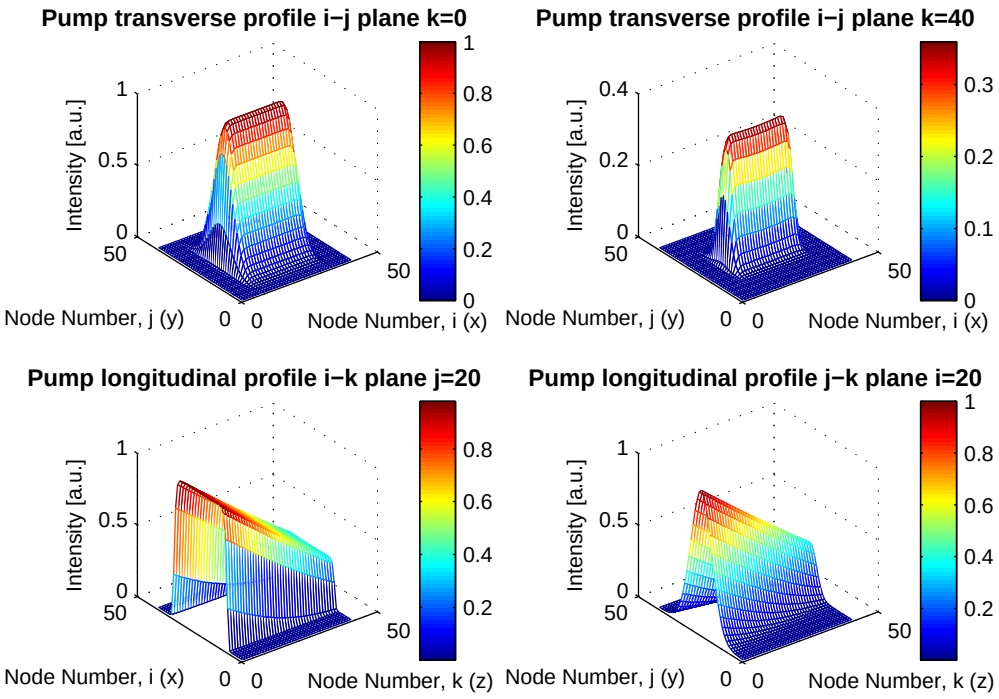

Figure 4.17: Pump beam profiles before the pulse.

Figure 4.17 shows the transverse profile on the end faces and longitudinal profiles of the pump beam that passed through the center of the slab before the 20th pulse. The longitudinal profiles showed flatter (linear) decreases in the center of the beam and exponential decays in the wings of the beam. After the pulse had gone through the amplifier the population density was significantly reduced.

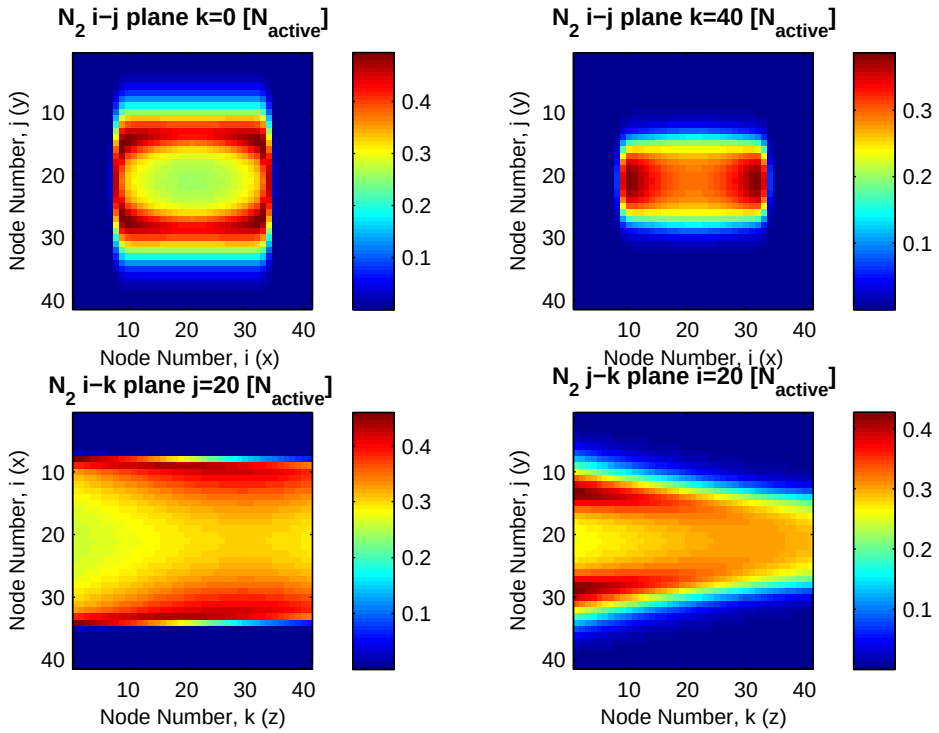

Figure 4.18: Upper laser manifold population after the 20^{th} pulse.

Figure 4.18 shows the upper laser manifold population after the 20^{th} pulse. The population densities at this point in time have been depopulated by the seed pulse. The pulse extracts energy from the population of the manifold more efficiently in the center of its transverse intensity profile than from the wings and left significant population there. This demonstrated the effect on the inversion due to the overlap of the transverse profiles of the pump and seed beams.

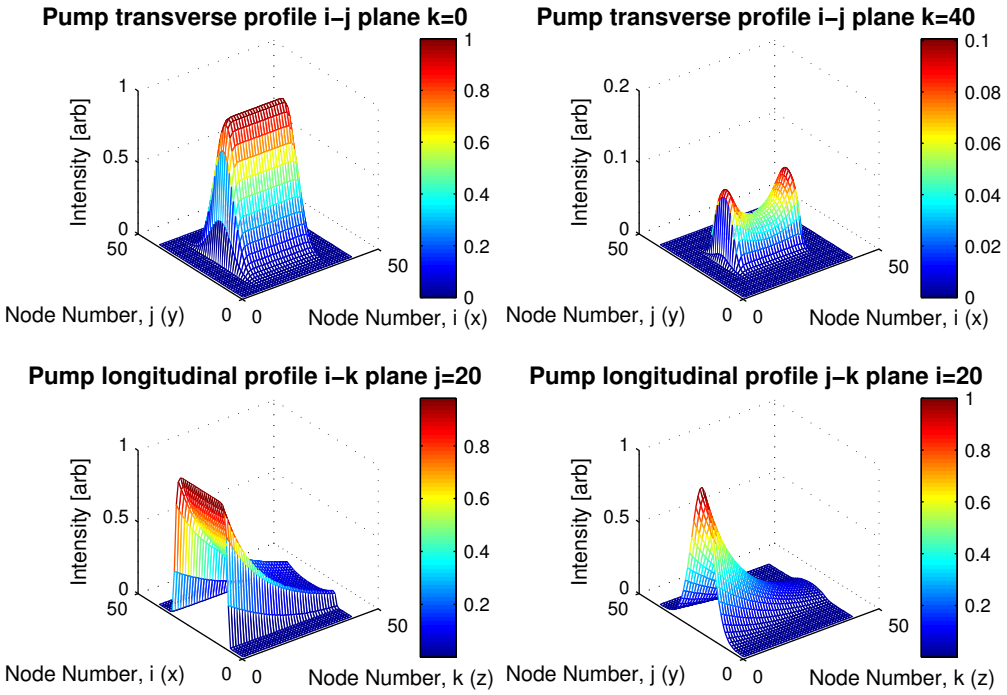

Figure 4.19: Pump beam profiles after the pulse.

The profile of the pump beam was also effected by the change in the population densities, see Figure 4.19. The transverse profile of the pump beam on the exit face (x-y plane k=40) showed significant changes from the profile on the input face (k=0) due to absorption by the non-uniform population densities found after the pulse.

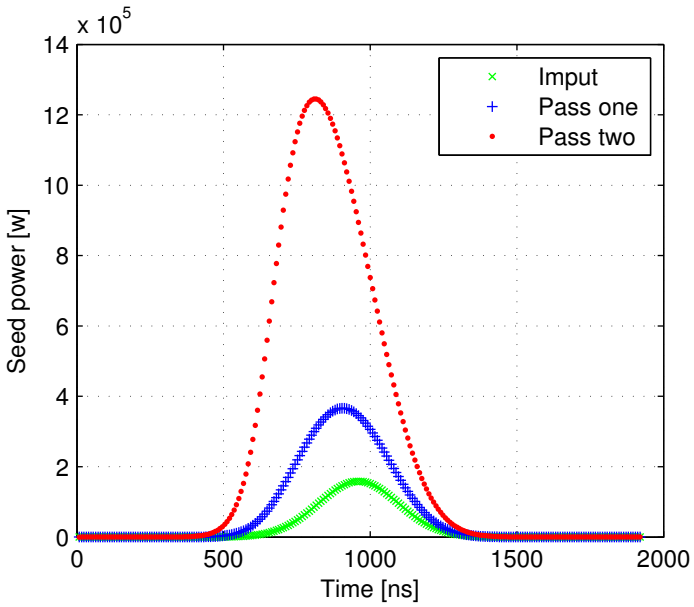

Figure 4.20: Traces of the power of the seed beam as it passed through three different planes that corresponds to the power of the input pulse, the power after the first pass, and finally the power of the second pass of the seed pulse.

Figure 4.20 shows an example of traces of the power of the seed beam and the amplification after the first and second passes through the amplifier. The amplification of the seed pulse by the pumped gain medium lead to both an increase in power and a distortion of the temporal profile. The instantaneous power traces were integrated (numerically) over a specific time interval to yield the energy, for instance the energy that was in a pulse or the energy transmitted by a pump beam.

4.5 General trends of the two-pass amplifier model

The general trends that result from changing an input parameter were useful for understanding the effect of the parameter on the system. The parameters that were studied included: pump wavelength, mode matching and beam size, and crystal length. The other system parameters were held constant and are tabulated in Table 4.6.

Pump Laser Parameters		
Tm:YLF pump laser properties	**Value**	**Reference**
CW laser power	0-189 W	[3]
M_x^2	443	[3]
M_y^2	3.8	[3]
Operating wavelength λ_p	1888 nm	[3]
Pump Super Gaussian Parameter in x plane	2	approximated
Pump Super Gaussian Parameter in y plane	20	approximated
Seed beam properties	**Value**	**Reference**
Maximum energy per pulse	54 mJ	[50, 3]
M_x^2	< 1.05	[50]
M_y^2	< 1.05	[50]
Operating wavelength λ_p	2064 nm	[50]
Seed Super Gaussian Parameter in x plane	2	approximated
Seed Super Gaussian Parameter in y plane	2	approximated
PRF	single shot-350 Hz	[50]
Pulse length at maximum energy [FWHM]	320 ns	[50]
Additional Parameters		
Crystal Length	100 mm	
Upconversion Rate Parameter	$5\times10^{-26}\ \frac{m^3}{s}$	
CW seed power	1 mW	
W_{eff} of the pump	0.948 mm	
W_{eff} of the seed	0.948 mm	

Table 4.6: Simulation parameters for investigation of amplifier performance for different pump beam wavelengths.

4.5.1 Small signal gain and saturation

The behavior of laser amplifiers as the energy of the seed pulse are increased are divided into regimes: small signal and saturation. In the small signal regime the amplifier increases the energy in the pulse linearly. The proportional gain or the double pass small signal gain, G_0 is constant. As the energy in the pulses increases there comes a point were the seed pulse extracts all the energy stored in the amplifier. The amplifier becomes saturated and the gain tends to one with increasing seed energy.

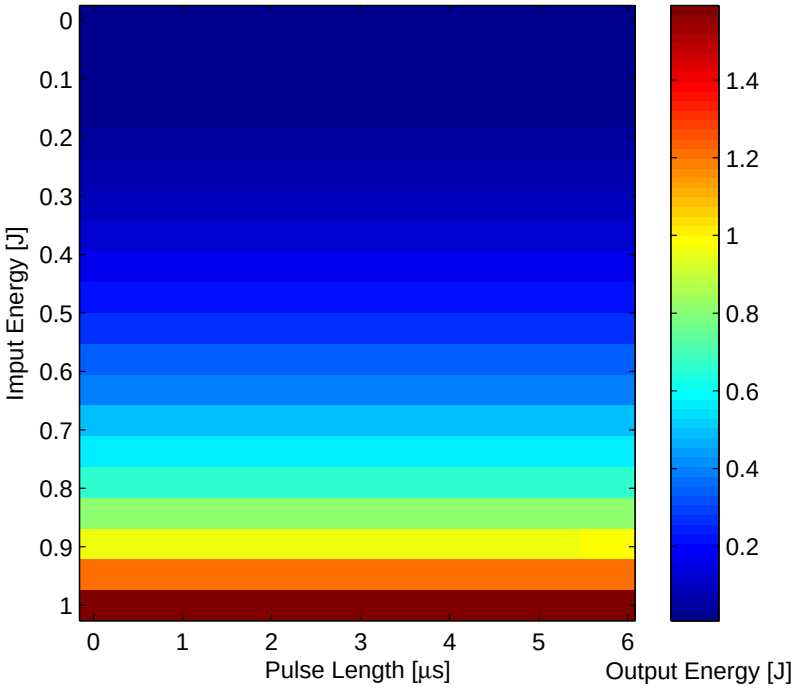

Figure 4.21: Saturation behavior of the amplifier on the sigma polarisation. The figure relates the output energy to the input energy and pulse length.

The energy output of the amplifier, shown in Figure 4.21, showed little dependence on pulse length and had a more pronounced dependence on the input energy. This suggests that the amplifier was saturated by the total energy and not the peak power of the pulse. This was expected as the pulse length was significantly sorter than the lifetime.

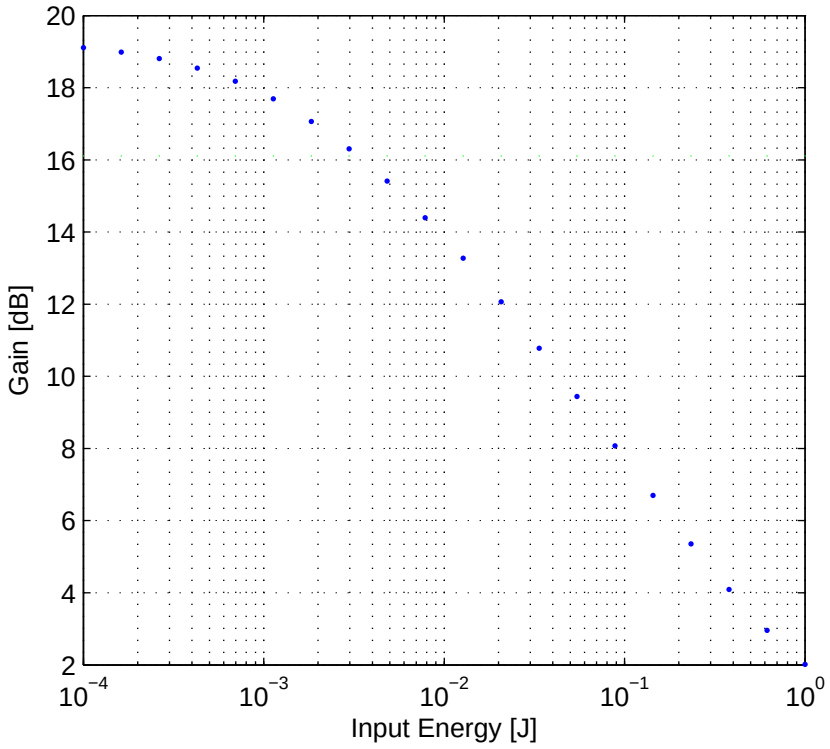

Figure 4.22: Saturation behavior of the amplifier on the sigma polarisation.

In Figure 4.22 the simulation results showed a small signal gain of 19 dB and a 3 dB point of approximately 10 mJ. In the small signal gain regime the energy that was extracted from the amplifier does not decrease with increasing pulse energies as significant depopulation of the laser manifold did not occur. As the seed energy increased the pulse saturated the gain by decreasing the population of the upper laser manifold. The saturation fluence of Ho:YLF at 2064 nm on the sigma polarisation was calculated to be 66 $\frac{kJ}{m^2}$ by Equation 2.21, this meant that the average saturation energy of a beam with effective size of 0.9 mm was 18.8 mJ and by Equation 2.30 the effective saturation energy was 9.4 mJ. The 3 dB point is by definition the effective saturation fluence of the amplifier so the simulated 3 dB point of approximately 10 mJ was very close to the average saturation fluence of 9.4 mJ.

4.5.2 Pump wavelength

Investigation of the effect of the pump beam wavelength on pump absorption and output energy with the numerical model of the amplifier was performed by scanning the pump wavelength parameter across the absorption band of Ho:YLF on the π polarization. The result of the simulation of the amplified

pulse energy and transmitted pump power dependence on pump laser wavelength is presented in Figure 4.23.

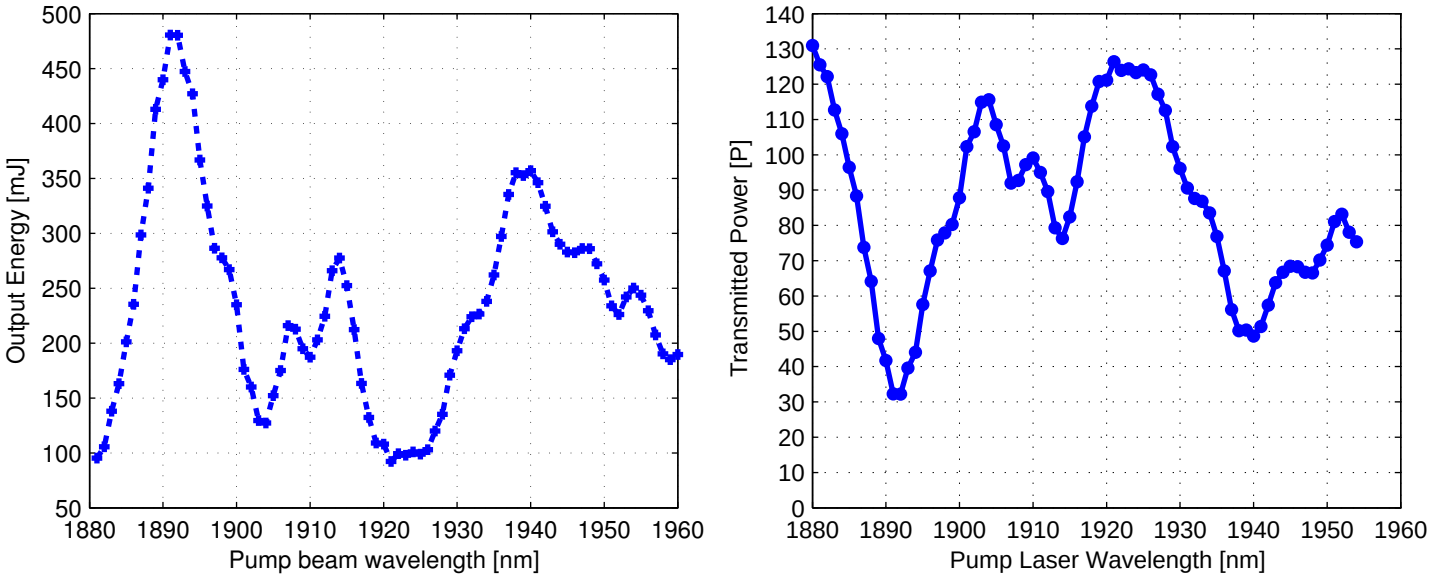

Figure 4.23: Amplifier energy per pulse and average transmitted pump beam power for different pump wavelengths on the π polarization.

The maximum in the output energy of the system occurred close to $1991-1992\,nm$ and corresponds to an amplified energy of $470\,mJ$. There were also peaks in the energy output at $1914\,nm$ and at $1940\,nm$. These peaks correspond closely to the absorption cross section of Ho:YLF as discussed in Section 4.2. However, the data suggests that more energy could have been extracted from a gain medium pumped at 1890-1892 nm than from the same medium pumped at 1940 nm despite the larger absorption cross section at the later wavelength. These results did not include thermal effects, as such the effect of the increased quantum defect at 1890 nm was not evaluated.

4.5.3 Matching pump and seed beam waists

It was expected that the amplifier energy would be dependent on the size of the seed and pump beams of the amplifier. This was investigated and to locate parameters for optimum gain, the simulation was run while the beam waists for the pump and seed beams in both planes where varied. The size of the seed and pump laser beams in the horizontal plane were constrained to be equal. To easily display the data an effective beam size w_{eff},

$$w_{eff} = \sqrt{w_x w_y} \tag{4.4}$$

was used to condense the pump and the seed beams beam waist in both planes to a single dimension. Figure 4.24 shows the dependence of the amplifier performance on the area of the seed and pump beams in the amplifier crystal that was observed.

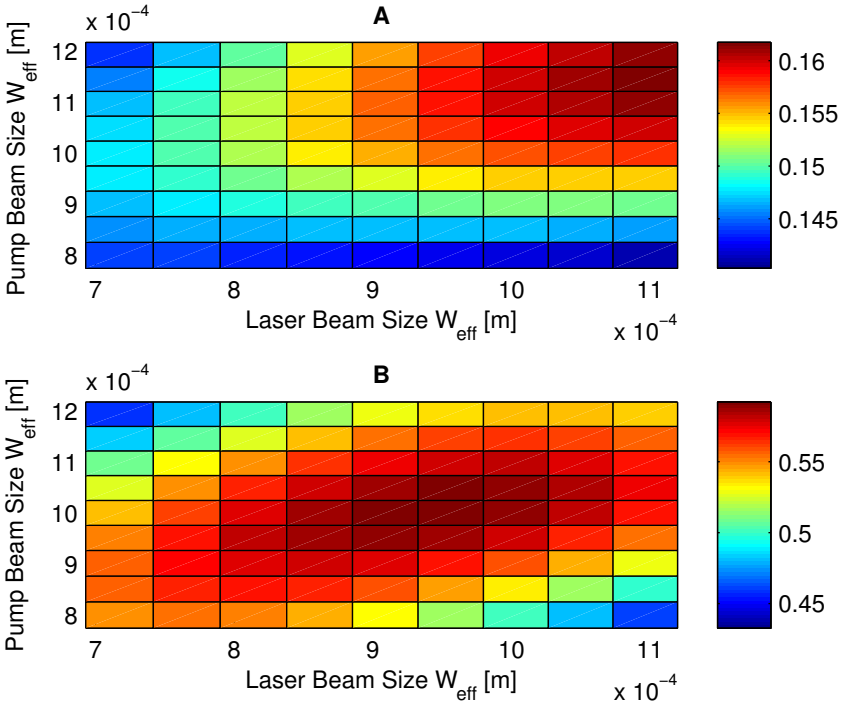

Figure 4.24: The simulated energy per pulse profile [J] for effective pump and seed beam sizes for each pass of the amplifier. The gain for the first pass, graph A, shows larger gain for bigger beams while the gain for the second pass, graph B, has a local maximum.

For the available pump and seed energy the peak energy output occurred approximately at the effective pump beam size of 1 mm and at a seed beam size of 0.95 mm.

4.5.4 Crystal length

The total energy extracted from the amplifier was expected to strongly depend on the length of the amplifier gain medium. Figure 4.25 shows the results that were obtained by the simulation of the amplifiers with different crystal lengths (fixed doping concentration).

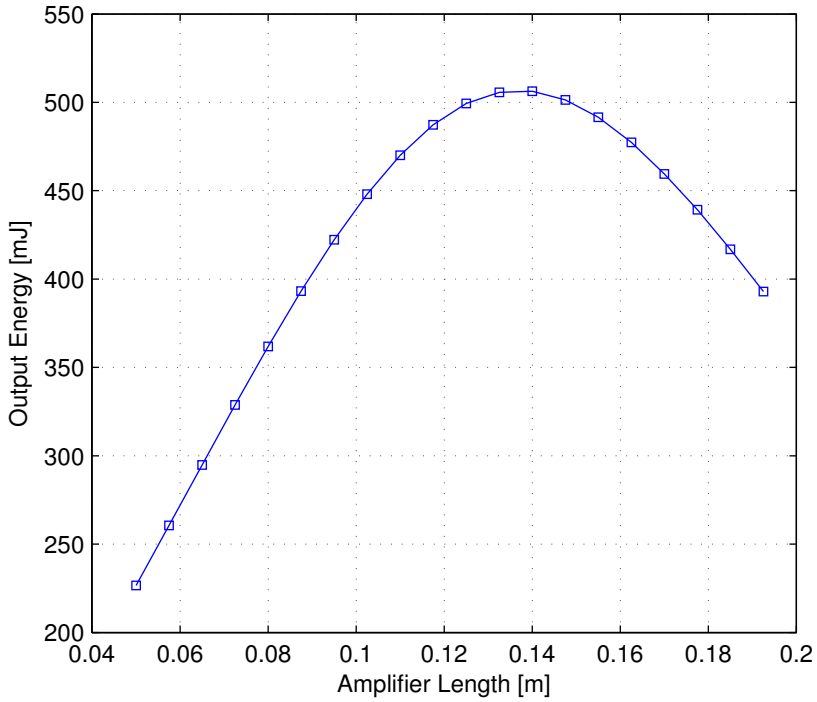

Figure 4.25: Optimization of the amplifier crystal length for a fixed beam size.

The maximum energy of the system was 506 mJ with this particular beam waist occurred with a crystal length of 133 mm. This peak value was unlikely to have been the local maximum given the constraint on the beam size and the fixed parameters, such as the pump wavelength. The result shows the peak in the output energy with increasing crystal length that was expected as it is typical of three level lasers.

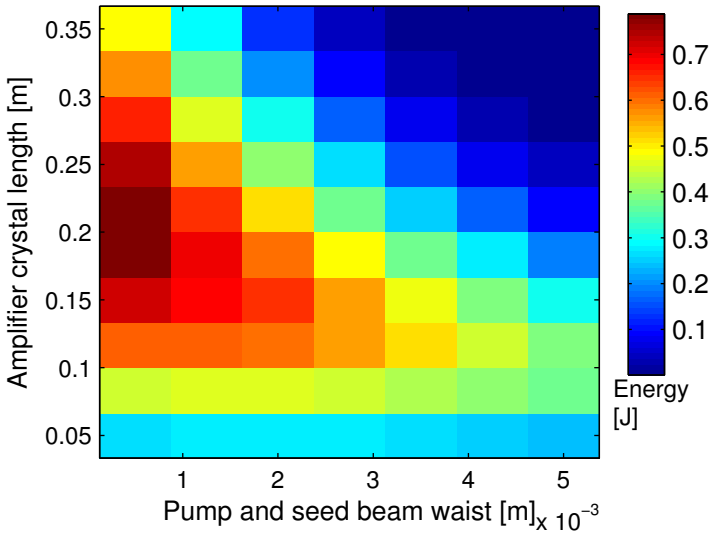

Figure 4.26: Dependence of amplifier energy output on the beam size and the gain medium length.

The simulated amplifier performance was expected to depend on both the "mode" volume and the intensity of the pump and seed beams. This parameter space was significantly larger and therefore matched (equal) pump and seed beams sizes have been assumed to be close to the optimum for any given amplifier length. The results that were obtained from the simulation of changing combined beam size (matched) and crystal length are shown in Figure 4.26. The figure shows that the energy of the amplifier increases for smaller beams and longer crystals.

4.6 Discussion & Conclusions

A general amplifier model was applied to a two pass slab design. The numerical model converged for this set of parameters in both temporal and spatial dimensions. The convergence characteristics of the model show that the model finds stable solutions and also provides an estimate of the error introduced by the numerical approximations made in the model.

The model has been used to simulate the change in performance for different pump and gain medium parameters. The simulation predicts the general trends for when certain parameters are varied. On the basis of the simulation results certain recommendations can be made on the experimental setup.

The model predicts that pump sources with wavelengths near 1890 nm are better for high energy operation of a two pass amplifier system. The simulated energy maximum at 1891 nm was larger than the local maximum near 1940 nm despite the lower absorption, this was because of the three level nature of the pump transition and a lower stimulated emission cross section. These results did not investigate the thermal effects in detail and it should be noted that the increased quantum defect at 1890 nm may deposit more heat into the gain medium.

Optimization of the pump and seed mode sizes suggest that an optimum size for a fixed 100 mm long crystal may be found near an effective beam widths of 1 mm. However, the model shows that longer gain medium lengths could increase the performance significantly with the associated optimum matched beam sizes decreasing with increasing length.

These results were used to optimize the design for an amplifier system, see Chapter 5. Further predictions are discussed in Chapters 6.

Chapter 5

Comparison between experiment and simulation of a high energy amplifier

A high energy Ho:YLF amplifier was developed for the Ho:YLF ring laser described in the previous chapter and constructed at the National Laser Center [3]. The results are reproduced with the principle author's consent and the description of some of the sub-systems expanded through helpful discussion with the authors.

The amplifier design discussed in the previous chapter was simulated but differed from the preliminary simulation in a number of features. These assumptions, parametrization and simplifications are discussed in Section 5.1.

The comparison between the results from the numerical model and the results from the experimental system is presented in Section 5.2. The results of three experiments that were completed on the amplifier system are compared to the simulation results. The effect of different propagation methods used in the model are presented.

The next section presents modeling results of the temperature dependence of the amplifier. This effect was extrapolated from theoretical effect of temperature on the cross sections of ionic Holmium (doped in YLF). The final section discusses the presented results.

5.1 System parametrization

The experimental amplifier setup differed from the design; some of the differences were changes to parameters, such as the differences in pump power or the energy output of the ring laser system. Other differences were more complicated, for instance the model assumed a good beam quality for the pump laser, that was not the case in the experimental setup.

The system parameters are found in Table 5.1. This table presents parameters that were both the known or measured values as well as inferred, approximated or extrapolated values. The motivation for such assumptions are discussed below.

Tm:YLF pump laser properties	Value	Reference
CW laser power	0-189 W	[3]
M_x^2	443	[3]
M_y^2	3.8	[3]
Operating wavelength λ_p	1890 nm	[3]
Pump Super Gaussian Parameter in x plane	2	approximated
Pump Super Gaussian Parameter in y plane	20	approximated
Seed beam properties		
Maximum energy per pulse	54 mJ	[50, 3]
M_x^2	< 1.05	[50]
M_y^2	< 1.05	[50]
Operating wavelength λ_s	2064 nm	[50]
Seed Super Gaussian Parameter in x plane	2	approximated
Seed Super Gaussian Parameter in y plane	2	approximated
PRF	single shot-350 Hz	[50]
Pulse length at maximum energy [FWHM]	320 ns	[50]
Polarization in Ho:YLF crystal	σ	
CW seed component	50 mW	
Additional Parameters		
Crystal Length	$100\,mm$	Measured
Upconversion Rate Parameter	$5 \times 10^{-26}\ \frac{m^3}{s}$	*Approximated

Table 5.1: Model parameters approximating the experimental setup of the high energy two pass amplifier. *Discussion of the upconversion rate parameter can be found in this Section.

Continuous low power seed component

The ring laser was injection seeded with a continuous wave diode laser that was tunable around 2064 nm which led to a non-negligible continuous wave component in the seed beam that was amplified and

led to a reduction in stored energy of the amplifier. Figure 5.1 shows the simulated reduction in energy per pulse due to the continuous wave power in the seed beam.

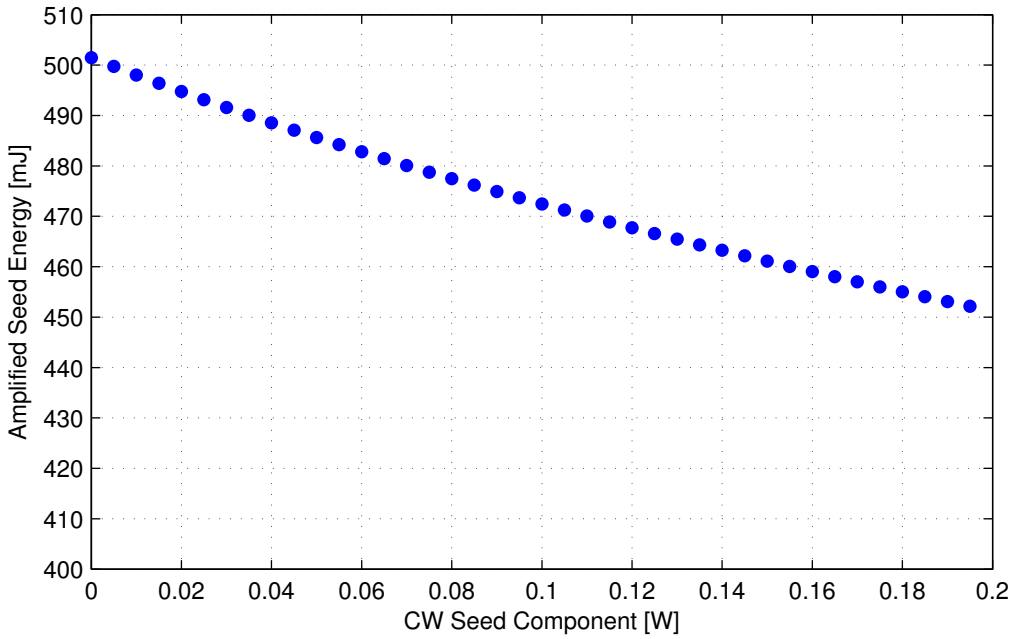

Figure 5.1: Effect of continuous wave seed component on the energy of the amplified pulse.

The effect of the CW seed of up to 200 mW was to reduce the output energy by up to 49 mJ as can be seen in Figure 5.1. The measured continuous wave component of the power was approximately 50 mW which corresponded to around 15mJ of energy reduction.

The effect of the continuous wave component was assumed to override the effect of ASE in the amplifier as the amplifier was seeded continuously with significant power.

Upconversion Coefficient

The effect of energy transfer upconversion has been modelled and shown to reduce the efficiency of laser systems [33]. The upconversion coefficient between the ${}^5I_7$ and ${}^5I_7$ manifold in Ho:YLF is generally regarded to be lower than in either Ho:YAG and Ho:LuAG at a given doping percentage [11]. At the low doping concentration of the available Ho:YLF crystals the upconversion rate is not well known. Shaw *et al.* measured a value of approximately $2.5 \times 10^{-24} \frac{m^3}{s}$ in Ho:YAG with a 1% atomic doping percentage [35], while Barnes *et al.* respectively measured $2.8 \times 10^{-24} \frac{m^3}{s}$ and $7.2 \times 10^{-24} \frac{m^3}{s}$ in 1% and 2% doped Ho:YAG and $3.2 \times 10^{-24} \frac{m^3}{s}$ in 2% Ho:YLF [11]. The upconversion rate of gain materials

with 0.5% doping was likely to be much smaller as the upconversion rate as been shown to have a quadratic dependence on the doping concentration of Ho ions in fluoride crystals [35, 11]. The effect of the upconversion rate on the performance of the amplifier was modeled and is shown in Figure 5.2.

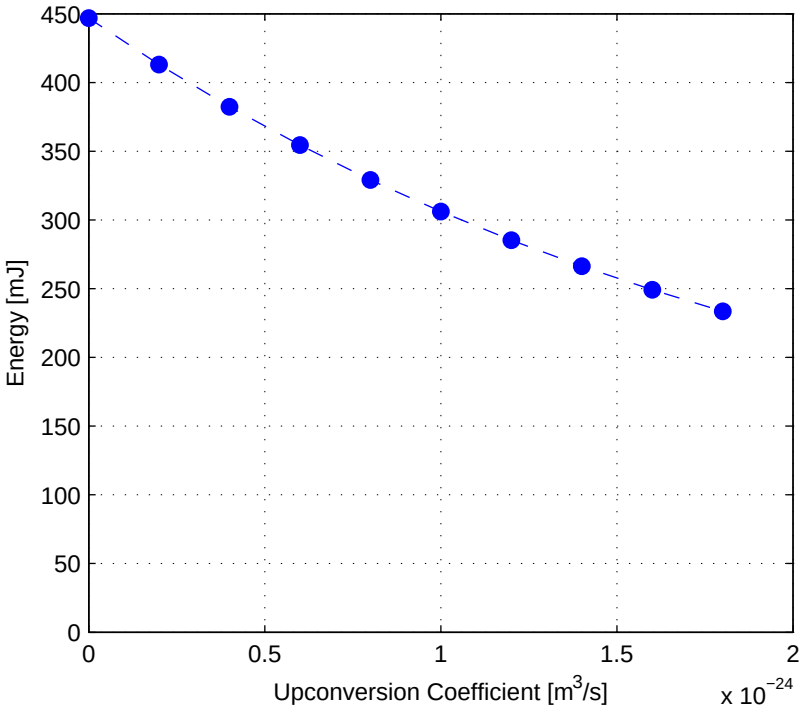

Figure 5.2: The effect of upconversion on amplifier performance.

The reduction in output energy as the upconversion rate is increase was found to be very steep. Unfortunately the upconversion coefficient for Ho:YLF with doping levels less than 2% was not known. This situation was further complicated as the pump wavelength at 1890 nm lead to higher inversions at low repetition rates (see Figure 4.5) than other systems, pumped at 1940 nm, where upconversion has been deduced as not being significant [53].

Modelling the pump beam

The diffraction of the pump beam in the amplifier was not properly modeled due to the increase in complexity in the propagation of the pump beam and the related computational requirements. The numerical propagation method outlined in Chapter 3 was unsuitable for the description of a highly divergent and multimode beam. Two different numerical methods were attempted to model the beam: decomposition into a finite number of Hermite-Gauss modes [23] and analytical method based on

the properties of super-Gaussian beams [17]. The numerical evaluation of the Hermite polynomial was limited by size of the vector (or matrix). In this case limitation was the computer RAM, the highest order beam that could be evaluated was, n = 50, which was insufficient to describe the beam. The analytical method was found to unstable when implement numerically. Unfortunately this left the existing descriptions of the pump beam that were assumed in the model. As consequence the measured pump beam and that described in the model were significantly different, the measured beam radius entered the crystal at 5 mm, focused down to 3.3 mm and then diverged again to approximately 5 mm at the exit face in contrast to the simulated pump beam that did not diverge at all in the case of the non diffracting propagation method or the limited diffraction of same Super-Gaussian beam with the diffracting beam propagation method. The beam propagation factor in the horizontal(verical) plane, M_x^2 $\left(M_y^2\right)$, was 440(5) [3].

5.2 Comparison with experimental results

The amplifier was experimentally characterized by changing the pump power, the seed pulse repetition frequency and the seed energy. In the first of three experiments the power of the Tm:YLF pump laser was varied. The parameters for the simulation used the same beam waist for all different pump powers which was a simplification because the Tm laser produced smaller beams at lower powers. The result is reported in Figure 5.3.

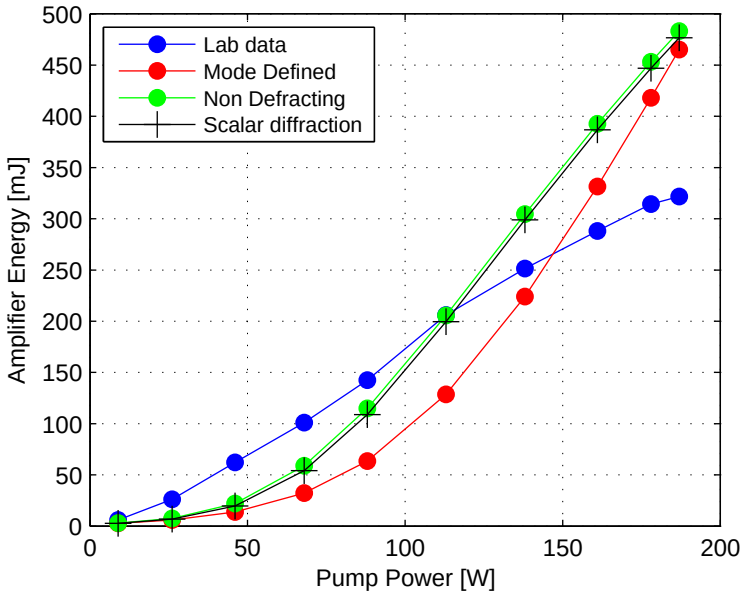

Figure 5.3: The amplifier energy output versus the pump power. The results from experimental amplifier [3] and the simulation with three propagation methods are shown.

There was a significant difference (150 mJ!) between the predicted performance and the experimental result. This difference is likely due to the description of the horizontal radius of the pump beam in the crystal: the radius depended on the pump power, the pump beam waist parameter was chosen to be the value of the pump beam at the focus, of approximately 3300 μm . A comparison of the effect of the pump beam sizes on each of the three experiments is addressed in Subsection 5.2.1 after a comparison of the three experiments with the fixed pump parameter.

The effect of the change of the pump beam waist in the x-plane at lower powers the amplifier was simulated at 100 W of pump power and varying beam waists. The result can be seen in Figure 5.4.

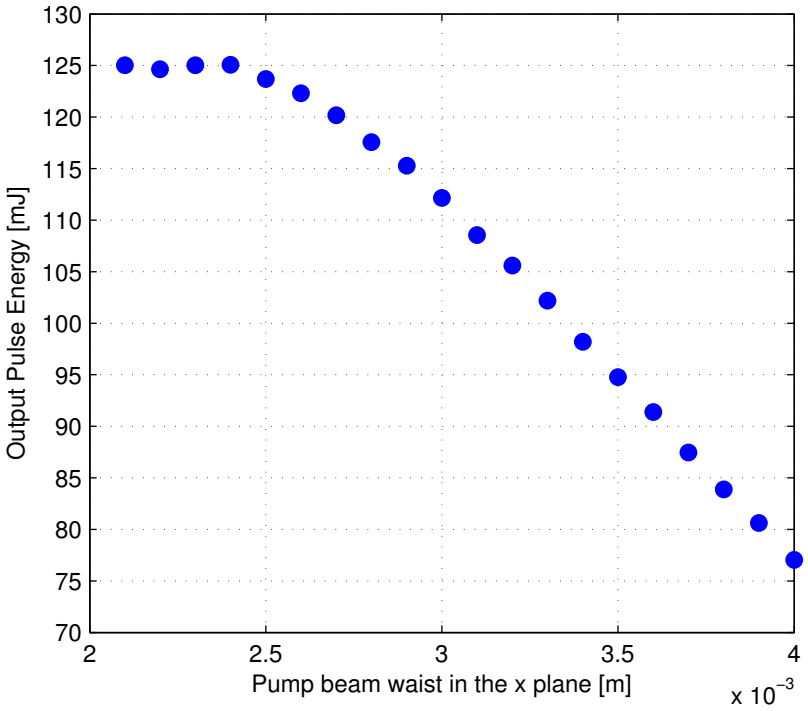

Figure 5.4: The effect of decreasing the pump beam waist on the amplifier at pump powers of 100W.

The results show the expected decrease in energy as the pump waist increased. The linear decrease was explained by the decrease in pump intensity. The roll off at small waist sizes was caused likely due to the saturation of the pump beam and mismatch between the pump and seed beam sizes.

The second experiment was to measure the amplifier performance as the pulse repetition rate of the seed laser was varied. The energy per pulse of the seed laser decreased as it's PRF was increased as shown in Figure 5.5 .

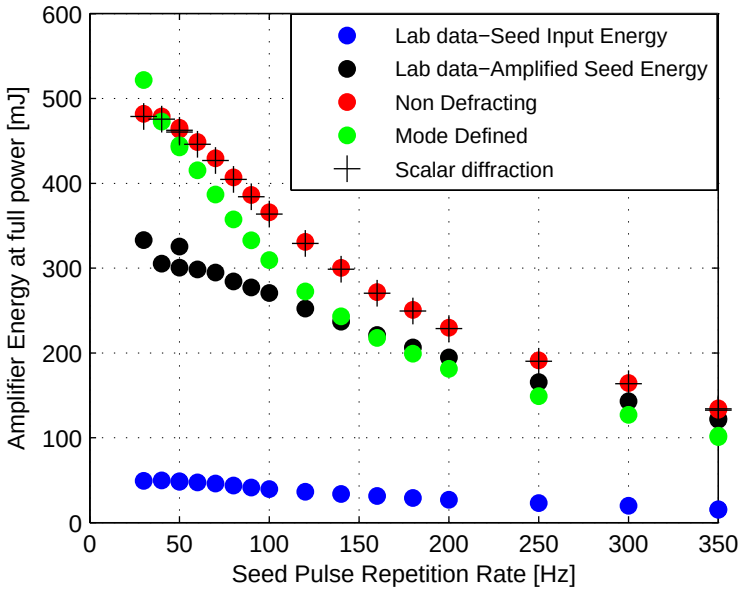

Figure 5.5: Comparison between the simulated and the experimental [3] amplifier's energy output for seed energies and pulse repetition rates at full pump power.

Figure 5.5 shows results where a consistent difference in the predicted and the experimental amplified energy was seen, with the simulation showing higher energy per pulse than the experimental amplifier. The difference in energy per pulse was attributed to the mismatch in the pump beam, the pump spot size dependence investigated further on in this section. The difference was most pronounced at low PRF while at high PRF the energy outputs were similar. The amplifier was designed to operate at 50 Hz as the energy of the seed laser did not increase significantly at lower PRF [50].

The third experimental characterization of the amplifier system was to vary the seed energy at 50Hz PRF at full pump power.

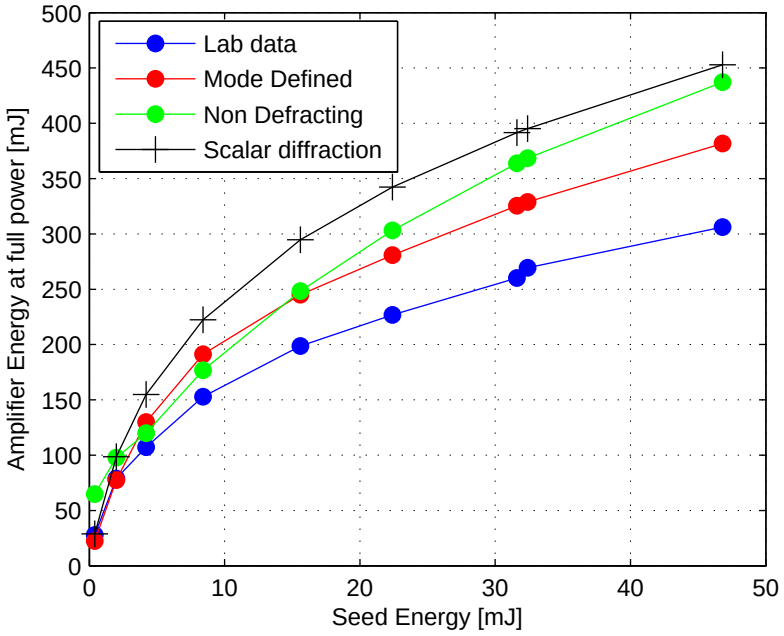

Figure 5.6: Comparison between the simulation and the experimental [3] amplifier's energy output for different seed energy at full pump power.

Figure 5.6 shows the results of a comparison between the simulation and the experimental performance for different seed energies. The model showed a similar trend to the experimental results, as the seed energy increased the amplifier gain decreases as the pulse saturated the gain medium. The simulation results have significantly larger energies. The persistent over prediction of the amplifier energy per pulse by the simulation was present which was presumed to be caused by a combination of the pump beam size miss-match, a larger upconversion parameter than was assumed and the effect of the CW seed.

5.2.1 Pump beam matching

The description of the pump beam as a collimated beam with the smallest measured waist was motivated by the restrictions from the model. Within the restrictions of the model to well behaved lower order beams or even non-diffracting beams the diffraction of the very poor quality pump beam could not be modelled. The only effective means to study the effect of the differing pump beam intensity within the model was to vary the pump beam radius. In effect the diffraction of the experimental pump beam has been approximated by assuming different average beam sizes .

The effect of large beam radii on the performance of the amplifier was simulated with the same transverse description of the pump beam. Only non-diffracting propagation method was used. The simulation used the same data set as the previous simulations but with 4 different pump beam sizes in the horizontal plane: 2, 3, 4, and 5 mm.

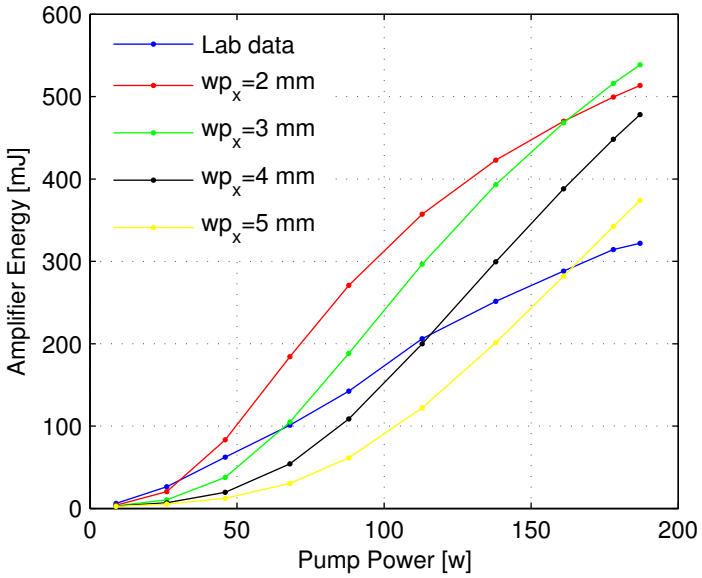

Figure 5.7: Simulation results showing the "slope" of the amplifier. The simulation of different pump beam waist sizes in the horizontal plane showed how the changing size of and uncertainty in this parameter has a large effect on the correlation with the experimental amplifier results [3].

The result of the simulation of the amplifier slope, found in Figure 5.7, showed a the intersecting of all the simulation results, the experimental result crosses the simulated result for smallest to largest pump beam sizes as the pump power increased. The best match at full power was the largest beam considered.

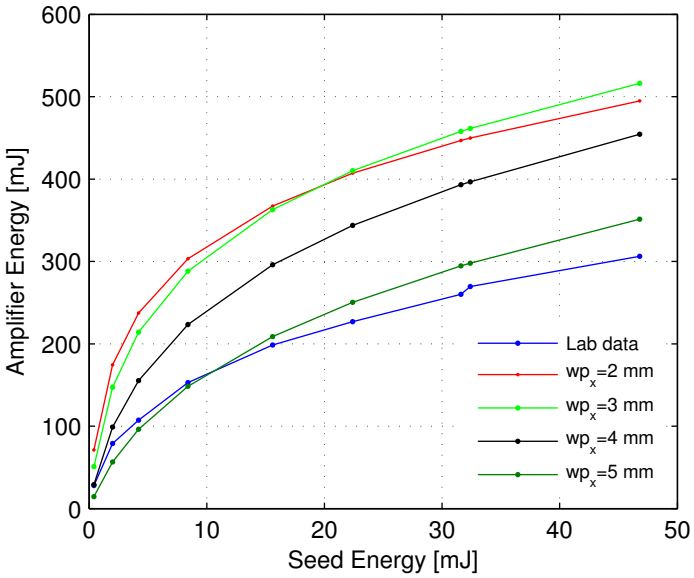

Figure 5.8: Comparison between the simulation and the experimental amplifier's energy output for changes to the seed energy at full power. This result was performed under constant pump power and showed better agreement between the large pump spot sizes and the experimental data [3].

Similarly the best match between the simulations with different beam sizes and the experimental results, with the change of seed energy at full power was the 5mm beam, as seen in Figure 5.8.

The characterization of the amplifier by changing the PRF of the seed laser was the only measurement where there was a significant change to the amount of time, and hence pump energy, before each pulse.

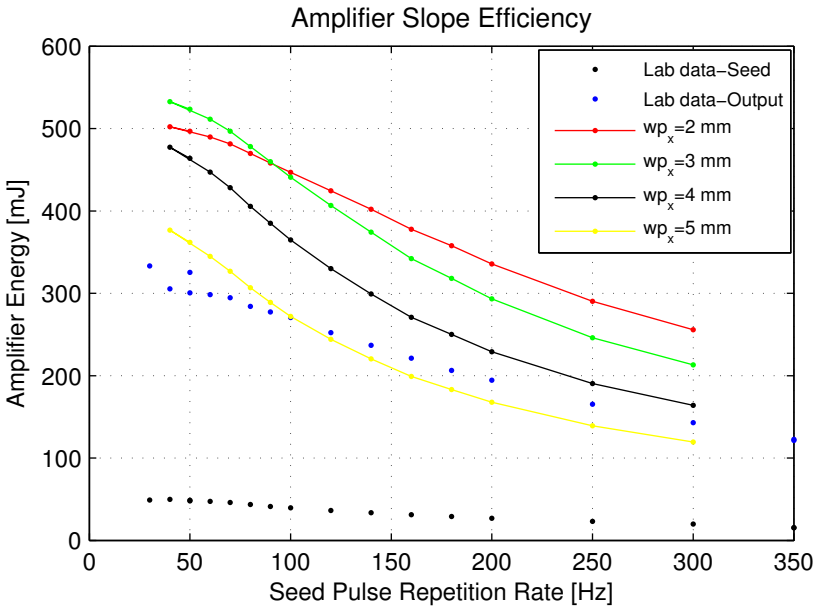

Figure 5.9: Comparison between the simulation with different pump beam parameters and the experimental amplifier's energy output for different seed energies at full power [3].

The results, shown in Figure 5.9, indicate that the matching the simulated results with the largest pump beam to the experimental data was valid only for the lower repetition rates and then failed to match at higher repetition rates. This indicated that the miss match was likely to be caused by a combination of the pump beam representation and other factors.

5.3 Temperature dependence of the cross sections of the laser transition

The temperature dependence of absorption and emission cross sections of bulk Ho:YLF above room temperature has not been measured (to the author's knowledge). It was possible that the temperature in the gain medium effected the efficiency of the amplifier. This section explores this effect by the use of assumptions about and extrapolation of the cross section.

There were a number of possible models that the change in the cross sections with increasing temperature could have followed but the lack of data at high temperatures complicates extrapolation [30]. Due to the lack of available high temperature cross section data the simplest possible assumption was that either the emission cross section was constant at the value of the room temperature data, over the considered temperature range , ie. $\sigma_{em}(\lambda, T = 300K)$, or that the absorption cross section was constant over the same range, at $\sigma_{ab}(\lambda, T = 300K)$. The emission cross sections under the first assumption, $\tilde{\sigma}_{em}$ had the value,

$$\tilde{\sigma}_{em} = \sigma_{ab}(\lambda, T = 300K)\, e^{\frac{hc}{k_B T}\left(\frac{1}{\lambda} - \frac{1}{\lambda_u}\right)} \tag{5.1}$$

$$\tilde{\sigma}_{ab} = \sigma_{ab}, \tag{5.2}$$

while under the second assumption the absorption cross section , $\tilde{\sigma}_{ab}$ had the value,

$$\tilde{\sigma}_{em} = \sigma_{em} \tag{5.3}$$

$$\tilde{\sigma}_{ab} = \sigma_{em}(\lambda, T = 300K)\, e^{-\frac{hc}{k_B T}\left(\frac{1}{\lambda} - \frac{1}{\lambda_u}\right)}. \tag{5.4}$$

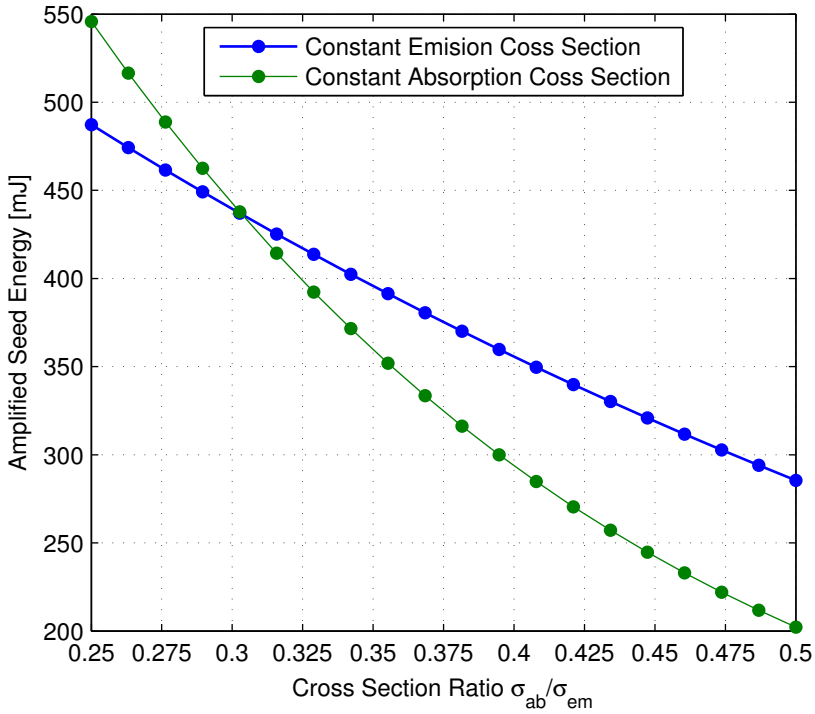

Figure 5.10: Reduction in amplifier performance due to the change in the ratio of cross sections.

Figure 5.10 shows the simulated results as changes to the ratios of cross sections effected the energy output. Both simulations showed decreasing energy output with increasing ratio, and hence increasing temperature.

5.4 Discussion

The results of the simulation were compared to the results from a state of the art experimental setup. The results show the same general trends but consistently predict higher pulse energies, the discrepancy between the results was likely due to the highly divergent pump beam. Modeling the propagation of that beam was beyond the capability of the diffracting model.

Some of the assumptions that were made (and not made) about the seed and pump lasers created a significant difference between the predictions in Chapter 4 and the experimental system:

1. The simulation predicted small decreases in energy due to upconversion. However, energy transfer upconversion may play a bigger role due to the large population of the upper laser level. Most determinations of the effect of upconversion on end pumped Holmium lasers have been based

on experimental systems with different doping percentages and different lengths maintaining the crystal's absorption. The effects have been found to be small, however, most of these systems have been pumped on the 1940 nm absorption peak which may pump less population density into the upper laser level than pumping on the 1890 nm absorption peak, as described in Chapter 4. The PRF of the system was lower than other reported Ho:YLF amplifiers giving more time for the buildup of upper laser manifold population [53, 19].

2. The CW seed component and the small signal gain were not well characterised. The beam size of the CW component of the seed beam was not measured, and exact power during pulsed operation was unknown but probably less than the value when the seed laser is in hold off (pumped but not lasing).

3. While the wavelength of the pump beam was measured to the accuracy of the spectrometer, the resulting range, of approximately 2.5 nm, may have effected the results significantly, as was shown in the simulation results in Chapter 4, Figure 4.20.

4. Extrapolation of the temperature dependence of the cross sections and assumptions about the distribution of temperature in the gain medium have enabled the simulation to predicts how the high temperature operation would negatively effect performance. However, as the temperature of the experimental gain media were not known it was not possible to compared the effect of this parameter.

5. Losses due to reflection from optics in the setup were not considered.

6. The thermal lens(es) caused by the temperature distribution in the gain medium crystals were observed in the experimental system. The thermal lens was observed in the amplifier system on the π polarisation to the extent that the reduction in beam quality (due to the imperfect lens) rendered the angular separation difficult. While the thermal lens in YLF on the σ polarisation is typically much weaker than on the π polarisation due to the negative change in the refractive index with temperature mitigating the effect of lensing due to end face bulging, the thermal lensing in this amplifier was not measured and so can not easily be accounted for.

The large number of unknown parameters, the unaccounted for effects and perhaps most importantly the inability of the model to describe the large divergence of the pump beam made a quantitative comparison between the model and these experimental results unfeasible.

The experimental amplifier represents a state of the art MOPA system. To the authors knowledge this system generated the highest reported pulse energy from a MOPA system using end-pumped Ho:YLF or any end-pumped Holmium bulk laser.

Chapter 6

Energy scaling Ho:YLF Amplifiers

The model was used to study the energy scaling possibilities of Ho:YLF amplifiers beyond the energy levels obtained in the previous chapter. This chapter investigates the potential of energy scaling a one stage amplifier.

The procedure for scaling the energy output of the amplifier was to scale the area and the power of the pump beam in the gain medium. In this approach the intensity of the pump beams stayed the same, however, the intensity of the seed beam decreased.

6.1 Single Pass Amplifier

The possible combination of pump beams, seed beams and gain medium parameters were very large. The results from the previous Chapter were a reasonable starting point as a demonstrated state of the art seed beam. The beam had close to perfect beam quality and controlled narrow band wavelength.

Only single pass of the seed beam was considered as the combined peak intensity on the crystal surfaces was lower than in multiple pass setups. This approach was considered over double pass seeding due to the decreased risk of damage to optics caused by high peak powers.

There were also two different directions from which to pump the amplifier. The pump may be incident on the amplifier from the same side as the seed or from the other side. The first configuration was chosen as it is believed that it is experimentally easier to implement.

The Ho:YLF gain medium that was considered has the same properties as the two pass amplifier; 0.5 %

atomic doping percentage, variable length and pump beam sizes. The seed beam waist was set to the pump beam waist. Other properties are tabulated in Sub-section 4.2.2.

A seed beam pulsed at 50 Hz with 330 mJ per pulse and with 500 ns pulse length was considered. Good beam quality was assumed. The parameters are found in Table 6.1.

Simulation seed beam property	
Energy per pulse [mJ]	330
Beam quality [M^2]	1
Pulse length [ns]	500
PRF [Hz]	50
CW component [W]	0
Wavelength [nm]	2064
Polarisation	Sigma, (E‖a)

Table 6.1: Simulation parameters for the seed beam properties.

The design space was limited to CW pump beams with diffraction limited beam quality. Tm:Fiber oscillator amplifier systems that provide kilowatt's of power with good beam quality exist. For example commercial laser manufacturer IPG sells 400W Tm:Fiber lasers and kilowatt class Tm:Fiber lasers have been demonstrated [54]. The parameters are found in Table 6.2.

Simulation pump beam properties	Range
Power [W]	200-1000
Beam quality [M^2]	1
Wavelength [nm]	1890
PRF [Hz]	CW (0)

Table 6.2: Simulation parameters for the pump beam properties.

6.2 Area scaling results

Area scaling of amplifiers relies on the efficiency of the design that is scaled as well as the effect of any limiting factors. As the efficiency of this design was expected to be strongly influenced by the pump beam diameter as well as the length of the gain medium these parameters were not fixed. The proposed energy scaling procedure was to increase the power of the pump beam and then search for the optimum pump beam waist and gain medium length using the model.

In an ideal simplified case ASE , damage considerations, and diffraction were ignored. The pump and seed wavelengths were close together so the two beams diffract at a similar rate. While the optimum

ratio of pump diameter to seed ratio is not necessarily one, it remains a good assumption given that the diffraction and mode matching were neglected.

A direct search of the parameter space was used to approximate the maximum energy for the given pump power. The chosen search grid was coarse and was expected to show the general trends.

The results of the simulation are presented below. Figure 6.1 shows the results of a simulation were increasing pump powers lead to increased energy per pulse and the optical to optical efficiency.

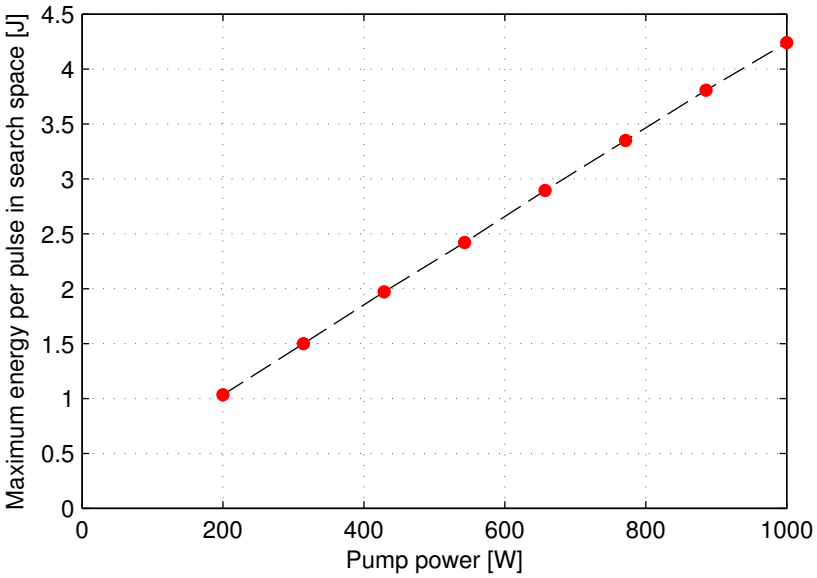

Figure 6.1: Maximum energy per pulse produced by the amplifier for increasing pump powers.

The results showed that the maximum energy per pulse increased linearly with the increased pump power, the slope was approximately 4 mJ/ W. The slope of the average power was 0.2 given the 50 Hz pulse repetition rate. The energy scaling procedure depended on optimizing the energy per pulse for different pump beam diameters and gain medium lengths. The changes in these parameters with increasing pump power are presented below in Figure 6.2.

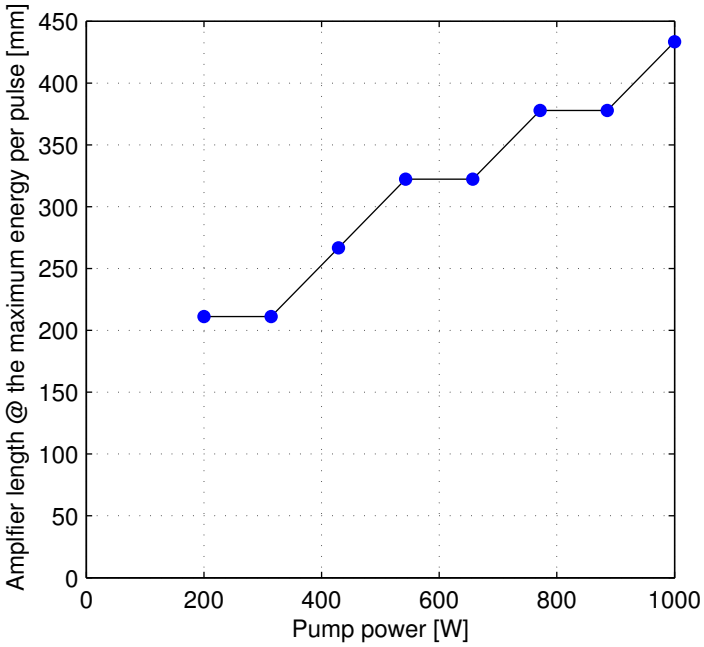

Figure 6.2: The length of the gain medium that produced the maximum energy per pulse.

The optimum pump beam diameter and gain medium length both increased with increasing pump power (the resolution of the direct search was not sufficient to produce smooth results).

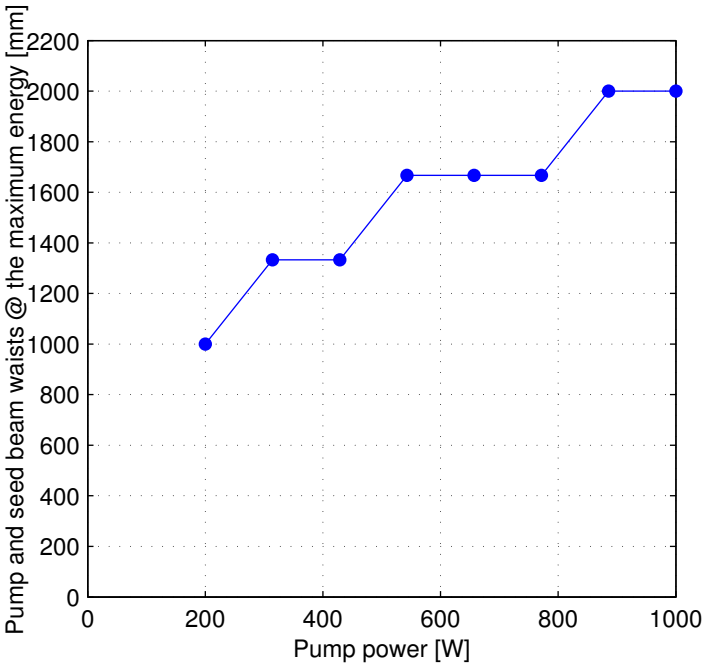

Figure 6.3: Beam waist of the pump and seed lasers that produced the maximum energy per pulse.

The beam area that corresponded to the optimum increased from 1 mm at 200 W of pump power

to 2 mm at 1 kW, shown in Figure 6.3. Given that the resultant energy extraction was linear, the constraints imposed on the pump beam by the need for increased pump intensity over longer amplifier lengths indicates that the optimum scaling method requires an increase in the pump brightness. In this case pumping a 450 mm long length of amplifier crystal with a 1 kW beam focused to a pump beam radius of 2 mm.

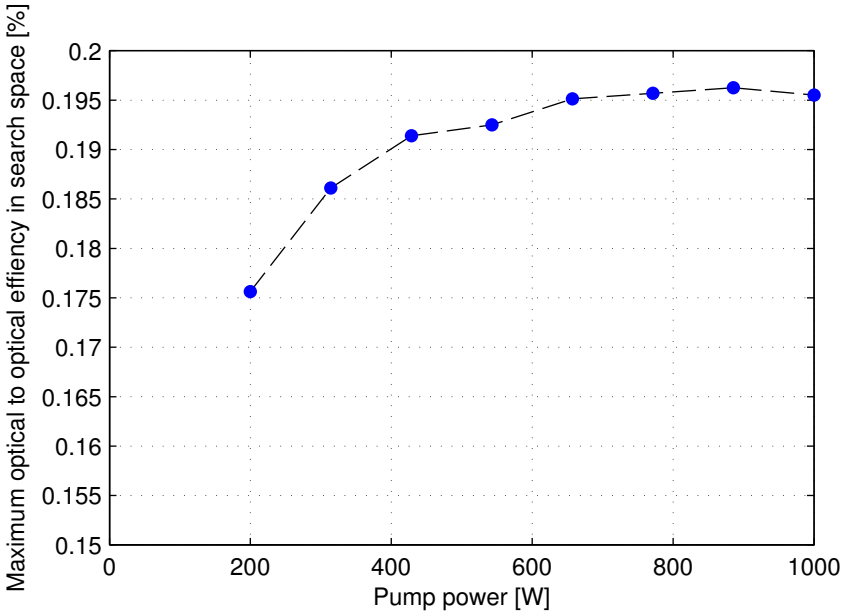

Figure 6.4: Efficiency of the energy scaling amplifier for increasing pump powers.

The optical to optical efficiency of the simulated system increased from 17.5 % at 200 W to 19.5 % at 885 W of pump power.

6.3 Discussion and conclusions

Optical to optical efficiencies of up to 19.5% were predicted for the single pass amplifier. There were a number of limits to this approach. There were limitations on: the possible size of a single crystals, the peak intensity of the amplified seed on the optics coatings before damage occurs, the minimum pump beam size and power incident on the crystal before thermal fracture, and on the amplifier size before ASE became problematic.

Chapter 7

Summary and Further Work

7.1 Summary of results

A numerical model has been developed using a rate equation formalism to simulate a Ho:YLF amplifier. The model was developed to account for the relevant processes in quasi-three level gain media, they included: spontaneous emission, stimulated emission, absorption and energy transfer upconversion.

The model spatially and temporally resolved these processes using a finite difference approach in the temporal domain while a number of different approaches were used to approximate the spatial propagation of the pump and seed beams.

The convergence characteristics of the model show that the model finds stable solutions and also provides an estimate of the numerical error introduced by the numerical approximations made in the model.

The model was used to optimise the design of a two pass amplifier. Model parameters have been changed to show the general trends in performance. Optimization of the following parameters predicted pulse energies above 480 mJ when seeded by a 55 mJ pulse at repetition rates of 50 Hz at the following values: pump wavelength of 1892 nm, crystal length of 100 mm of 0.5 % (atm.) doped Ho:YLF, and effective beam sizes of 1 mm and 0.95 mm for the pump and seed beams respectively

The results of the simulation are compared to the results from a state of the art experimental setup. The results show the same general trends but consistently predict higher pulse energies. These discrepancies between the results were shown to be due partly to description of the highly divergent pump beam.

Extrapolation of the temperature dependence of the cross sections and assumptions about the distribution of temperature in the gain medium have enabled the simulation to predict how the high temperature operation would negatively effect performance. Similarly, parametrization of the unknown upconversion coefficient leads to prediction of decrease in performance due to energy transfer upconversion.

Simulation results of a high energy single pass amplifier predict that energy scaling in Ho:YLF follows linearly with respect to pump power and that in an ideal case multi-Joule operation is possible at 50 Hz with optical to optical efficiencies of 19.5 %.

7.2 Future work

- Modelling the divergent pump beam in a consistent manner.
- Measurement of the cross sections and other material properties above room temperature.
- Incorporation of a model for temperature distribution in the crystal. There are a number of possibilities such as Finite Element Methods (FEM).

Publications

Journal Publications

- H. J. Strauss, W. Koen, C. Bollig, M. J. D. Esser, C. Jacobs, **O. J. P. Collett**, and D. R. Preussler, "Ho:YLF & Ho:LuLF slab amplifier system delivering 200 mJ, 2 µm single-frequency pulses," Optics Express 19 (15), 13974-13979 (2011).

Journal Publications in preparation

- M. J. D. Esser, H. J. Strauss, W. Koen, **O. J. P. Collett** and C. Bollig "Ho:YLF & Ho:LuLF Slab Laser End-pumped by a Tm:YLF laser," to be submitted to Applied Physics B: Lasers & Optics.

Invited International Conference Papers

- M. J. D. Esser, C. Jacobs, W. Koen, H. Strauss, D. Preussler, L. R. Botha, O. J. P. Collett and C. Bollig "High-Energy 2 µm Solid-State Laser Development" Fourteenth Annual Directed Energy Symposium, Directed Energy Professional Society, 14-18 November 2011, La Jolla, California (invited) (2011).
- C. Jacobs, M. J. D. Esser, H. Strauss, W. Koen, D. Preussler, L. R. Botha, O. J. P. Collett and C. Bollig "High-Energy Laser Research for Infrared Countermeasures" Paper 8543-10, SPIE Security & Defence, 24-27 September 2012, Edinburgh, United Kingdom (invited) (2012).
- C. Bollig, H.J. Strauss, W. Koen, M.J.D. Esser, C. Jacobs, **O.J.P. Collett**, D.R. Preussler and L.R. Botha, "High-Energy Narrow-Band Mid-Infrared Laser Systems", 20th International Laser Physics Workshop (LPHYS '11) Sarajevo, July 11-15, 2011, Talk #4.5.2. (invited) (2011).

International Conference Papers

- **O. Collett**, C. Bollig, and M. J. D. Esser, "Numerical Optimization of a high-energy end-pumped Ho:YLF Slab Amplifier," in CLEO/Europe and EQEC 2011 Conference Digest, OSA Technical Digest (CD) (Optical Society of America, 2011), paper CA_P24 (2011).
- H.J. Strauss, D. Preussler, **O.J.P. Collett**, M.J.D. Esser, C. Jacobs, C. Bollig, W. Koen and K. Nyangaza, "330 mJ, 2 μm, Single Frequency, Ho:YLF Slab Amplifier," Advanced Solid-State Photonics, Istanbul, Turkey, 13-16 February 2011, ATuA4 (2011).
- W. Koen, H.J. Strauss, C. Bollig, M.J.D. Esser, C. Jacobs, **O.J.P. Collett**, K. Nyangaza and D. Preussler "200 mJ Single Frequency Ho:YLF & Ho:LuLF Slab Amplifier System at 2064 nm," in 4th EPS-QEOD Europhoton Conference, Hamburg, Germany, WeC4, Europhysics Conference Abstract Volume 34C, ISBN 2-914771-64-9, (2010).
- M.J.D. Esser, H.J. Strauss, W. Koen, **O.J.P. Collett** and C. Bollig, "End-pumped Ho:YLF & Ho:LuLF Slab Laser," in 4th EPS-QEOD Europhoton Conference, Hamburg, Germany, WeP29, Europhysics Conference Abstract Volume 34C, ISBN 2-914771-64-9, (2010).

National Conference Papers

- O. J. P. Collett and M. J. D. Esser "Computation of Amplified Spontaneous Emission in multi-element laser models" in South African Institute of Physics 57th annual conference, hosted by University of Pretoria, July 2011, paper 416, (2012).
- C. JACOBS and O. J. P. Collett "Challenges in developing a Holmium slab laser to pump a rod OPO" in South African Institute of Physics 57th annual conference, hosted by University of Pretoria, July 2012, paper 428, (2012).
- **O.J.P. Collett**, M. J. D. Esser and C. Bollig "Pulse Repetition Frequency locking by pump modulation in numerical simulations of a diode end pumped passively Q-switched Nd:YAG laser with a Cr4+:YAG saturable absorber," in South African Institute of Physics 56th annual conference, hosted by UNISA, July 2011, paper 322, (2011).
- H. J. Strauss, W. Koen, C. Bollig, M. J. D. Esser, C. Jacobs, **O. J. P. Collett** and D. R. Preussler "2 μm Ho doped amplifiers" in South African Institute of Physics 56th annual conference, hosted by UNISA, July 2011, paper 150, (2011).

- Cobus Jacobs, Hencharl Strauss, Christoph Bollig, Daniel Esser, Wayne Koen, **Oliver Collett**, Kwanele Nyangaza and Dieter Preussler, "Single Frequency 2µm MOPA delivering 200mJ at 50Hz," in South African Institute of Physics 55th annual conference, CSIR, Pretoria, September 2010, paper 280, ISBN 978-0-620-46211-2 (2010).

- M. J. D Daniel Esser, **Oliver Collett** and Christoph Bollig, "Demonstration of a Hybrid Ho:YLF Ho:LuLF Slab Laser," in South African Institute of Physics 55th annual conference, CSIR, Pretoria, September 2010, paper 304, ISBN 978-0-620-46211-2 (2010).

- Hencharl Johan Strauss, Shaun Burd, Wayne Koen, Daniel Esser, Cobus Jacobs, **Oliver Collett**, Kwanele Nyangaza, Dieter Preussler and Christoph Bollig, "Multi pass 1.9 µm Tm:YLF slab laser pump source," in South African Institute of Physics 55th annual conference, CSIR, Pretoria, September 2010, paper 247, ISBN 978-0-620-46211-2 (2010).

- M. J. D. Esser, C. Jacobs, W. Koen, H. Strauss, D. Preussler, L.R. Botha, **O. J. P. Collett** and C. Bollig, "Development of High-Energy 2 µm Solid-State Lasers," CSIR conference "Science: real and relevant," August 2010.

Bibliography

[1] B. M. Walsh G. W. Grew N. P. Barnes. Energy levels and intensity parameters of Ho^3+ ions in $GdLiF_4$, $YLiF_4$ and $LuLiF_4$. *JOURNAL OF PHYSICS CONDENSED MATTER*, 17:7643–7665, 2005.

[2] University of Hamburg. Ho YLF spectra, 2010.

[3] H.J. Strauss D. Preussler O.J.P. Collett M.J.D. Esser C. Jacobs C. Bollig W. Koen K. Nyangaza. 330 mJ, 2 μm, Single Frequency, Ho:YLF Slab Amplifier. In *Advanced Solid-State Photonics*, 2011.

[4] I. T. Sorokina K. L. Vodopyanov, editor. *Solid-State Mid-Intrared Laser Sources*. Springer, 2003.

[5] A. Dergachev D. Armstrong A. Smith M. Dubois. High-power, high-energy ZGP OPA Pumped by a 2.05 μm Ho:YLF MOPA System. In *SPIE - The International Society for Optical Engineering, Vol.6875*, 2008.

[6] T. Y. Fan R. L. Byer. Modeling and CW Operation of a Quasi-Three-Level 946nm Nd:YAG laser. *IEEE JOURNAL OF QUATUM ELECTRONICS*, QE-23:605–612, 1987.

[7] W. P. Risk. Modeling of longitudinally pumped solid-state lasers exibiting reabsorbtion losses . *Journal Optical Society of America B*, 5:1412–1423, 1988.

[8] W. F. Krupke L. L. Chase. Ground-state depleted solid-state lasers: principles, characteristics and scaling. *Optical and Quantum Electronics*, 22:S1–S22, 1990.

[9] S. A. Payne L. L. Chase L. K. Smith W. L. Kway W. F. Krupke. Infrared Cross-Section Measurement for Crystals Doped with Er,Tm, and Ho. *IEEE JOURNAL OF QUANTUM ELECTRONICS*, 28(11):2619–2630, 1992.

[10] N. P. Barnes M. Petros J. Yu U. N. Singh B. M. Walsh. Spectroscopy and modeling of solid state lanthanide lasers: Application to trivalent Tm^{3+} and Ho^{3+} in $YLiF_4$ and $LuLiF_4$. *JOURNAL OF APPLIED PHYSICS*, 95:3255–3271, 2004.

[11] N. P. Barnes B. M. Walsh E. D. Filer. Ho:Ho upconversion: applications to Ho lasers. *J. Opt. Soc. Am. B*, 20:1212, 2003.

[12] N. P. Barnes W. J. Rodriguez B. M. Walsh. Ho:Tm:YLF laser amplifiers. *Journal of the Optical Society of America B*, 13:2872–2882, 1996.

[13] B. D. Bartolo N. P. Barnes B. M. Walsh. Branching ratios, cross sections, and radiative lifetimes of rare earth ions in solids: Application to Tm^{3+} and Ho^{3+} ions in LiYF. *JOURNAL OF APPLIED PHYSICS*, 83(5):2772 – 2788, 1998.

[14] Brain M Walsh. *Spectroscopy and Excitation Dynamics of trivalent lanthanides Tm^{3+} and Ho^{3+} in $LiYF_4$*. PhD thesis, Boston College, 1995.

[15] Mulugeta Petros N. P. Barnes U. N. Singh, Jirong Yu. Injection-seeded, room temperature diode-pumped Ho:Tm:YLF laser with output energy of 600 mJ at 10 Hz. In *OSA TOPS*, pages 194–196, 1998.

[16] P. Budni C. Ibach S. Setzler E. Gustafson R. Castro E. Chicklis. 50-mJ, Q-switched, 2.09-μm holmium laser resonantly pumped by a diode-pumped 1.9-μm thulium laser. *Optics Letters*, 28:1016–1018, 2003.

[17] M. Schellhorn A. Hirth. Modeling of Intracavity-Pumped Quasi-Three-Level Lasers. *IEEE JOURNAL OF QUANTUM ELECTRONICS*, 38,11:1455–1464, 2002.

[18] Sik So. *Power Scaling of Tm:YLF-pumped Ho:YAG Lasers*. PhD thesis, UNIVERSITY OF SOUTHAMPTON, 2007.

[19] M. Eichhorn M. Schellhorn. High-energy ho:llf mopa laser system using a top-hat pump profile for the amplifier stage. *Applied Physics B*, 109:351–357, 2012.

[20] K. Altman C. Pflaum S. Seider. Three-dimensional finite element computation of laser cavity eigenmodes. *APPLIED OPTICS*, 43:1892–1901, 2004.

[21] H. Shu. *Analytic and numerical modeling of diode pumped Yb:YAG laser oscilators and amplifiers.* PhD thesis, University of Central Florida, 2003.

[22] M. D. Feit J. R. Morris J. A. Fleck. Time-Dependant Propagation of High Energy Laser Beams through the Atmosphere. *Applied Physics*, 10:129–160, 1976.

[23] Anothony E. Siegman. *Lasers.* Universty Science Books, 1986.

[24] F. Shen A. Wang. Fast-Fourier-transform based numerical integration method for the Rayliegh-Sommerfeld diffraction formula. *Applied optics*, 45:1102–1110, 2006.

[25] M. Wohlmuth C. Pflaum K. Altman M. Paster C. Hahn. Dynamic multimode analysis of Q-switched solid state laser cavities. *OPTICS EXPRESS*, 17:17303–17316, 2009.

[26] Z. Xiang J. Chen C. Liu J. Ge T. Li Z. Zhao Y. Dong S. Pan D. Wang. Beam quality improvement by gain guiding effect in end-pumped Nd:YVO4 laser amplifiers. *OPTICS EXPRESS*, 19 (21):21060–21073, 2011.

[27] C. Pare. Optimum laser beam profile for maximum energy extraction from a saturable amplifier. *Optics Communications*, 123:762–776, 1996.

[28] T. Y. Fan. Optimizing the Efficiency and Stored Energy in Quasi-Three-Level Lasers. *IEEE JOURNAL OF QUATUM ELECTRONICS*, 28:2692–2697, 1992.

[29] Orazio Svelto. *Principles of Lasers, FOURTH EDITION.* Springer, 1998.

[30] M. Eichhorn. Quasi-three-level solid-state lasers in the near and mid infrared based on trivalent rare earth ions. *APPLIED PHYSICS B*, 93:269–316, 2008.

[31] F. Cornacchia A. Toncelli M. Tonelli. Review- $2\mu m$ lasers with fluoride crystals : Research and development. *Progress in QuantumElectronics*, 33:61–109, 2009.

[32] D. E. McCumber. Einstein Relations Connecting Broadband Emission and Absorption Spectra. *Physical Review*, 136:954–957, 1964.

[33] G. Rustad K. Stenersen. Modeling of Laser-Pumped Tm and Ho Lasers Accounting for Up-conversion and Ground-State Depletion. *IEEE JOURNAL OF QUANTUM ELECTRONICS*, 32:1645–1656, 1996.

[34] N. P. Barnes E. D. Filer C. A. Morrison C. J. Lee. Ho:Tm Lasers I: Theoretical. *LEEE JOURNAL OF QUANTUM ELECTRONICS*, 32:92–103, 1996.

[35] L. B. Shaw R. S. F. Chang N. Djeu. Measurement of up-conversion energy-transfer probilities in $Ho : Y_3Al_5O_{12}$ and $Tm : Y_3Al_5O_{12}$. *Physical Review B*, 50 (10):6609–6619, 1994.

[36] J. E. Harvey. Fourier treatment of near -field diffraction theory. *American Journal of Physics*, 47(11):974–980, 1979.

[37] Goodman. *Introduction to Foureir Optics*. McGRAW-HILL, 1996.

[38] H. J. Strauss W. Koen C. Bollig M. J. D. Esser C. Jacobs O. J. P. Collett D. R. Preussler. Ho:YLF & Ho:LuLF slab amplifier system delivering 200 mJ, 2 μm single-frequency pulses. *Optics Express*, 19 (15):13974–13979, 2011.

[39] W. E. Schiesser G. W. Griffiths. *A COMPENDIUM OF PARTIAL DIFFERENTIAL EQUATION MODELS, Method of Lines Analysis with MATLAB New York*, volume Volume 18. CAMBRIDGE UNIVERSITY PRESS, 2009.

[40] M. Newstein P. Rabinowitz B. N. Perry. Wave propagation in media with focused gain. *PHYSICAL REVIEW A VOLUME 27, NUMBER 4 APRIL 1983*, 27:1989–2002, 1983.

[41] Jason D. Schmidt. *Numerical Simulation of Optical Wave Propagation*. SPIE PRESS, 2010.

[42] O. Svelto S. Taccheo C. Svelto. Analysis of amplified spontaneous emission: some corrections to the Linford formula. *Optics Communications*, 149:277–282, 1998.

[43] T. Kozacki. Numerical Errors of diffraction computing using plane wave spectrum decomposition. *Optics Comunications*, 281:4219–4223, 2008.

[44] Ronald N. Bracewell. *The Fourier Transform and Its Applications*. McGraw-Hill Higher Education, 2000.

[45] K. Matsushima T. Shimobaba. Band-Limited Angular Spectrum Method for Numerical Simulation of Free-spece Propagation in Far and Near Fields. *Optics Express*, 17:19662–19673, 2009.

[46] A. Brant J. Dym. Fast Calculation of Multiple Line Integrals. *Journal of Scientific Computing*, 20:1417–1429, 1999.

[47] G. Beylkin. Discrete Radon Transforms. *IEEE TRANSACTIONS ON ACOUSTICS, SPEECH, AND SIGNAL PROCESSING*, 35:162–172, 1987.

[48] *The Mathworks, MATLAB R2009b.*

[49] M. Schellhorn S. Ngcobo C. Bollig. High-power diode-pumped Tm:YLF slab laser. *Applied Physics B: Lasers and Optics*, 94:195–198, 2009.

[50] M. Esser C. Jacobs W. Koen D. Preussler K. Nyangaza M. Schellhorn C. Bollig. 70 mJ Single-Frequency Q-Switched Ho:YLF Ring Laser-Amplifier System Pumped by a Single 82 W Tm Fibre Laser. In *Middle-Infrared Coherent Sources, Trouville, France*, 2009.

[51] R. L. Byer J. M. Eggleston T. J. Kane. The slab geometry laser - part II: thermal effects in a finite slab. *IEEE J. Quantum Electronics*, 21:1195–1210, 1985.

[52] R. Poprawe H. D. Hoffmann J. Weitenberg T. Mans P. Russbueldt. Compact diode-pumped 1.1 kw yb:yag innoslab femtosecond amplifier. *Opt. Lett.*, 32:4169–4171, 2010.

[53] M. J. D. Esser C. Jacobs M. Schellhorn H. Strauss C. Bollig W. Koen. Compact fibre-laser-pumped Ho:YLF oscillator-amplifier system. *Applied Physics B*, 99:101–106, 2010.

[54] Joshua E. Rothenberg Lewis D. Book Gregory D. Goodno. 600-W, Single-Mode, Single-Frequency Thulium Fiber Laser Amplifier. In *SPIE: Fiber Lasers V*, 2009.